

# A new avalanche photodiode readout for the Crystal Barrel experiment

Friedemann Zenke

Diplomarbeit in Physik

angefertigt im  
Helmholtz-Institut für Strahlen- und Kernphysik

vorgelegt der  
Mathematisch-Naturwissenschaftlichen Fakultät der Universität Bonn

März 2009



# Acknowledgments

I would like to express my gratitude to the various people who kindly provided me with their helpful assistance during all endeavors to finish this thesis. At first I would like to thank Reinhard and Ulrike for giving me the opportunity to work at the Crystal Barrel experiment. I owe thanks to Klaus Desch who is the second referee of this thesis. I big thanks goes to Michael Steinacher for his sheer unlimited supply of good advice regarding electronics and for fruitful instructive discussions. I always learned something new. A thanks also goes to Groningen, namely to Herbert Löhner and Myroslav Kavatsyuk for supplying the Gerber files of their PWO shaper prototype. Many thanks to Igor Konorov for the VHDL sources for his SADC.

Furthermore I would like to thank Alexander for his unfailing support and encouragement. This thesis could not exist without the continued generous support of Annika, Christoph, Christian and Philipp. The people from room 102 showed ultimate patience in answering questions and providing reassurance. My full appreciation also belongs to all the people who actively contributed in making the Studentenexperiment a success. I would like to further thank the people who accompanied me through various revisions during the writing phase and in times of infinite grumpiness. I owe special thanks to Hannah for proofreading my occa and for her help in converting it into scientific writing.

Finally my thoughts wander to those people who were both omnipresent and indispensable throughout my studies. Thank you Mario and Johanna for physical and profane discussions. A thanks goes to Karim for unforgettable reflections over coffee. Another goes to Felix for sharing all the good memories on wave mechanics. I would like to give a special thanks to Martin and Hiltrud for their constant support without compromise.



# Contents

<b>1</b>	<b>Introduction</b>	<b>9</b>
1.1	Hadron physics . . . . .	9
1.1.1	Baryon states . . . . .	9
1.1.2	Missing resonance problem . . . . .	10
1.2	Crystal Barrel experiment . . . . .	12
1.2.1	Charged particle tracking extension . . . . .	12
1.2.2	A new readout for the main calorimeter . . . . .	13
1.3	Purpose of this thesis . . . . .	13
<b>2</b>	<b>The Crystal Barrel experiment</b>	<b>15</b>
2.1	Polarized photon beam . . . . .	16
2.1.1	Electron accelerator . . . . .	16
2.1.2	Modes of operation . . . . .	18
2.1.3	Tagging system . . . . .	19
2.2	Polarized target . . . . .	20
2.2.1	Additional targets . . . . .	21
2.3	Subdetectors . . . . .	21
2.3.1	Inner detector . . . . .	21
2.3.2	Main calorimeter . . . . .	22
2.3.3	Forward Plug . . . . .	22
2.3.4	Čerenkov detector . . . . .	22
2.3.5	MiniTAPS . . . . .	24
2.3.6	Flux monitoring . . . . .	24
2.4	Trigger and data acquisition . . . . .	24
2.4.1	A new readout . . . . .	27
2.5	The Studentenexperiment . . . . .	28
<b>3</b>	<b>The crystal light readout</b>	<b>31</b>
3.1	Scintillation detectors . . . . .	31
3.1.1	Inorganic scintillators . . . . .	31
3.1.2	Crystal Barrel crystals . . . . .	32
3.2	Photo detectors . . . . .	32
3.2.1	Current photodiode readout . . . . .	34
<b>4</b>	<b>Initial situation and equipment</b>	<b>35</b>
4.1	Hamamatsu S8664-1010 Si APD . . . . .	35
4.2	Prototype crystal end-cap . . . . .	35

## Contents

4.3	LNP preamplifier . . . . .	35
4.4	$3 \times 3$ crystal matrix . . . . .	38
4.5	High voltage power supply . . . . .	38
4.6	i-trOnics SADC . . . . .	40
4.6.1	Zero Chip firmware . . . . .	41
<b>5</b>	<b>The trigger branch</b>	<b>43</b>
5.1	Goals and challenges . . . . .	43
5.2	The preamplifier signal . . . . .	44
5.3	Background theory on pulse shaping . . . . .	44
5.4	Timing filter developments . . . . .	47
5.4.1	Experimental method . . . . .	48
5.4.2	Time-walk correction . . . . .	48
5.4.3	Ortec 474 Timing Amplifier . . . . .	49
5.4.4	Integrated timing filters . . . . .	51
5.5	Timing filter tests with cosmic muons . . . . .	54
5.6	Timing filter tests with the tagged photon beam . . . . .	55
5.6.1	Experimental method . . . . .	57
5.6.2	Results and discussion . . . . .	58
5.7	Timing filter tests with an LED pulser . . . . .	63
5.7.1	Experimental method . . . . .	63
5.7.2	Results and discussion . . . . .	64
5.8	Summary and conclusion . . . . .	65
<b>6</b>	<b>The energy branch</b>	<b>67</b>
6.1	Energy readout . . . . .	68
6.1.1	Introduction and background theory . . . . .	68
6.1.2	Experimental method . . . . .	68
6.1.3	Results and discussion . . . . .	75
6.1.4	Future improvements . . . . .	77
6.2	Time readout . . . . .	77
6.2.1	Introduction and background theory . . . . .	78
6.2.2	Simulations . . . . .	78
6.2.3	Linear fit time extraction . . . . .	81
6.2.4	Experimental method . . . . .	82
6.2.5	Results and discussion . . . . .	84
6.3	Summary and conclusion . . . . .	85
6.4	Outlook . . . . .	88
<b>7</b>	<b>Summary and conclusion</b>	<b>89</b>
<b>A</b>	<b>Operation preliminaries for the LNP preamplifier</b>	<b>93</b>
A.1	Reversing the polarity of the output . . . . .	93
A.2	Modifications towards noise reduction . . . . .	93

<b>B Quantization errors in <math>t_0</math> extraction</b>	<b>95</b>
<b>C Circuit layout diagrams</b>	<b>99</b>

*Contents*

# 1 Introduction

## 1.1 Hadron physics

Nature's most powerful interaction – the strong force – has been puzzling scientists for decades. It is not only the reason for the nucleon-nucleon interaction, but also the force responsible for confining quarks into hadrons. Although it is generally accepted that the equations profoundly describing the strong force are found and formulated in quantum chromodynamics (QCD), the equations cannot be solved analytically for all energy scales. This is because the coupling constant of the interaction  $\alpha_s$  is strongly dependent on the momentum transfer  $Q$  of the participating particles. While for high momentum transfers ( $Q \gtrsim 100 \text{ GeV}$ ) the perturbative calculation of QCD is feasible ( $\alpha_s \lesssim 0.1$ ), this is not the case for low values of  $Q$  of less than a few GeV. In the low energy range  $\alpha_s$  is in the order of one, which makes the perturbative calculation of the the exact theory very difficult or even impossible [5].

The two main advances in trying to understand the strong interaction are scattering experiments and spectroscopy experiments. It was these types of experiments that guided scientists like Bohr or Rutherford to formulate their atomic models and that ultimately led to a thorough understanding of the electromagnetic interaction. In hadron physics the bound objects of study are hadrons and the underlying force is the strong force.

### 1.1.1 Baryon states

Just like in atomic physics one approach to understanding the strong force is studying the excitation spectrum of hadronic systems. The main difference is the different energy scale. The energies involved in hadronic reactions are typically in the same order of magnitude as the mass of the systems themselves. That results in some peculiarities that are unique to hadron physics. In hadron physics an excited state is usually considered as a different particle, due to its higher mass. However, these particles are usually very unstable and decay very rapidly – typically in the order of  $\approx 10^{-24} \text{ s}$ . As a direct consequence such states cannot be observed directly. Their existence can only be reconstructed from their primary and secondary decay products. The decay usually proceeds via emitting charged- and uncharged mesons that on their part consecutively decay to photons and leptons. By characterizing the angular distribution and energies of the decay products it is possible to extract the corresponding quantum numbers of the responsible state. The arising field dedicated to the excitation and detection of

## 1 Introduction

such states is called *hadron spectroscopy*.

A direct consequence of the high energy scale is that excitation levels are not sharp spectral lines of well defined energy, like in the atomic case. The energy uncertainty given by the Heisenberg uncertainty principle is large enough to allow for significant overlap between neighboring states. Therefore several states can coincide at one certain energy and all contribute to the same reaction. Moreover the different contributions have to be understood quantum mechanically as the superposition of different probability amplitudes. Being the square of the sum of all amplitudes, the resulting differential cross section is subject to interference. This makes it hard to disentangle the involved states. One underlying method of disentanglement is called partial wave analysis (PWA). Since the contributing amplitudes cannot be measured directly, trying to find a set of amplitudes that reproduces a given cross section, inherently leads into ambiguities.

This problem can be alleviated to a certain extent by performing polarization experiments<sup>1</sup>. This allows to measure additional observables which further constrain the possibilities of interfering partial waves. In this context the parameters are called polarization observables. The ultimate aim of such experiments, like the Crystal Barrel experiment, is to provide complete experimental data for the PWA. For pseudoscalar single meson photoproduction it is believed that the full knowledge of eight carefully chosen single- and double polarization observables will lead to an unambiguous description of the underlying reactions. This fact is commonly expressed as performing a *complete experiment* [8]. Such a complete experiment will ultimately lead to a better understanding of the excitation spectrum of the nucleon.

### 1.1.2 The missing resonance problem

Because the computation of QCD is technically not feasible in the energy range of hadronic bound states, various phenomenological models have been developed to describe the data. The  $N^*$  excitation spectrum of one such constituent quark model, is shown in Figure 1.1. In an approach like that, the model is usually chosen to resemble several states, which are already known. The scale is then generally fixed at the ground state – the proton in the present case. One can observe that in some ranges the resulting model predictions are well met by the experimental results. However, in other regimes the model predictions do not have an experimental counterpart. The key question now is: Do these states exist or not? There are several approaches to this so called *missing resonance problem*. First it could be argued that the states do not exist and the models do not take into account certain aspects of the system. A higher degree of organization within the hadronic bound state could for instance explain a freeze-out of certain degrees of freedom, thus leading to less states. A possible example of an approach

---

<sup>1</sup>Depending on the number of particles that are polarized in the initial state and whether or not the polarization can be measured for the final state one talks about single, double and triple polarization observables.

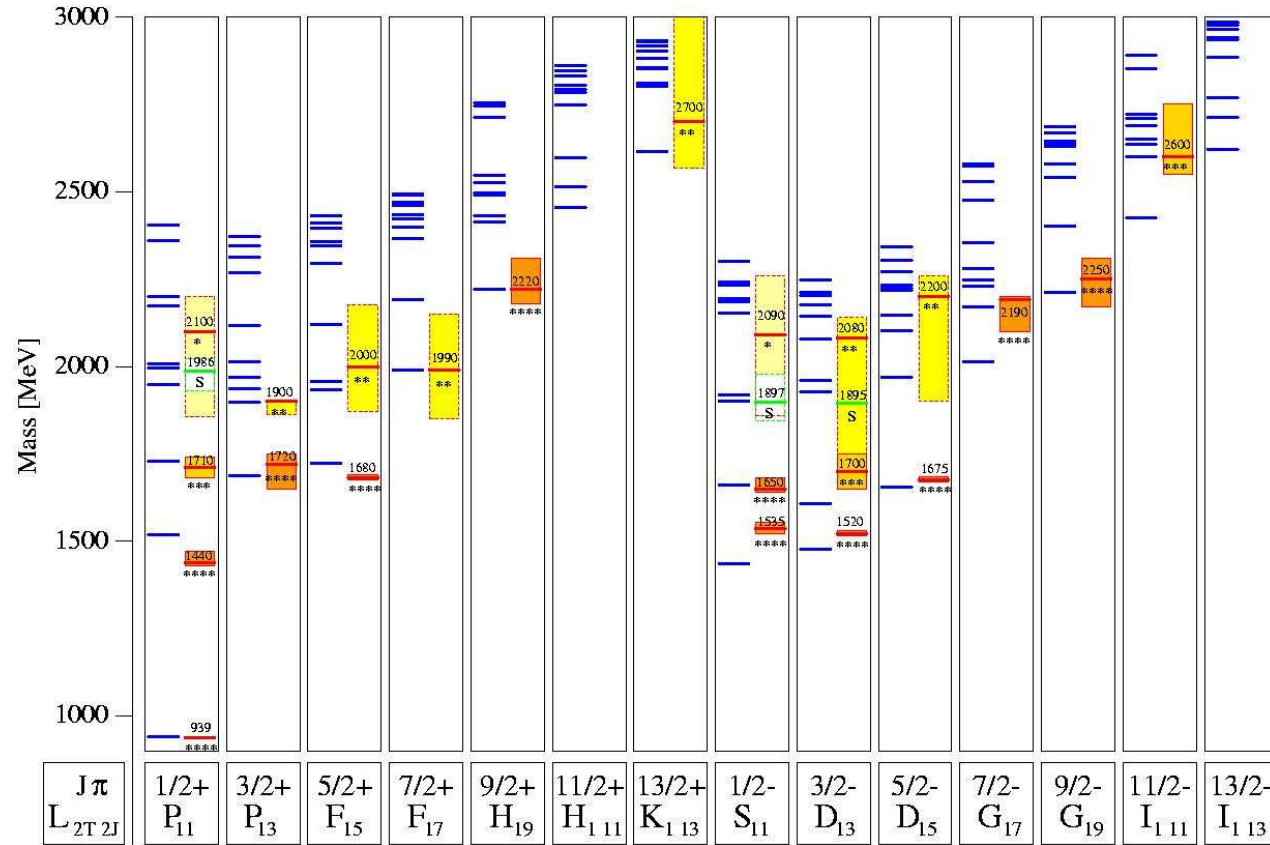


Figure 1.1:  $N^*$  resonances predicted by the Bonn model. Some theoretical predictions on the left hand side of each column are confirmed by measurement (right hand side, where the bars represent experimental uncertainties). However, especially at higher energies many states are predicted that were not yet observed experimentally [31].

## 1 Introduction

that takes into account a reduced number of degrees of freedom, is a relativistic quark-diquark model [30]. Second one might argue that the experimentalists have not seen the states in question yet. They might be hidden under other stronger and predominant resonances. The fact how most of the data of the  $N^*$  and the  $\Delta$  resonance spectrum have been measured could also give an explanation why these states are missing. Most experimental data shown in Figure 1.1 was measured with the help of pion scattering. It is very much possible that pion scattering favors the formation of certain hadronic states over others. In any case more experimental data on the states in question are needed. Finally a different excitation mechanism could shed some light. At this point photoproduction<sup>2</sup> experiments – in contrast to pion scattering – offer a new perception of the problem. In addition double polarization experiments could furthermore help to disentangle the interfering partial waves that contribute to one channel. Finally new high precision measurements might lead to a strong foundation upon which to build, check and validate models.

## 1.2 The Crystal Barrel experiment

The Crystal Barrel experiment at the Electron Stretcher Accelerator (ELSA) in Bonn is a photoproduction experiment that focuses on the detection of multi-photon final states from the decay of baryon states. The multiple photons are detected and characterized in multiple electromagnetic calorimeters of the experiment. One of the most outstanding properties of the experiment is its capability to perform single- and double polarization measurements. In these experiments either the beam or the target – or both are polarized.

There are two major upgrade plans for the Crystal Barrel experiment. The upgrades are aiming at making the experiment both more versatile (to gain insight into new reaction channels that are currently not accessible) and more efficient (to gain higher statistical significance). One of the upgrades aims at extending the experiment's capabilities of particle detection from neutral final states to charged final states with all its benefits. The second upgrade will make the trigger of the experiment more efficient.

### 1.2.1 The charged particle tracking extension

Due to the different energy loss mechanism of protons and charged mesons in matter, they generally escape the electromagnetic calorimeters. Therefore their energy cannot be measured very well. However, track detection and reconstruction within a magnetic field offers a way of measuring the transverse momentum  $p_t$  instead. In addition to that the method allows to extract the sign of the charge and to distinguish photons from electrons and charged mesons. Therefore the

---

<sup>2</sup>In the case of *photoproduction*, a real photon of known energy is used to excite the nucleon.

upgrade will include the integration of a time projection chamber into the main calorimeter and the addition of a solenoid magnet.

The benefits of this upgrade are many-fold and will extend the experiment's capabilities far beyond what is possible now. While the detection capabilities for multi-photon final states will not suffer from the upgrade, a lot of new charged channels will become accessible. The vertex reconstruction capabilities of the time projection chamber will furthermore allow to specifically aim at the detection of reactions involving strange particles like the  $\Sigma^0$  or the  $\Lambda$ . The signature of these particles is a secondary decay vertex outside of the target. Due to the self analyzing power of such strange decays, recoil polarization will become accessible for the experiment [4].

#### 1.2.2 A new readout for the main calorimeter

The second upgrade is aiming at refining the readout of the main calorimeter. This will allow to also include the main calorimeter in the first level trigger. Currently the detector can only actively contribute to the second level trigger. The trigger scheme will be explained in detail in Section 2.4. The upgrade furthermore includes the transition to new readout electronics such as Flash-ADCs (FADCs) and will add the capability of time extraction to the main calorimeter. These changes go hand in hand with a complete refurbishment or replacement of the current crystal readout. The core problem of the current readout is, that it is too slow to contribute a first level trigger signal. Several possibilities to make it faster are currently evaluated. Since the possibility of a photomultiplier readout is ruled out, as the whole setup is meant to be kept operational inside a magnetic field, one way of doing so would be to add a silicon photomultiplier to the existing readout of the crystals. This addition would yield a signal that rises fast enough that it could be used for trigger generation and time extraction. The studies on this topic are nearly at their end. The details are described in two different works by Manuela Gottschall and Marco Wehrfritz [15, 51]. Another possibility would be to replace the current photodiode readout by a new readout based on avalanche photodiodes which is the topic of this thesis.

### 1.3 The purpose of this thesis

This thesis studies the option of a new avalanche photodiode readout for the Crystal Barrel detector. Furthermore this work will be looking more closely at the possibilities and advantages of a FADC based readout for the main calorimeter. The Chapters 2 and 3 will introduce the current experiment, while Chapter 4 will describe the initial situation during the first period of this work. I will cover trigger related questions in Chapter 5 and then face the necessities of a high resolution energy readout with FADCs in Chapter 6. Details on a fully digital time extraction will also be given in this chapter.

## *1 Introduction*

In this work several tests are devised, carried out and analyzed. A possible solution for a readout scheme for the main calorimeter is found. The ideas described in this work justify and show the functional efficiency by test results. The final conclusion will be, that an avalanche photodiode based readout for the Crystal Barrel calorimeter is feasible and able of providing first level trigger capability within the required working parameters. I will further conclude that digital feature extraction with the help of programmable FADCs will not only yield energy information but furthermore offers the extraction of time information by means of digital filtering.

## 2 The Crystal Barrel experiment

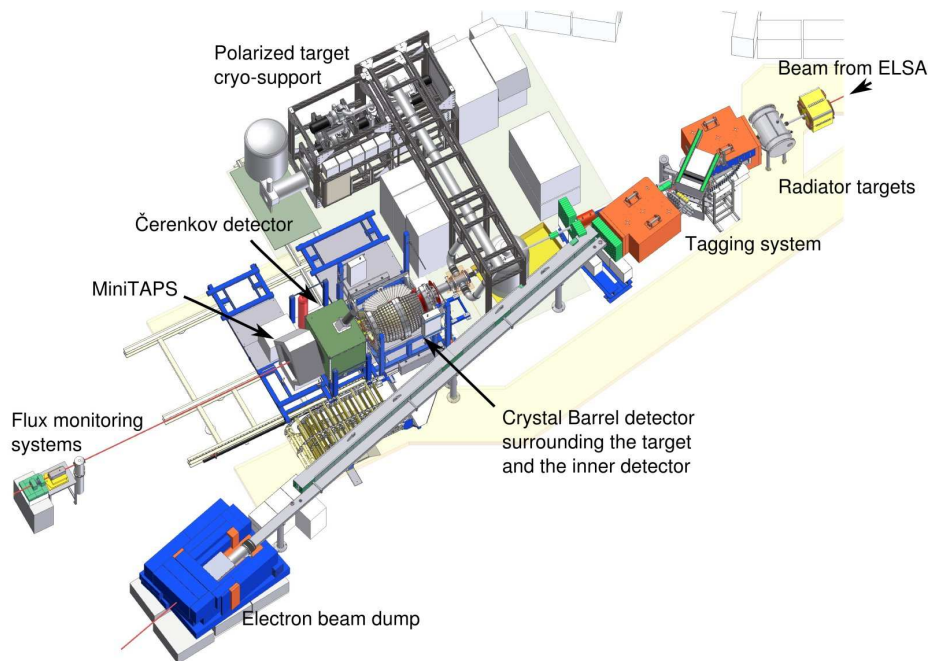


Figure 2.1: Overview of the experimental area of the Crystal Barrel experiment. Coming from the accelerator, the electron beam enters the area from the top right. The photon beam is created at the radiator target, afterwards it passes the tagging system and is then impinging on the target inside the Crystal Barrel detector. Finally the flux monitoring systems constitute the end of the beam line.

This section gives an overview of the Crystal Barrel experiment. The overall structure of the experiment can be divided into three main parts. First there are the facilities for the creation of the polarized photon beam (Section 2.1). Second there is the polarized target (Section 2.2) and finally there are the different subdetectors to detect and characterize the decay particles (Section 2.3). An overview of the experimental area is shown in Figure 2.1.

## 2.1 The polarized photon beam

As was already discussed in detail in Chapter 1, the Crystal Barrel experiment uses the mechanism of photoproduction. Hence one fundamental precondition is the generation of a directional photon beam with energies in the order of GeV. Furthermore the single photons should be of known energy and for double polarization studies it is important that the beam can be polarized and the degree of polarization is known. There are two common ways of obtaining such a photon beam – namely laser Compton backscattering or bremsstrahlung. At the Crystal Barrel experiment the bremsstrahlung method is used to produce real photons. Both approaches require an accelerator to supply a high energy electron beam.

### 2.1.1 The electron accelerator

The Electron Stretcher Accelerator (ELSA) uses several steps to accelerate the electrons to the desired energies (see Figure 2.2). In a first step the electrons are accelerated in a linear accelerator to relativistic energies of about 20 MeV before they are injected into the booster synchrotron. The booster offers an energy range from 500 MeV to 1.6 GeV and is used as an injector for the stretcher ring. The latter overcomes the problem of a low duty factor due to the pulsed operation of the booster synchrotron (duty factor  $\sim 5\%$ ). The booster is used to homogeneously fill the stretcher ring, where the electrons reach the desired energy after an additional acceleration. From the stretcher ring a continuous and slow extraction over several seconds is possible. The duty factor is increased up to values of 60-70% for typical hadron physics scenarios. This operation allows a maximum possible electron energy of 3.5 GeV. The energy is primarily limited by the bending power of ELSA's dipole magnets and the RF generated acceleration voltage. The maximum beam current is in the order of  $\approx 1$  nA at typical energy of 3.2 GeV [23].

### The polarized source

The ELSA facility features a polarized electron source to supply spin polarized electrons. The source uses the light of a pulsed Ti-Sa laser impinging on a single Be-InGaAs/Be-AlGaAs strained-layer superlattice photocathode with a typical quantum lifetime of more than 3000 h. A typical polarization of approximately 80 % is possible at the source. The electron spin orientation is manipulated several times during the process of acceleration. However, it is adjusted to be longitudinally polarized upon extraction to the experimental area. Due to depolarizing intrinsic- and imperfection resonances in the accelerator, polarizations in the experimental area are less than 80 %. The polarization at the radiator target is energy dependent (see Section 2.1.2). At an energy of 2.4 GeV a polarization of 55 % can be achieved. A thorough description of the source is given in [10, 22].

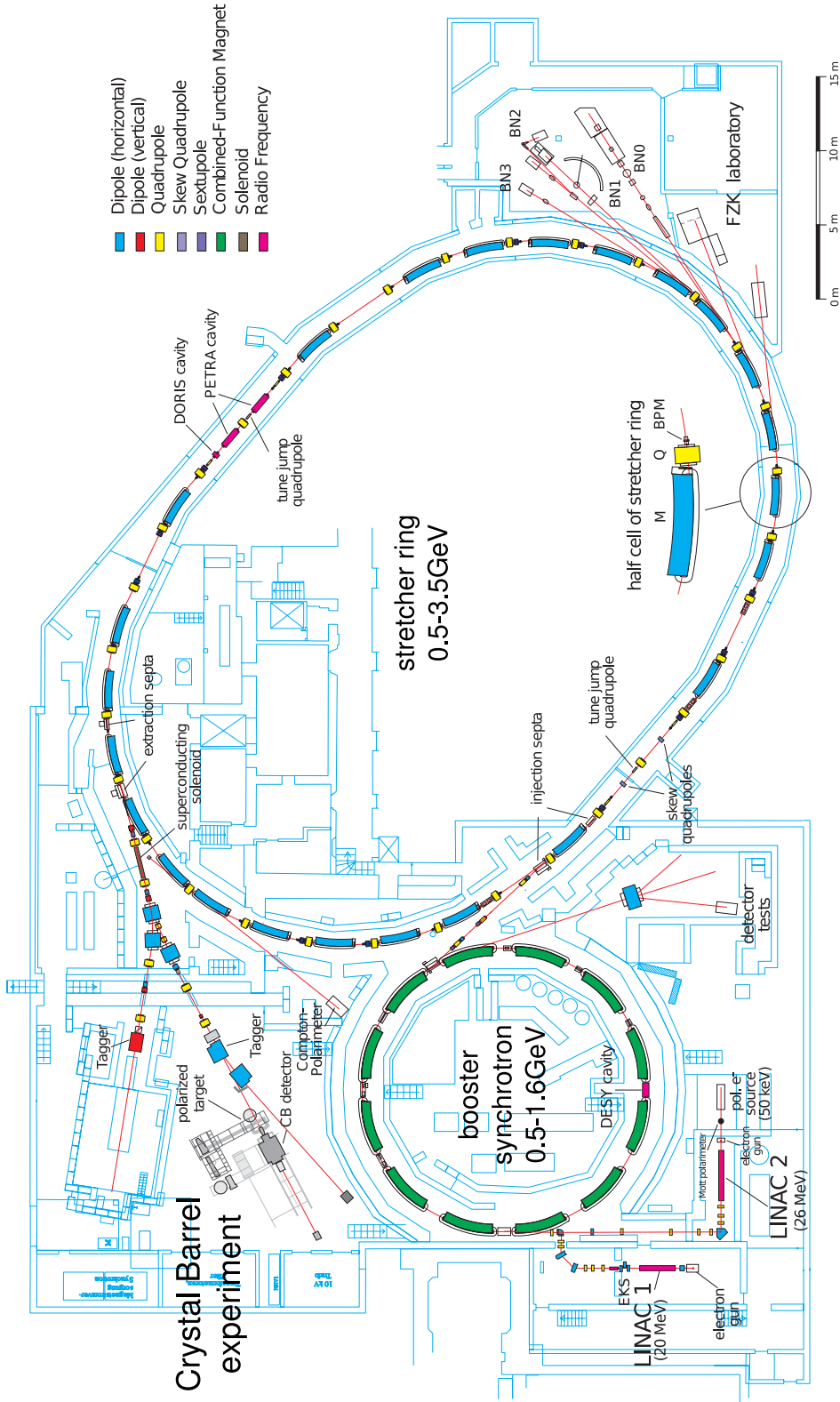


Figure 2.2: ELSA floor plan.

### 2.1.2 The radiator targets and possible modes of operation

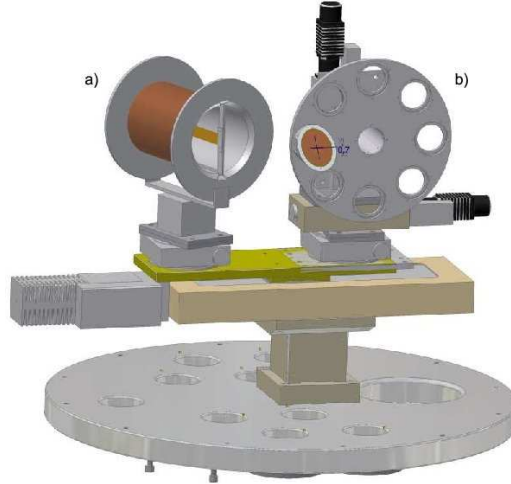


Figure 2.3: The target-structure is mounted on a goniometer. It holds the Møller coil with an amorphous radiator inside (a) and the target wheel (b) housing multiple different targets in the outer ring and the diamond radiator in the center of the disc.

To generate a photon beam from the beam of highly energetic electrons, the Crystal Barrel experiment uses the bremsstrahlung process. That means that the high energy electrons are decelerated in a radiator target – not unlike in the case of an X-ray tube. Various different radiator targets are mounted on the target structure. The structure is remote controlled and can expose and precisely align the different targets to the primary electron beam.

A beam of unpolarized photons is the most trivial case. In that case an amorphous target (usually copper foil) is used in combination with an unpolarized electron beam. Several foils with a different thickness can be chosen from the target wheel (see Figure 2.3 b) to optimize the ratio between photon rate and multiple scattering. The latter effect is unwanted. The reason why is outlined in Section 2.1.3.

Circularly polarized photons can be supplied to the experiment by using the combination of an amorphous target and a longitudinally spin-polarized electron beam [38]. In this case the radiator target is put in an external field (see Figure 2.3 a) to allow constant monitoring of the degree of beam polarization via the Møller effect. The details of the method are explained in [28].

Finally the linearly polarized photon beam is created by exploiting a process called coherent bremsstrahlung. The vector of the momentum transfer  $\vec{q}$  of the bremsstrahlung process has to be matched carefully to the reciprocal lattice vector  $\vec{g}$  of a periodic structure. In contrast to incoherent bremsstrahlung where the electron scatters off a single isolated atom, in the coherent case the whole lattice

is the scattering partner. By carefully choosing the orientation of the lattice and the momentum of the incident electrons  $\vec{p}_0$  it is possible to select only certain  $\vec{q}$  vectors that are kinematically allowed to contribute. The photons emitted by this process are linearly polarized in the plane defined by  $\vec{g}$  and  $\vec{p}_0$ . The coherent bremsstrahlung adds to the incoherent bremsstrahlung spectrum. In the kinematically allowed regime the photon beam has a net polarization.

In the case of the Crystal Barrel experiment a diamond is used. It is located in the center of the target wheel. The whole target structure is equipped with a very precise goniometer. This makes it possible to align the diamond crystal very precisely along all three rotational axes. A detailed description of the process is given in [11].

### 2.1.3 The tagging system

The task of the tagging system is to mark or *tag* the created photons according to their energy. In the case of single scattering events, the primary electron energy  $E_0$  is split according to

$$E_0 = E_\gamma + E_e$$

between the photon ( $E_\gamma$ ) and the electron ( $E_e$ ). Therefore it is possible to indirectly measure the photon energy by dint of measuring  $E_e$ .

Behind the radiator target the electron and the photon beam are superimposing each other. The electron energy can be determined by simply directing both beams through the field of a dipole magnet that is aligned perpendicular to the direction of motion. Here the charged electrons are deflected by the Lorentz force, while the photons remain unaffected. This serves a double purpose. First this is a simple way of separating the photon beam from the electrons. Second as the force is momentum dependent, determining the exit angle of the electron from the magnetic field also contains its energy information  $E_e$ . The trajectory of the electron is determined using a tagging hodoscope. It is an array of organic scintillators that are used to detect the electron track behind the magnetic field (see Figure 2.4).

The tagging system is one of the most important subdetectors of the experiment as it defines the initial state energy of any potential reaction. Due to its high time resolution it acts as the time reference for the trigger system and therefore for the whole experiment. It also plays an important role in the photon flux determination of the experiment (see also [21]).

The beam of electrons that did not interact in the radiator target is bent away by the tagging magnet and a second adjustable dipole magnet further downstream. This beam is guided to and absorbed at the beam dump to avoid unnecessary interactions with the environment that could give rise to background reactions affecting the experiment. Behind the tagging system the photon beam is further narrowed by an interchangeable tungsten collimator of variable diameter before finally impinging on the target.

## 2 The Crystal Barrel experiment

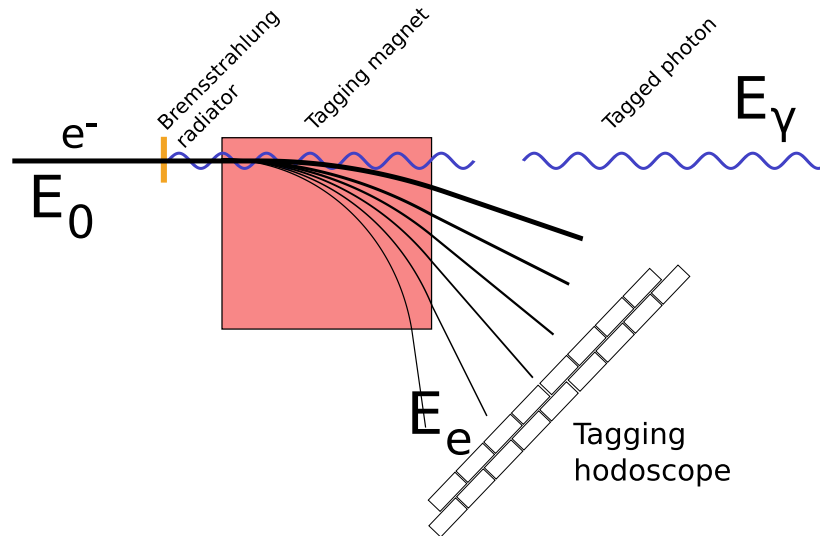


Figure 2.4: Working principles of the tagging system. Electrons of known energy  $E_0$  impinge on a radiator and create bremsstrahlung. By measuring the angle of deflection in a magnetic dipole field the energy of the bremsstrahlung photon  $E_\gamma$  can be reconstructed.

### 2.2 The polarized target

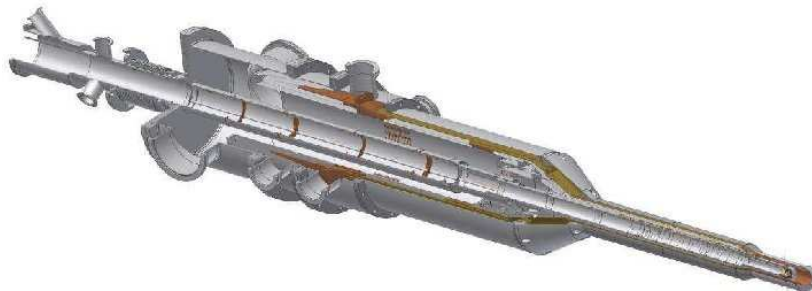


Figure 2.5: The polarized target cryostat. The beam enters the structure from the left. The target is located close to the tip at the right hand side, which is located at the geometrical center of the Crystal Barrel detector.

The task of the target is to supply polarized protons for double polarization experiments. The Bonn frozen-spin target uses frozen butanol that is chemically endowed with a water-porphyrine solution. This additive yields  $1.82 \times 10^{19}$  electron spins per  $\text{cm}^3$  that can be manipulated by means of an outer magnetic field. With the help of microwave radiation, the polarized spin of the electrons is then transferred to the protons in the hydrogen atoms of the material. At the same time the thermal relaxation is kept at a minimum by cooling the target to

approximately 30-50 mK in the cryostat (see Figure 2.5). With this method the Bonn frozen-spin target achieves polarizations up to 80-85 % with decay times of typically a few hundred hours. The target is described in detail in [7].

### 2.2.1 Additional targets

In addition to the frozen Butanol target the experiment can also operate with different unpolarized targets. Currently a liquid hydrogen ( $\text{LH}_2$ ), a liquid deuterium ( $\text{LD}_2$ ) and a carbon target are available. As a pure proton target the  $\text{LH}_2$  can be used for very clean measurements that are used for the normalization of the Butanol measurements. Likewise the  $\text{LD}_2$  adds the effect of the neutron to this measurement. Finally measurements on the carbon can be used for background subtraction from the butanol measurements [47].

## 2.3 The subdetectors of the experiment

To detect the decay products of the hadronic reactions the target is surrounded by various detectors. The most important detectors are the electromagnetic calorimeters, namely the Crystal Barrel detector (Section 2.3.2), the Forward Plug detector (Section 2.3.3) and the MiniTAPS detector (Section 2.3.5). To distinguish whether a hit in one of the calorimeters was neutral or caused by a charged particle, each calorimeter is equipped with its affiliated charged particle identification system. The inner detector of the Crystal Barrel calorimeter is responsible for the charged particle detection for the main calorimeter (see Section 2.3.1). The Forward Plug and MiniTAPS also feature dedicated organic scintillation detectors specifically for charged particle detection.

For measuring absolute cross sections, the precise knowledge of the initial photon flux is crucial. The detectors that serve that purpose are described in Section 2.3.6.

Finally a gas Čerenkov detector is used to suppress electromagnetic background reactions on trigger level (see Section 2.3.4).

### 2.3.1 The inner detector

The inner detector of the Crystal Barrel consists of 513 organic scintillating fibers. The fibers are arranged in three layers and are read out by multi-anode photomultipliers. A picture of the detector is shown in Figure 2.6. The layers are contorted such that the detector provides a track point for charged particle hits with a spatial resolution of  $\delta x < 1.6$  mm. The detector system plays an important role for the first level trigger (see Section 2.4). A detailed description of the detector is given in [46, 16].

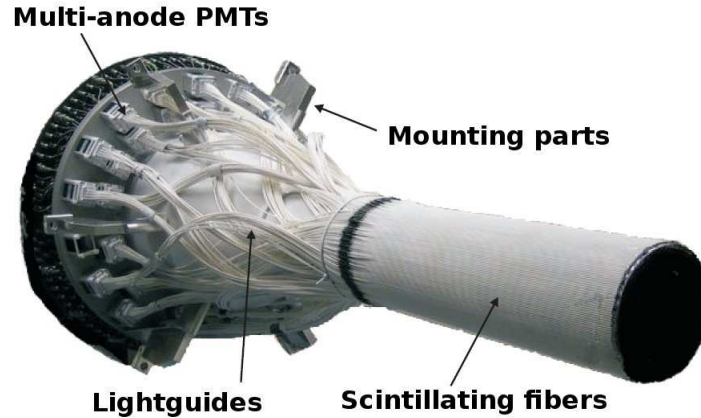


Figure 2.6: Overview of the inner detector. The light created by the scintillating fibers is directed backwards using lightguides. Here it is read out by the multi-anode photomultiplier tubes (PMTs).

### 2.3.2 The main calorimeter

The Crystal Barrel detector [1] is an electromagnetic calorimeter. It currently consists of 1230 Thallium doped CsI scintillator crystals (see Figure 2.7) that are read out by photodiodes (see Sections 3.1.2 and 3.2.1). The detector covers a  $\theta$  range from  $30^\circ$  to  $156^\circ$  and the full  $2\pi$  angle in  $\phi$ -direction [52]. The segmentation of the detector allows the acquisition of spatial hit information.

### 2.3.3 The Forward Plug detector

The Forward Plug consists of three rings and a total of 90 CsI(Tl) crystals (see Figure 2.8). It covers  $10^\circ - 28^\circ$  in  $\theta$  and  $2\pi$  in  $\phi$ . The detector crystals were originally constituting the forward section of the main calorimeter. The corresponding crystals were removed and fitted with a photomultiplier readout and additional organic front scintillators for charged particle identification. The whole unit now represents the Forward Plug detector.

In fixed target experiments, subdetectors in forward direction receive the highest rates. When triggering on the whole detector is not feasible, it is especially efficient to trigger on subdetectors in the forward direction. This being the reason to build the Forward Plug, it is now used in the first level trigger. A detailed description of the Forward Plug detector and the readout is given in [52, 14].

### 2.3.4 The Čerenkov detector

The gas Čerenkov detector uses  $\text{CO}_2$  as its active medium. It is sensitive to electrons and positrons and covers the same  $\theta$  angle like the MiniTAPS detector (see Section 2.3.5). Pair production is the dominant background reaction. Electron positron pairs are mostly created in the target or the beam pipe. The detector

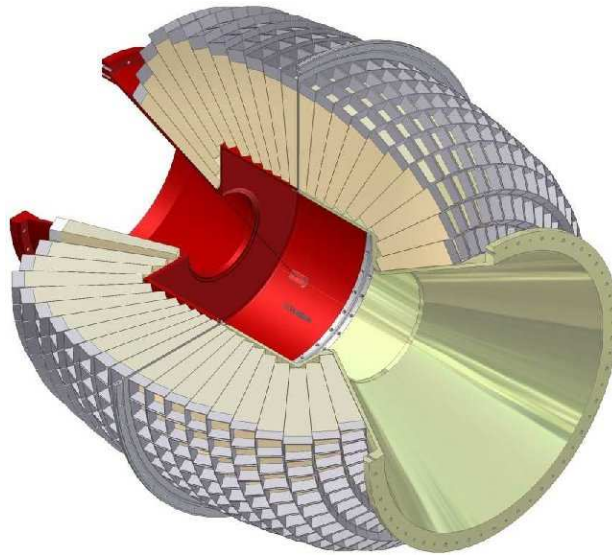


Figure 2.7: The main calorimeter. 1230 CsI(Tl) crystal scintillators read out by photodiodes surround a cylindrical cavity in the center.

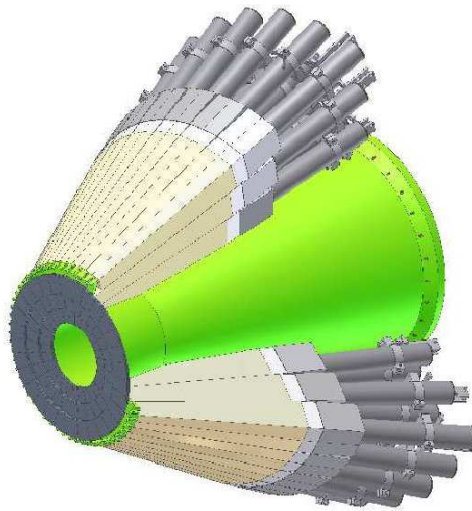


Figure 2.8: The Forward Plug detector. The ring arrangement of front organic scintillation detectors serves for charged particle identification.

## 2 The Crystal Barrel experiment

has a single photomultiplier channel and the fast response allows its use as a veto in the first level trigger. Thus the first level trigger is made more selective to minimize dead time. Due to its high time resolution it is also used as a time reference for tagger time calibrations [21]. A detailed description of the system is given in [27].

### 2.3.5 The MiniTAPS detector

The Two Arm Photon Spectrometer (TAPS) built at the University of Giessen is an electromagnetic calorimeter consisting of 216 hexagonal BaF<sub>2</sub> crystals. It is located in forward direction covering a solid angle of  $1.5^\circ < \theta < 12^\circ$  (and  $2\pi$  in  $\phi$ ). Therefore it closes the gap between the Forward Plug and the beam line. Each crystal is read out by a photomultiplier and has an organic front scintillator for charged particle identification. The detector system is described in detail in [32, 35].

### 2.3.6 Flux monitoring

The end of the photon beam line is marked by two detectors dedicated to flux monitoring. The gamma intensity monitor (GIM) consists of 16 lead fluoride crystals read out by photomultipliers. The Čerenkov light response of the GIM crystals is fast enough to resolve the photons of the primary photon beam in time [33].

However, as the detector shows saturation effects at very high rates a second detector has been built to support the GIM. The Flux Monitor (FluMo) is a combination of thin organic scintillation counters with a converter target. Electron positron pairs are created in the target and detected by the scintillators. Since only a certain fraction of all photons causes pair production in the converter, the rate is reduced by orders of magnitude in comparison to the GIM. Hence it is possible to measure at much higher rates [9].

## 2.4 Trigger and data acquisition

There are essentially two ways of running the data acquisition (DAQ) of an experiment. One is the *free running* way and one is the *gated mode*. Although mixed forms are possible the classical free running experiment will store all data recorded by all subdetectors at all times. In this approach it is the task of the offline analysis to filter the relevant information from the recorded data.

In a triggered DAQ an on-line preselection is made by the trigger logic. The trigger electronics constantly monitors and evaluates various detector signals in search of the signature of a potentially interesting event. If one of such predefined trigger condition is met, the readout is triggered. The DAQ is then responsible for saving all relevant data of this event. Usually the DAQ system will lock itself while being busy and therefore not accept any new trigger signal at this stage. This

busy-time of the DAQ and also the trigger logic itself is called dead-time. Apart from the reduced amount of unnecessary data, this approach has the advantage that it allows to efficiently introduce the parameter of time<sup>1</sup> into the readout.

The Crystal Barrel experiment runs in gated DAQ mode and the trigger of the experiment is based on a two level scheme. In the present case the first level trigger can either start the data readout directly or invoke the second level trigger. The second level trigger now has access to more information than the first trigger level. The tradeoff is that it causes dead-time for each event it discards. If the event complies with the trigger condition the dead-time produced by the second level trigger is negligibly small compared to the conversion- and readout time.

The reactions relevant for the experiment generally involve at least two photons and a recoil proton in the final state. Typical reactions of that type are  $\gamma p \rightarrow p\pi^0 \rightarrow p\gamma\gamma$  or  $\gamma p \rightarrow p\eta \rightarrow p\gamma\gamma$ . To trigger on these reactions one could require particle energy deposits (PEDs) of three or more particles in the calorimeters. However, if only two PEDs are required by the trigger condition, also events are acquired where one of the participating particles is lost in an acceptance hole of the experiment. Due to the high energy resolution for photons, the four vector of a lost recoil proton can be reconstructed in the off-line analysis. Unfortunately this is not possible for a lost photon. In that case the event is recorded but cannot be analyzed. Since more complicated reactions generally involve larger numbers of particles in the final state, it is even more likely to satisfy the two PED requirement.

In general the trigger condition for production runs requires two PEDs or clusters<sup>2</sup>. The task of the trigger electronics is to count the number of PEDs  $n$  and in case of  $n \geq 2$ , raise the trigger condition.

The first level trigger of the Crystal Barrel experiment bases its decision on information from the inner detector, the Forward Plug, the MiniTAPS, the tagging system and the gas Čerenkov detector which can veto the readout. The Forward Plug detector and MiniTAPS have their dedicated cluster finding logic that is connected to the central first level trigger module. In the case of a hit both detectors discriminate between one or two (and more) PEDs. The inner detector contributes a single signal indicating one or more hits. Similarly also the Čerenkov detector supplies one single signal. All subdetectors have to be timed to supply this information 225 ns after the event (see Figure 2.9). The time is matched to the fixed delay in the analog signal lines of the Crystal Barrel detector. The main calorimeter is currently not part of the first level trigger, because the signals of the preamplifier of the current photodiode readout rise too slowly to meet this timing constraint. A first level trigger condition is raised if at least one PED was seen in either MiniTAPS, the Forward Plug or the inner detector and at the same time the Čerenkov did not fire.

---

<sup>1</sup>Time in this context is usually understood as the relative time difference of a special occasion during the course of an event, to the point of time when the trigger condition was raised.

<sup>2</sup>The electromagnetic shower of a photon in the calorimeter generally affects several crystals, thus forming a *cluster*.

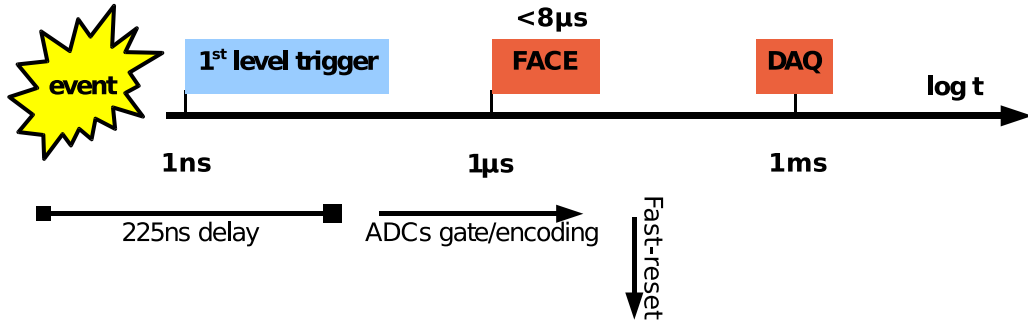


Figure 2.9: Timeline of an event as it appears to the current Crystal Barrel trigger and readout. The main contribution to dead-time arises from fast-resets and the readout of the ADCs.

The second level trigger is based on the output of the first level trigger and the Fast Cluster Encoder (FACE). The latter is a set of logic circuits that perform cluster counting on the hit pattern of the main calorimeter. Similar to the cluster finding logic of Forward Plug it is capable of signalling the number of clusters to the central trigger module. A full description of the function and design of the application-specific integrated circuit of FACE is given in [12].

When the first level trigger condition is raised two things can happen. The second level trigger module can receive a bypass signal in the case that two (or more) PEDs were already found by the first level trigger. Otherwise the first level trigger supplies the minimum number of clusters that have to be found in the main calorimeter – either one or more. At the same time the ADCs receive their gate which causes them to readout the analog signals that now arrive from their delay lines. If FACE is bypassed, the ADCs are read out as soon as they have finished digitizing ( $\approx 1$  ms). If the inner detector has signalled at least one charged particle or if the number of PEDs found by the first level trigger  $n_{\text{firstlevel}}$  satisfies the relation  $n_{\text{firstlevel}} = 1$ , the second level trigger logic waits for the results from FACE  $n_{\text{face}}$ . This step takes  $5 \mu\text{s}$  on average but might take up to  $8 \mu\text{s}$  depending on the number of clusters found in the main calorimeter. If now the inequality  $n_{\text{firstlevel}} + n_{\text{face}} \geq 2$  can be satisfied the data acquisition is triggered. If the condition cannot be fulfilled, the ADCs receive fast-reset signals ( $2 \mu\text{s}$ ) and the trigger unlocks itself. The 1 ms readout time of the ADCs adds to the dead time, which cannot be avoided with the present ADCs. The relative time scales involved in the trigger and the readout are illustrated in Figure 2.9.

The two trigger levels are realized in two distinct Field Programmable Gate Array (FPGA) modules that were specifically developed for this purpose. The FPGAs allow a quick and flexible alteration of the trigger conditions if needed during the experiment. A detailed description of this module is given in [53].

### 2.4.1 Benefits and requirements of a new readout

The current trigger/readout scheme has certain disadvantages. First of all, since the first level trigger can fire upon a single charged particle in the inner detector, the acquisition of photoproduction reactions on the neutron are suppressed by the trigger (see Figure 2.10). Second, unwanted electron positron pairs that are created in the target or the beamline can mimic protons in the inner detector. Such events invoke false first level triggers. Generally this background event is then discarded by the second level trigger. A lot of dead time is created by this so called fast-resets. Each fast-reset contributes more than  $5 \mu\text{s}$  to dead-time. Many fast-resets are avoidable by a more selective first level trigger.

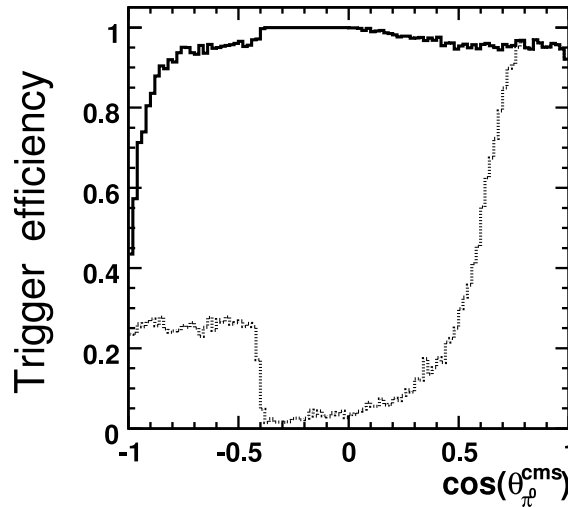


Figure 2.10: Comparison of current- (dotted) and possible trigger acceptance (solid) for photoproduction off the neutron for the reaction  $\gamma n \rightarrow n\pi^0$ . Putting the main calorimeter in the first level trigger will result in a trigger efficiency close to one for almost the full  $\theta$  range. That would be almost identical to the current trigger efficiency for photoproduction off the proton. Plot taken from [4].

In conclusion it would be very desirable to make the hit information from the main calorimeter available to the first level trigger. Doing so would result in a completely new trigger scheme, where FACE would play a totally different role. This step would widen the trigger efficiency for photo production off the neutron. Seeing the recoil proton could be abandoned as a trigger condition for large parts of the solid angle (compare Figure 2.10). It might even be possible to completely abandon the second trigger level if one could remedy the generally long times arising from any clusterfinding algorithm. The hit information would also allow suppression of the electromagnetic background. First calculations suggest that

## 2 The Crystal Barrel experiment

suppression by a factor of 400 is realistic [48].

Another problem of the Crystal Barrel readout is related to the data readout from the ADCs. The long conversion- and readout times of approximately 1 ms (see Figure 2.9) are dead-time. The slow ADC readout inherently limits the readout rate to 1 kHz maximum. Faster ADCs could help to significantly speed up the readout rate.

To approach the problem of the slow readout and the resulting long dead-times, a free running energy readout would be the solution of choice. The basic concept of FADCs already comes very close to this idea. It could be argued that such a readout would also resolve the latency constraint of the first level trigger. Digital delays can be easily realized in FADCs and are only limited by memory. A memory delay can easily last for several  $\mu\text{s}$ , which could be used to loosen the first level trigger time constraint. However, in that case other subdetector systems, like the tagger or the GIM, with their existing multi-hit TDCs become the limiting factor. As no upgrades are planned for these detectors, they would impose a new time constraint of the order of  $1 \mu\text{s}$  that should still be met by the first level trigger.

The fundamental requirement for a first level trigger that includes the main calorimeter, is a signal from the main calorimeter crystals that has a faster risetime than the present readout. Section 3.2 will describe the present readout in detail and introduce avalanche photodiodes as a possible remedy to this timing problem.

### 2.5 The Studentenexperiment

Despite the fact that the Studentenexperiment is not an experiment aiming at serious scientific progress, this work had an impact substantial enough on the experiment to justify its mention here. Likewise this thesis was impacted by several measurements conducted during the dedicated beam time for the experiment. The Studentenexperiment is a course for graduate students that is held annually. It aims at setting up a small experiment to observe the  $\Delta(1232)$  resonance via its symmetric decay channel  $\Delta \rightarrow p\pi^0 \rightarrow p\gamma\gamma$ .

In the past years the experiment was performed using mainly technology that is or at least was also used for the Crystal Barrel experiment. Lately in 2008 the Studentenexperiment also became a test bench for new detector developments. The first APD readout was fitted to the crystals that are generally reserved for this experiment. The fast trigger capability with the new APD based readout was tested in the course of this experiment. Section 5.6 will deal with the details of the measurements that were carried out in this context.

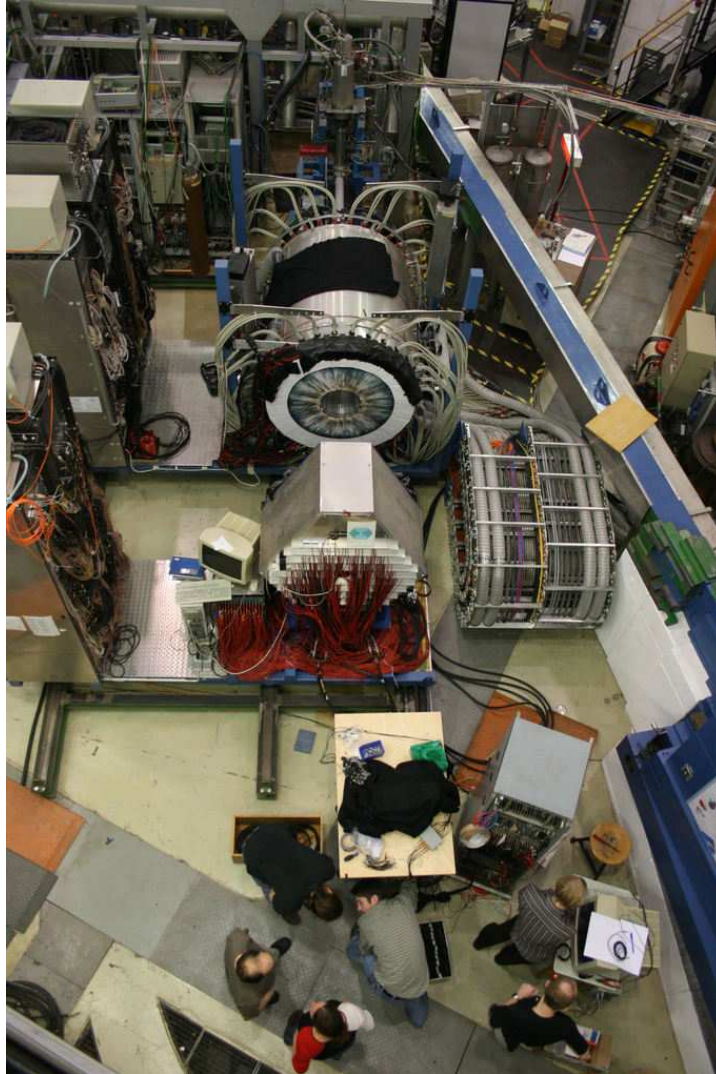


Figure 2.11: Students setting up the Studentenexperiment at the beamline behind the MiniTAPS detector. The detectors on the table are covered with black cloth to keep ambient light from leaking into the crystals.

## 2 *The Crystal Barrel experiment*

## 3 The crystal light readout

### 3.1 Scintillation detectors

Generally a scintillation detector consists of a scintillating material which is optically coupled to a photodetector. Radiation that passes through the scintillator excites its atoms or molecules. That causes the material to emit light that is transmitted to the photodetector. That could for instance be a photomultiplier tube (PMT) or an avalanche photodiode (APD), like it is the case in this work. Here the photons will induce a weak photocurrent which then is amplified in a process of electron multiplication. This chapter will give an overview on inorganic scintillators and photodetectors.

#### 3.1.1 Inorganic scintillators

Although there is a great variety of scintillators, the following discussion will focus on the category of inorganic scintillators. For the present thesis, this is the relevant type of scintillator. The Crystal Barrel detector in particular uses CsI(Tl) as a scintillating material where Thallium (Tl) is the so called *impurity activator*. Most inorganic crystals exhibit the phenomenon of phosphorescence which means that after being excited, their afterglow persists for a period of time that reaches into the regime of microseconds. In general they are 2-3 orders of magnitude slower than the organic equivalents. In the organic case whole molecules rather than atoms are excited. Molecules, thanks to their great variety of possible states, tend to have much shorter decay times than inorganic scintillators, where the light emission always proceeds via so called excitons.

The great advantage of inorganic scintillators on the other hand is their high stopping power and their good light output. This arises from their high atomic number and matter density. Therefore inorganic scintillators are usually the first choice for photodetection. High stopping power means that it is very likely for a photon to interact with the material. For high energy photons ( $E_\gamma \gg 1\text{MeV}$ ) such interactions will preferably lead to the formation of  $e^+e^-$  pairs. These on the other hand are also very likely to interact with the crystal, thus forming new photons by bremsstrahlung. Given the particles involved still have enough energy at this point, the cycle starts all over again. This energy loss mechanism of high energy photons (and  $e^\pm$  respectively) is a phenomenon commonly referred to as an electromagnetic shower.

It is obvious that, in the process a lot of charged particles ( $e^\pm$ ) are created within the bulk material. These particles cause ionization of the crystal's atoms.

### 3 The crystal light readout

In inorganic crystals the scintillation mechanism is a direct consequence of the electron band structure. Ionization can either lift an electron from the valence band to the conduction band, thus creating a particle hole pair, or it can create an exciton by exciting the electron to the exciton band which lies just below the conduction band. An exciton is a quasi particle formed by an electron hole pair. It can travel freely through the crystal lattice. Whenever an exciton has an encounter by chance with an impurity activator, deexcitation is possible by emission of scintillation light. Because the impurity activators are sparse throughout the material the crystal remains transparent for this designated wavelength. It is in this way that scintillation light is generated [29].

#### 3.1.2 The Crystal Barrel crystals

While NaI(Tl) is probably the most commonly used inorganic crystal in high resolution calorimetry, CsI(Tl) features a higher stopping power. It has an about 30% shorter radiation length  $X_0$  and at the same time greater light output than NaI(Tl) [54]. Being less hygroscopic it is easier to design appropriate housings for the crystals. This was important for the mechanical support structure of the detector. The CsI(Tl) of the Crystal Barrel detector alone weights about 4 t.

The crystal dimensions were chosen as a compromise between energy resolution at high energies and needed space. Also mechanical considerations were playing a major role in the decision making. All crystals have a fixed length of 300mm ( $16.1X_0$ ) capable of longitudinally containing a shower of a  $\gamma$  particle with  $E_\gamma = 2$  GeV to more than 99%.

The whole crystal is wrapped in white Teflon foil for diffuse reflectivity. On top of that a titanium layer is holding the crystal in position and acts as a light seal. Attached to the end of the structure is the readout end-cap. The end-cap houses the wavelength shifter, the photodiode and preamplifier as the first stage of the readout electronics. This structure will be described in more detail in Section 3.2.1.

There is a total of 1380 scintillating crystals that were in use when the Crystal Barrel was still operated at LEAR [1, 6]. Today the setup uses less crystals in backward direction and for small forward angles, thus leaving space for the inner detector and the target. The Crystal Barrel currently consists of 1230 crystals [52]. The elements that have been removed are available for prototype developments and testing. Most studies in this work were carried out using such crystals.

## 3.2 Photo detectors

After having discussed how light is created from radiation passing through matter with scintillating properties, the photodetection part will now be reviewed in more detail. The aim of a photodetector is to convert the photon response of a detector into an electronic signal.

Most photodetectors convert the incidental photons to photoelectrons as a first step. While a PMT will do so utilizing the outer photo-electric effect, an APD will do so via the internal photo-electric effect. That means an electron hole pair is created in the depletion layer of the diode.

The second step is to amplify the weak photocurrent. Usually this is done by an electron multiplication process, as in the case of the PMT or the avalanche photodiode. These devices make use of the avalanche effect. In an APD a photo-electron is sufficiently accelerated to energies high enough to free further charge carriers from the bulk material. Because of the chain-reaction character of this process it is commonly referred to as the *avalanche effect*. A photodiode in strong contrast, does not have an intrinsic gain. Because the primary signal of the photodiode is very weak, it needs a very sensitive preamplifier before the signal can be processed. More information on the fundamentals of photodetection is given in [19].

Avalanche photodiodes have a special role. Since their gain is significantly higher than one, but also a lot smaller than that of PMTs, their signal still needs to be amplified. They also have very special requirements in terms of the stability of the bias voltage and ambient temperature (see Figure 3.1). However their great advantage over PMTs is that they can be operated in a strong external magnetic field. This is generally not possible for PMTs. For most applications of an APD readout, the intrinsic gain mechanism is combined with a charge sensitive preamplifier (see Section 4.3).

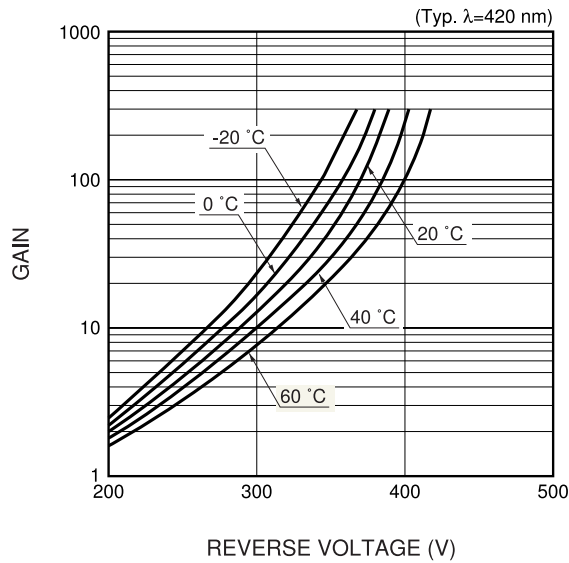


Figure 3.1: Voltage and temperature dependence of Si APD, taken from Si APD datasheet [18]. The gain of the APD rises for higher bias voltages. Yet, it falls for higher temperatures. In the final setup the temperature dependence will be corrected by adjusting the HV [45].

### 3.2.1 The current photodiode readout

The readout of the Crystal Barrel calorimeter is currently conducted via photodiodes. This part of the readout still dates back to the time, when the detector was located at CERN's Low Energy Antiproton Ring.

Initially the critical decision to use photodiodes instead of PMTs was made with regard to the magnetic field that surrounded the detector. The field allows the measurement of the transverse momentum  $p_t$ . The crystals are read out with the Hamamatsu S2575 PIN silicon photodiode that is flange-mounted to the side of the wavelength shifter (WLS). Although the CsI(Tl) light output, which peaks at a wavelength of around  $\lambda_{\text{CsI}} = 550 \text{ nm}$ , matches the photodiode's most sensitive range very well, the WLS is used as a light collection system. It absorbs primarily at a wavelength around 530 nm and uniformly re-emits into a longer wavelengths where the crystal is less likely to re-absorb the light (transmission around 90% for  $\lambda \approx 620 \text{ nm}$ ) [1]. As a consequence less light is lost due to re-absorption and a better spatial homogeneity of the light collection process is achieved. Tests have shown, that one  $1 \text{ cm}^2$  photodiode with WLS performs as well as four  $1 \text{ cm}^2$  photodiodes attached directly to the crystal end face [50].

The signal of each photodiode is fed into a charge sensitive preamplifier that is housed in the end-cap of the crystal (see Fig. 3.2). The integrated signal is then sent out of the detector structure via an differential output. A complete description of the readout is given in [1].

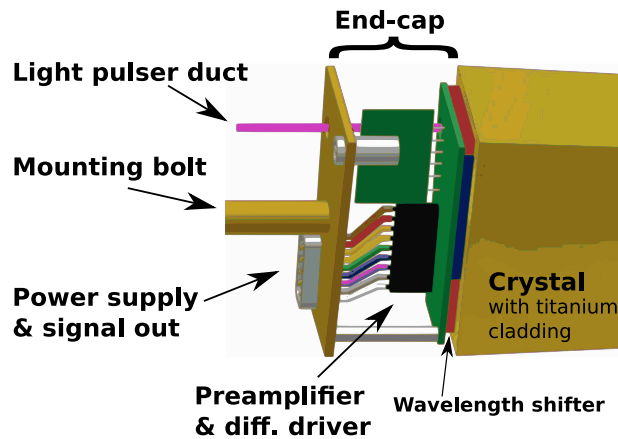


Figure 3.2: Schematic view of the end-cap for the photodiode readout as it is currently used at the Crystal Barrel detector. The end-cap contains the wavelength shifter, the photodiode and the preamplifier. The whole crystal is held in place by the mounting bolt attached to the end-cap. A light pulser duct is included for the relative calibration of the detectors.

## 4 Initial situation and equipment

### 4.1 The Hamamatsu S8664-1010 Si APD

In the present work the Hamamatsu S8664-1010 Silicon APD was used for all tests. This type of APD has been developed for the Electromagnetic Calorimeter (EMC) of  $\bar{P}$ ANDA at FAIR. It is a Large Area Avalanche Photo Diode (LAAPD) with an active area of  $10 \times 10 \text{ mm}^2$  in a ceramic housing. The internal design is based on the reverse biased diode used in the CMS electromagnetic calorimeter. It features a quantum efficiency of 70% at 420 nm and exhibits a capacitance of 270 pF at a gain of 50. At the same gain the diode has a dark current of approximately 10 nA at ambient temperatures. A thorough discussion of the device is given in [18, 37].

### 4.2 The prototype crystal end-cap

For the APD test readout a new end-cap was designed to house the APD and the case for the 18 mm standard printed circuit board of the associated preamplifier (see Figure 4.1). The design and manufacturing of these parts was done at the workshop of the University of Giessen. The construction offers room for a dual APD readout. Due to the relatively high light output of CsI(Tl) compared to PbWO, photon statistics was not the limiting factor of the readout. Therefore only one APD per crystal was used for all tests in this work.

### 4.3 The Basel LNP preamplifier

In the present work the readout of the APDs is conducted via the low noise/low power charge integrating preamplifier (LNP preamplifier), which was developed at the University of Basel for the  $\bar{P}$ ANDA electromagnetic calorimeter. A picture of the printed circuit board can be seen in Figure 4.2. This circuit was specifically adopted to the APD readout of CsI(Tl) crystals.

The charge sensitive amplifier linearly converts the charge signal of an LAAPD to a voltage that can then be fed into consecutive electronics. Integrating amplifiers are generally characterized by the time constant  $\tau_{\text{int}}$ . The time constant has to be matched to the shape of the signal for proper operation. As the APD responds very quickly to the detected photon flux, the signal response is governed by the crystal itself. Therefore the time constant has to be adjusted to the crystal rather than to the APD. The decrease in light output of scintillators can be

#### 4 Initial situation and equipment

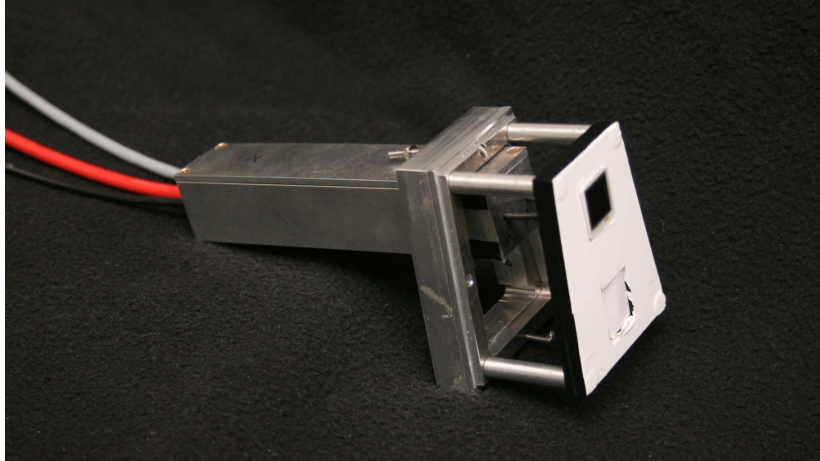


Figure 4.1: Prototype APD readout end-cap. The end-cap allows to simultaneously house two APDs. However, during all tests it was only equipped with one. The metal box contains the LNP preamplifier.

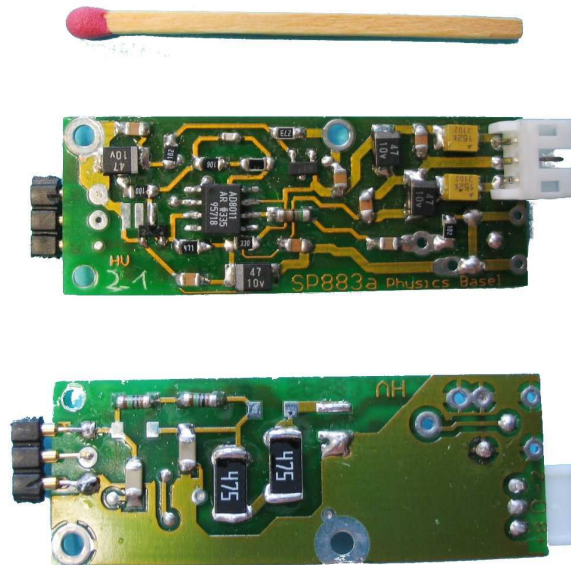


Figure 4.2: Front- and back plane of the LNP preamplifier. By courtesy of M. Steinacher [45].

characterized by the exponential decay constant  $\tau$ . The lightout of PbWO<sup>1</sup> as used at  $\bar{P}$ ANDA decays with  $\tau_{\text{PbWO}} \leq 50$  ns [54]. Thallium doped CsI(Tl) on the other hand has an much slower intrinsic decay constant of  $\tau_{\text{CsI}} = 0.9$   $\mu\text{s}$  [1]. Consequently the preamplifier used in our setup was configured with a  $\tau_{\text{int}} = 22$   $\mu\text{s}$  in its feedback loop thus adequately satisfying the requirement of  $\tau_{\text{int}} \gg \tau_{\text{CsI}}$ . This and the different routing of the printed circuit are the only differences between the  $\bar{P}$ ANDA version [40] and the design used in the present work.

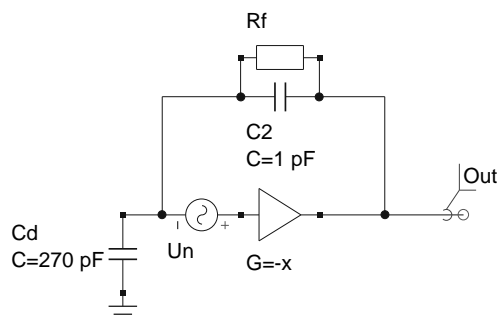


Figure 4.3: A basic integrating amplifier.  $U_n$  represents a thermal noise contribution at its input.  $C_d$  is the input capacitance.

The limit for detecting small signals is imposed by the noise contamination of the signal. When the signals of interest approach the noise level of the readout, they become indistinguishable. Like any detector an APD acts as input capacitance ( $C_d = 270$  pF at gain 50) on the preamplifier. The capacity at the input of an integrating amplifier increases the noise level of the signal significantly. The underlying principle is commonly known as noise-gain. It can easily be understood with the help of a working example. Given an inverting type amplifier as shown in Figure 4.3 the voltage Out is given as

$$\text{Out} = \frac{Z_f}{Z_i} U_n \approx \frac{C_d}{C_2} U_n$$

where  $U_n$  is a tiny noise contribution expressed as voltage. One major source for noise is thermal noise with a typical magnitude of some  $0.8$  mV/ $\sqrt{\text{f}}$ .  $Z_i$  and  $Z_f$  represent the complex impedance of input and feedback respectively. In direct consequence the noise contribution  $U_n$  is amplified by the substantial factor of 270.

As the capacity of the APD cannot be altered it is important to keep  $U_n$  as small as possible. The schematic of the LNP preamplifier can be found in Appendix C Figure C.3. The two key components of the circuit are the low power 300 MHz current-feedback operational amplifier AD8011 and the BF862 junction FET (JFET). The JFET is used as common-emitter amplifier with high forward transadmittance. It acts as low noise voltage amplifier at the non-inverting input

<sup>1</sup>lead tungstate

## 4 Initial situation and equipment

of the AD8011 thus giving it a high input impedance. At the same time it allows for a fast transition frequency and inverts the input. Therefore any given feedback from the operational amplifier output to the JFET is negative. Finally signal integration is achieved via negative feedback. The feedback loop formed by  $C12$  and  $R10$  was set to  $\tau_i = 22 \mu\text{s}$  integration time. By fixing the potential for the inverting current sensitive input of the AD8011 to 5.5 V, the JFET and the operational amplifier together form a fast amplifier with minimal power consumption. During normal operation the whole circuit consumes less than 50 mW.

A detailed description of the circuit can be found in [40].

### 4.4 The $3 \times 3$ crystal matrix

To test the new readout in a realistic environment, two prototype arrays in a  $3 \times 3$  matrix arrangement were built. One such array can be seen in Figure 4.4. Having at least one crystal fully surrounded by other crystals was important to study shower leakage in detail.

The support structure for the matrices had previously been developed and constructed in Bonn. The  $3 \times 3$  matrices had already been used in combination with the photodiode readout at the Studentenexperiment (see Section 2.5) and for prototype tests (see [51]). In the present case the photodiode readout was replaced with the Hamamatsu S8664-1010 Si APD (compare with Section 4.1). It was combined with the LNP preamplifier mentioned earlier (see Section 4.3).

### 4.5 The high voltage power supply

The strong gain dependence of the avalanche photodiodes on the bias voltage imposes strict requirements on the stability of the high voltage power supply (see Section 3.2). Furthermore the HV power supply has to be floating to avoid ground loops and prevent noise from coupling into the sensitive readout circuit via its ground connection. To accommodate for this special requirements two Iseg<sup>2</sup> EDS F 025n 104-K modules were purchased. The HV modules are of standard 6U Eurocard format and fit into the Iseg ECH 228 crate.

The modules have a maximum output current of  $100 \mu\text{A}$  and a voltage range from 0 to -2500 V. Ripple and noise in the frequency range  $10 \text{ Hz} < f < 100 \text{ MHz}$  is guaranteed to be less than 10 mV for maximum load conditions. The module can be controlled via CANbus. Voltages can be adjusted for the individual channels with a resolution better than 50 mV. However, the voltage measurement is guaranteed to be better than 5 mV. Additionally the current measurement is better than 2 nA [26]. The precise measurement of the current is very useful to see if the bias voltage of an APD had already exceeded its breakthrough voltage. Although the current through the APD is limited by a  $28 \text{ M}\Omega$  resistance (see Figure C.3) the current rises to the order of several  $\mu\text{A}$  in that case.

<sup>2</sup>Iseg Spezialelektronik GmbH, Bautzner Landstr. 23, 01454 Rossendorf, Germany.



Figure 4.4: A  $3 \times 3$  matrix in the beam line seen downstream from behind the MiniTAPS detector. In this particular measurement the upper left crystal was aligned centrally in the beam.

## 4.6 The i-trOnics SADC

The i-trOnics i-SADC 108032 was the FADC that was used in this work. The FADC was readily available and the sources of the firmware were accessible. These were the main reasons why it was used as a testbed for the readout studies conducted during this thesis.

The module was developed by Igor Konorov and Alexander Mann at the Technical University of Munich<sup>3</sup>. It has 32 channels of  $110\ \Omega$  differential inputs with individual virtual ground, all featuring a 10 bit ADC resolution. The device comes as a standard 6 U VME module, but only uses the VME crate as power supply. All communication is either established via a dedicated optical fiber connection to a special concentrator module or via a special J2 adapter card that can be read out via an USB interface. The latter solution was used in the present setup. It is possible to operate the SADC in 40 MHz or 80 MHz mode which can be controlled by replacing the firmware on board via the JTAG<sup>4</sup> interface[43]. For the APD readout the 80 MHz solution was used.

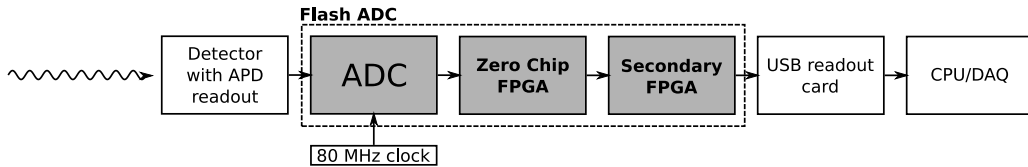


Figure 4.5: Schematic dataflow of the TU Munich SADC.

The board is divided into two identical operational units of 16 ADC channels each. A schematic view of the data flow of one channel is outlined in Figure 4.5. The 16 channels are operated in parallel with the primary clock frequency and the resulting data stream is fed in a parallel fashion into one of two Zero Chip FPGAs. Here the data is processed by a configurable firmware that can be loaded into the chip. The Zero Chips (each responsible for 16 channels) communicate with a single secondary FPGA that is loaded with its own firmware during power up. The secondary FPGA manages the communication with the fiber optical uplink to the concentrator module or if programmed with a different firmware, as in the present case, with the J2 USB readout card. It also manages the programming of the two Zero Chip FPGAs and offers a register based configuration interface for the Zero Chip firmware via a dedicated I<sup>2</sup>C bus. For all tests that have been conducted using the SADC module the USB readout firmware was used on this chip.

<sup>3</sup>Physik-Department E18, Technische Universität, München, James-Franck-Strasse, 85748 Garching.

<sup>4</sup>JTAG is the commonly used name for the IEEE 1149.1 standard *Standard Test Access Port and Boundary-Scan Architecture* for test access ports used on printed circuit boards.

### 4.6.1 The Zero Chip firmware

The SADC was operated using the Window Trigger v3.00 firmware or its derivatives (see Section 6.1.2). The firmware was developed by Alexander Mann and Igor Konorov for this SADC. It supports three different triggering modes (latch-all, sparse and self-trigger) and has configurable thresholds for all input channels. It has an in-built support for external trigger signals and other fully configurable features, such as input signal inversion and maximum extraction.

In case of the USB readout the 80 MHz clock is provided by an on-board quartz. In all in-experiment situations a single clock is distributed via the Gigabit ethernet transceiver. The readout is event based and comprises the baseline, the signal's maximum, a 30 bit clock value and additional time correction information of the integrated constant-fraction discriminator.

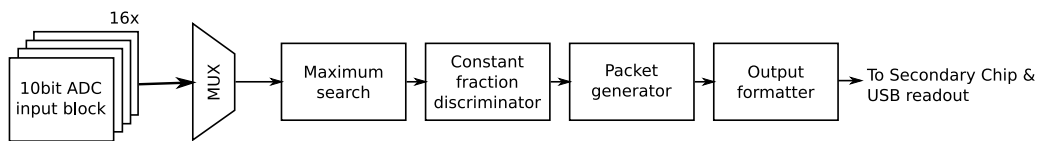


Figure 4.6: Schematic of the Zero Chip dataflow. The data of the different input blocks is multiplexed (MUX) and injected it into the pipeline.

To use the available resources on the FPGA sparingly the main data processing on the chip is done in a pipeline. The principle of operation is outlined in Figure 4.6. The 16 input blocks are responsible for acquiring the number of samples specified by the `event size` setting, in case an internal trigger condition is raised. This trigger can either be generated from each input-block itself or be distributed from input block number 0 in *latch-all* or *sparse* trigger mode. The samples are stored in integrated FIFOs<sup>5</sup>, that are implemented with the internal block memory of the FPGA. The multiplexer (MUX) continuously switches between the different input channels and checks if new data is present at one of the channels. If data is waiting, the samples are read from the input block FIFO and injected into the pipeline that is operated at primary clock frequency. The different pipeline stages can now add data words to the primary sampling data that are also moving along the pipeline. By marking them with additional tag-bits they can be distinguished from sampling words. In a first step the maximum is extracted from the data stream. It is needed by the constant fraction discriminator stage. The constant fraction discriminator uses this information and finds the two samples next to the adjusted fraction. It then interpolates between the neighboring samples, thus minimizing time quantization noise for signals with fast risetimes. The packet generator and the output formatter prepare the data for serial transmission to the Secondary Chip FPGA, from where it is finally sent to the USB output or the fiber up-link respectively.

<sup>5</sup>A FIFO is one type of basic buffer typically used in computer science. It obeys the paradigm of first-in-first-out data management.

#### *4 Initial situation and equipment*

## 5 The trigger branch

This chapter focuses on how a valid trigger signal can be obtained using an APD based readout. First the theoretical background of signal shaping is discussed, then needed electronics developments are described. Finally the results of different time resolution measurements are presented.

### 5.1 Goals and challenges

The first level trigger decision of the Crystal Barrel experiment is made in some 20 ns after all relevant subdetectors have reported to the logic. This process is timed to happen 225 ns after the event (see Section 2.4 for details). Although a new energy readout is planned and the current trigger scheme will have to be streamlined for the upgrade, 200 ns were taken as latency constraint for the new trigger signal. Given that it takes the CsI(Tl) signal approximately 100 ns to rise to its maximum, this limit seems reasonably achievable.

To avoid false coincidences from the crystals, boundary conditions for time resolution and noise level were chosen. The initial aim was to achieve time resolutions in the order of 10 ns ( $\sigma$ ). This number is strongly dependent on the actual noise level. That means that one can afford a much worse time resolution, given that there is almost no chance of false coincidences. On the other hand one needs a very fine time resolution if the readout is noisy, to compensate for the higher probability of accidental coincidences [3]. This point strongly depends on the actual implementation of the new trigger scheme being deployed. It will inevitably lead to further discussion.

Finally it is important to conduct the energy calibration of the APD readout in the primary tagged photon beam. Therefore a single crystal should be able to sustain a minimum trigger rate of a few kHz.

The fundamental requirements for a new trigger for the main calorimeter can be summarized as follows. First a low latency is needed to avoid unnecessary delay and the associated distortion of analog information in long delay lines. Second a high time resolution and stability are needed to actually allow the on-line selection of coincident events. Finally the new trigger should allow for high rates in the order of a few kHz. Although multi-hits in a single crystal are not very likely [13] they can occur occasionally as described by Poisson statistics. To also account for such rare events and have at the same time the opportunity to test the equipment in a primary photon beam, rate stability up to several kHz is necessary.

## 5.2 The preamplifier signal

Given a light pulse from a CsI(Tl) crystal the preamplifier will accumulate a charge which is approximately proportional to the photon flux captured by the APD. An integrating type preamplifier will eventually convert the collected charge into a voltage at its output. Figure 5.1 shows the form of a simplified CsI(Tl) pulse shape and its integrated output as it would be expected from an ideal integrating amplifier that integrates over an infinitely large time window ( $\tau = \infty$ ). Such an amplifier would be impractical for a real world scenario. The amplifier would start to pile-up<sup>1</sup> the signals of several events and soon reach its limits where no further increase in signal is possible. Therefore the amplifier has to return to its baseline which is usually achieved by an exponential decay of the signal. This can be seen in Figure 5.1. However it is important to note that all useful information in the underlying signal is contained in the leading edge and the maximum of the preamplifier output. The decay of the preamplifier signal is always the same exponential shape and the decay constant  $\tau$  is a fixed property of the preamplifier itself (for more details see Section 4.3). The only case where the tail of a signal contains additional information is in the occurrence of pile-up. It is essential to account for such events otherwise one will overestimate the size of this pulse and miss the second event. This phenomenon and how it is taken care of for the energy readout will be discussed in more detail later.

Figure 5.1 shows the typical response of an integrating amplifier like it was used for the prototype APD readout of a CsI(Tl) crystal. It illustrates the general time scales that are involved. The signal rises over roughly  $5 \mu\text{s}$  and then decays slowly. The decay is an exponential with a time constant of  $22 \mu\text{s}$ . A direct consequence is that the signal does not comply with the input requirements for many commercial standard discriminators. Most discriminators with single ended inputs have serial capacitors at their input to protect the input from DC currents. The capacitor acts as a CR high pass stage. In the case of a slowly varying signal, like the preamplifier signal, most of the spectral power is lost at the input of the discriminator. To overcome this problem pulse shaping was introduced to the readout and the generation of a trigger signal.

## 5.3 Background theory on pulse shaping

The term *pulse shaping* usually refers to applying signal filters to an analog signal and thereby selecting particular frequency ranges for enhancement while others are chosen to be suppressed. Generally pulse shaping aims to increase the signal to noise ratio. Thus it improves the overall quality of the readout. Another reason for applying pulse shaping is to manipulate the risetime of a signal.

In the present scenario the latter application of pulse shaping is used to derive a

---

<sup>1</sup>During the duration of a detected signal, a second signal falling in the same time window will *pile-up* on the first [29].

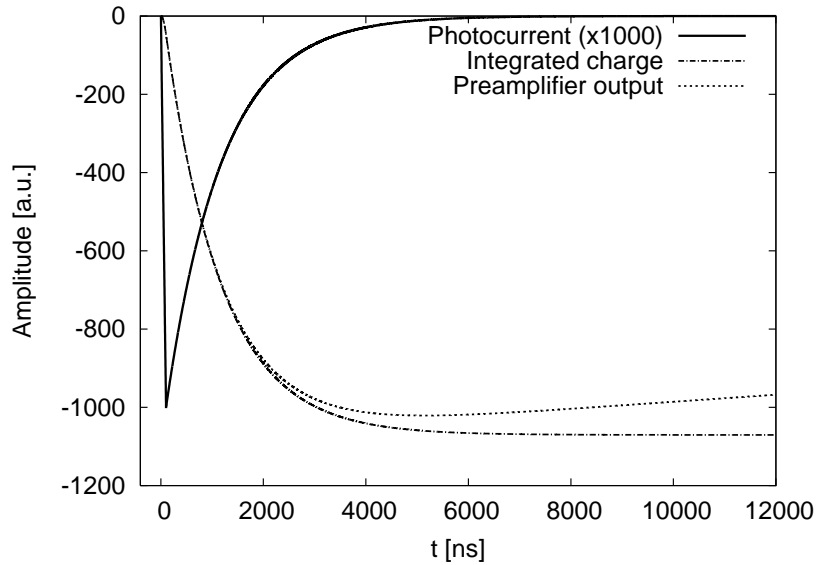


Figure 5.1: Schematic calculation of preamplifier output in comparison with initial photocurrent. The flux was approximated with a linear rise of 100 ns duration and an exponential decay with decay constant  $\tau = 1.1 \mu\text{s}$ . The preamplifier gain in the simulation was equal to one.

signal from the preamplifier output that rises faster than the preamplifier output itself. The derived signal has to comply with the latency constraint of the trigger logic (see Section 5.1) as a primary design goal. However, the derived signal has several additional advantages over the bare preamplifier output. First of all a quickly rising signal is more likely to exhibit better time resolutions than a slowly rising one. Several mechanisms contribute to this behavior. One example which is particularly easy to understand in the time domain is illustrated in Figure 5.2. However, the main problem arises from low frequency noise components. A typical noise spectrum often follows a  $1/f$  behavior to first order. In the time domain it is clear that a slow signal, that obviously has its main spectral power in the lower frequency range, is more strongly affected by noise than a fast rising signal.

The LNP preamplifier output is incompatible with the initial demand for a low latency signal due to its long risetime. Initial tests with leading edge discriminators operating at very low thresholds showed that it was not possible to generate a low latency trigger signal with  $\sigma < 10$  ns time resolution.

The well established approach to deriving signals that achieve nanosecond time resolutions is shown in Figure 5.3. The new piece of electronics that has been inserted into the readout chain is called a fast timing filter amplifier. It turns out that this device solves the above issues. A timing filter amplifier essentially consists of a frequency filter and a timing amplifier. Timing amplifiers achieve rise times in the subnanosecond regime usually by sacrificing temperature stability

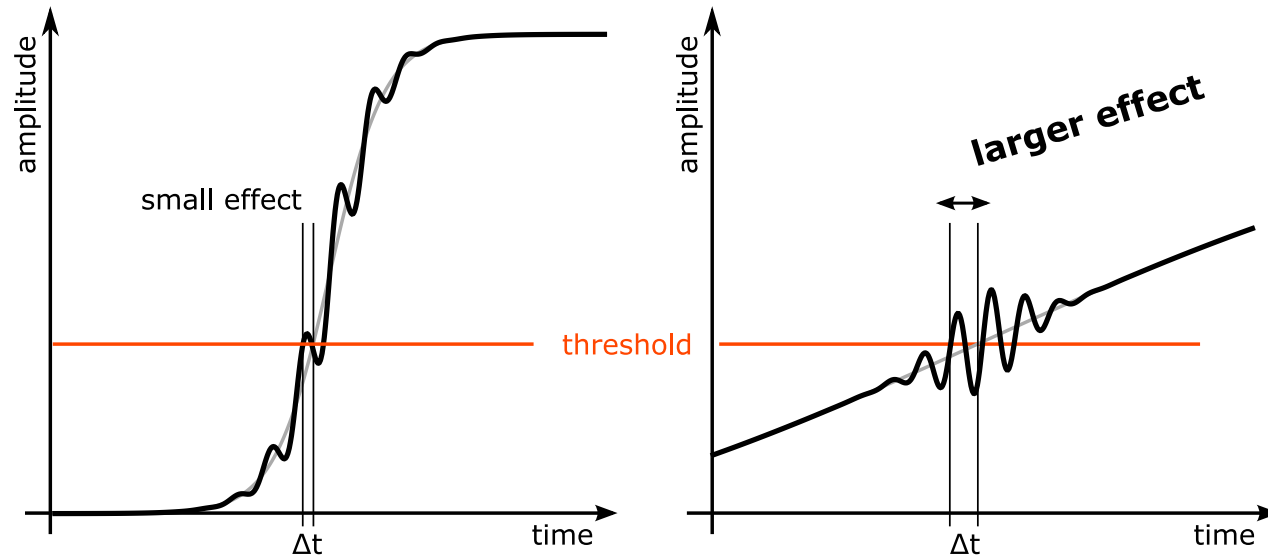


Figure 5.2: A slow timing signal in combination with a leading edge discriminator is more sensitive to noise. The left hand side shows the function  $\tanh(x)$  with a sinusoidal noise contamination added to the signal. The right hand side shows the same signal by a factor of 10 slower. Yet it exhibits the same noise feature. The time measurement on the faster signal will in general yield better time resolution for a leading edge discriminator.

and linearity [39]. The latter effect makes this readout chain not well suited for energy readout. It is solely optimized for time resolution. Section 5.8 will be dedicated to finding a solution for the energy readout part.

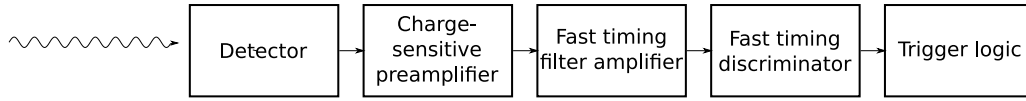


Figure 5.3: Common scheme for time readout achieving nanosecond resolutions.

During all following tests the timing filter amplifier was implemented as a Bessel band-pass filter. That means it can be characterized with the transmission frequency  $f_t$ . The output signal therefore loses its low and high frequency components as they get attenuated exponentially. It only preserves its spectral power in a frequency band around  $f_t$ . The response of the filter to the step function<sup>2</sup> is called the step response. This output has the rise time  $\tau$  that is closely related to  $f_t$ . The relation is given by

$$\tau = \frac{1}{2\pi f_t}$$

where  $\tau$  is usually called the shaping time constant. With respect to the 200 ns latency constraint a  $f_t$  of 6 MHz was chosen. That corresponds to  $\tau = 26.5$  ns. As the sole filtering removes spectral power the signal is strongly attenuated. The timing amplifier is used to amplify the remaining frequency components.

## 5.4 Timing filter developments

In the course of the project different filters were tested in combination with the preamplifier signal of the APD readout. It was natural to start with equipment that was already at hand. At first the usability of the shaper of the current photodiode readout was evaluated. It was found that the filter had timing constants that were not suitable for the planned application. All recorded time spectra were nearly flat over a range of several hundred nanoseconds. In a second step the commercial module MSCF-16 by the company Mesytec [34] was tested, but also this shaper did not fulfill the signal requirements for the trigger signal.

First meaningful results were obtained with the Ortec 474 spectroscopy shaper (see Section 5.4.3). The results obtained from this single channel NIM module lead to the development of further optimized custom design filters that are described in Sections 5.4.4 and 5.4.4. These filters were designed to also satisfy the requirements for small-scale integration and to account for tests that required larger numbers of channels.

The work on the topic was mainly done in collaboration with M. Steinacher at the University of Basel. I received further support from Herbert Löhner from

<sup>2</sup>Step functions can easily be realized in hardware as square functions with low frequencies.

KVI, Groningen and his group, who supplied a printed circuit board layout that could be adopted to the present needs.

### 5.4.1 Experimental method

To allow the comparison of different timing filters, the common setup as outlined in Figure 5.4 was used. All timing tests in this section have been performed with an external coincidence of organic scintillators read out by photomultiplier tubes. A single CsI(Tl) crystal in combination with the APD readout served as a testbed for the timing filters. The LNP preamplifier was operated with negative polarity output. It was directly connected to the timing filter under test. To minimize noise pick-up in the setup, a complete Faraday shielding was assured and ground loops were avoided. A complete description of the necessary steps is given in Appendix A.

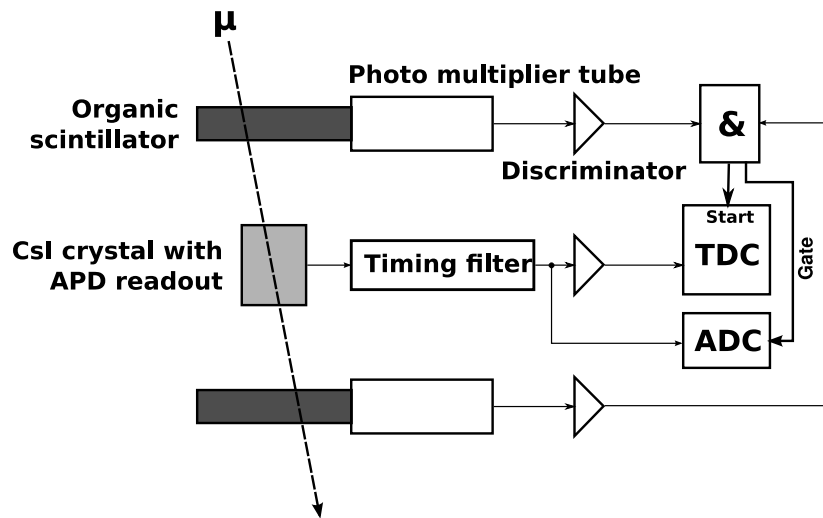


Figure 5.4: Common test setup for time resolution measurements with cosmic muons. The outer organic scintillator coincidence serves as a time reference.

The external coincidence had a typical time resolution in the order of nanoseconds, which was sufficiently high for this study. In addition to the time readout via the time digital converter (TDC), a small fraction (1:30) of the signal was fed to an ADC. This was done to check whether or not a Landau distribution could be observed. The ADC data was also used to verify the proper settings of the trigger thresholds and to allow time-walk correction.

### 5.4.2 Time-walk correction

Standard leading edge discriminators are prone to the mechanism of *time-walk*. The phenomenon describes the systematic time shift of a signal in dependence of

its pulse height. Time-walk correction compensates for this effect by exploiting the knowledge of this relation. To apply time-walk correction, some measurement of pulse height or signal strength has to be present.

The time-walk correction in this work is achieved by plotting time versus the ADC value. The empiric function

$$\Delta t(x) = \frac{\alpha}{\sqrt{\beta + x}}$$

is then fitted to the resulting distribution (see Figure 5.5 for an example). Here  $\alpha$  and  $\beta$  are the fit parameters and  $x$  is the corresponding ADC value. The function values of  $\Delta t(x)$  can now readily be subtracted from any given event-time value and will substantially minimize pulse height dependent time-walk.

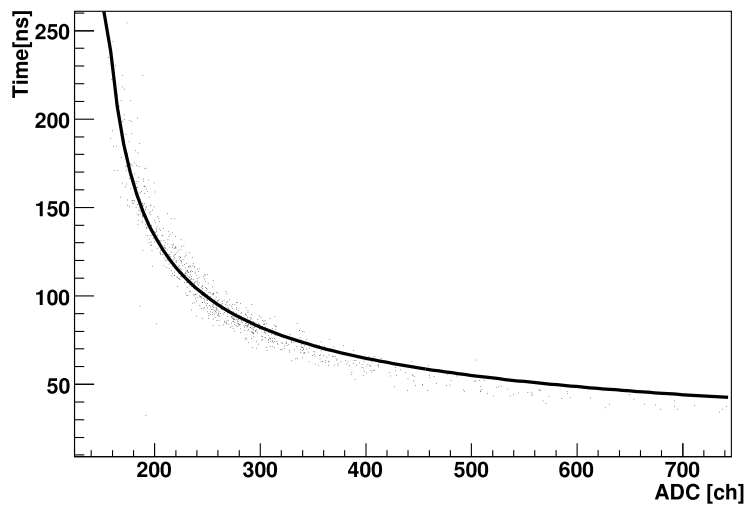
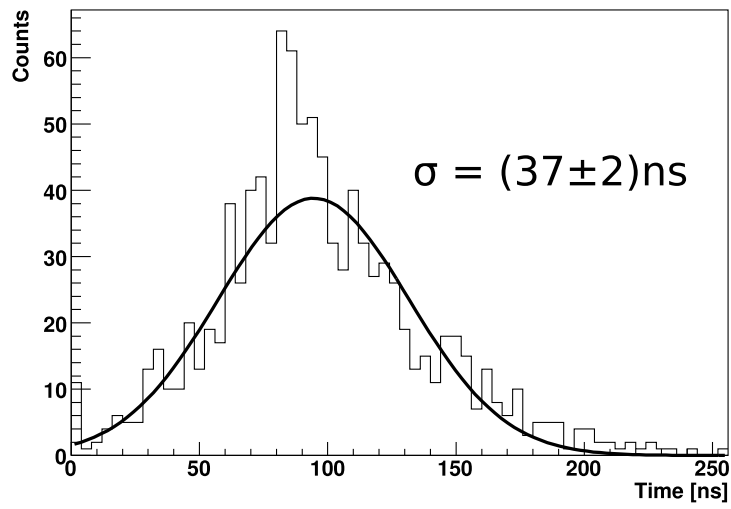


Figure 5.5: Typical plot for performing a time-walk correction. In this example cosmic muons were measured with the prototype APD readout in combination with the Ortec 474 timing amplifier (see Section 5.4.3).

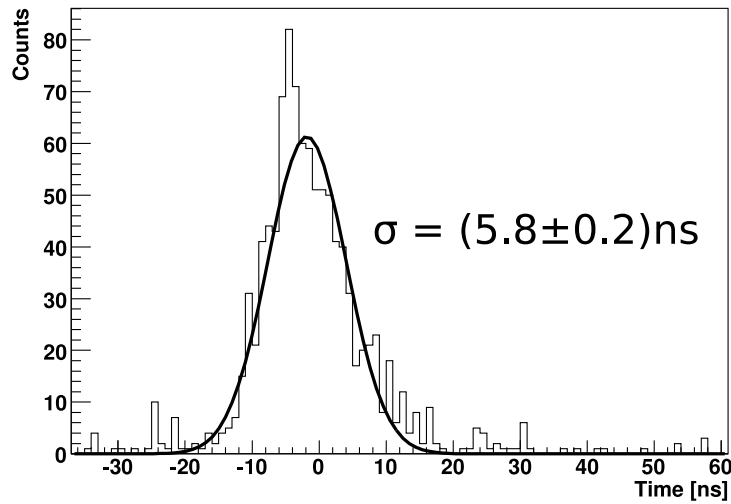
### 5.4.3 The Ortec 474 Timing Amplifier

Further timing tests have been performed with the Ortec 474 Timing Amplifier. The Ortec 474 is a timing filter amplifier. It is a standard NIM module for one input channel that has been specially designed for pulse shaping aiming at optimizing the signal to noise ratio for timing applications. It features continuously changeable gain in combination with individually adjustable CR and RC time constants covering a range from 20 ns to 500 ns each.

The measurements with the Ortec 474 were the first tests that showed time resolutions close to the initial design goal. The results of the measurement are



(a) Raw time spectrum



(b) Corrected time spectrum

Figure 5.6: Results of the time resolution measurement with the Ortec 474. The integrating and differentiating time constants were set to  $\tau_i = \tau_d = 50 \text{ ns}$ . For the corresponding time-walk correction function see Figure 5.5. These results already illustrate that on-line time-walk correction is needed for the trigger if time resolutions better than 10 ns ( $\sigma$ ) are to be obtained.

outlined in Figure 5.6. A time resolution ( $\sigma$ ) of  $37 \pm 2$  ns was measured with cosmic muons (Figure 5.6(a)). This measurement already showed that time-walk correction is indispensable. By applying time-walk correction to the data, a resolution of  $5.8 \pm 0.2$  ns was achieved (Figure 5.6(b)).

Nevertheless being only a single channel module, the Ortec 474 was not a suitable solution for the demands of the trigger tests. Only one such module was available during the tests and more than one channel was needed for the Studentenexperiment. The readout of two  $3 \times 3$  arrays meant that 18 channels were needed. The next section will give further reasons, why a different solution had to be found.

### 5.4.4 Integrated timing filters

As was seen in simulations performed by M. Steinacher in Basel and confirmed in first measurements utilizing the Ortec 474 timing filter, the optimal transmission frequency  $f_t$  is close to 6 MHz. Since the fast Fourier components of the preamplifier output are small, even minute disturbances on the signal are sufficient to degrade the time resolution. It is therefore desirable to have the timing filter as close as possible to the preamplifier, thus avoiding long signal paths that are prone to noise-pickup. The timing filter amplifier therefore needs to be small enough to allow integration into the crystal end-cap. It should furthermore feature low power consumption to minimize the thermal power constantly heating the detector system during operation. This aim is easy to justify when considering that the whole system has to be temperature stabilized.

As a result of these additional design goals, a small low-power integrated timing filter was required and developed at the University of Basel. This timing filter will be called *Basel Shaper* throughout this document. At the same time it was crucial to test the idea of running a functioning trigger with such timing filters as soon as possible. As the development of the Basel Shaper prototype took time and certain deadlines had to be met, a second timing filter was developed in Bonn, where size and power consumption were secondary design goals. This line of development will consequently be called *Shaper rev. 4.2* in this work.

#### Basel Shaper

This timing filter was designed by M. Steinacher at the University of Basel. It was outlined as a low power circuit with a small footprint on the printed circuit board. Such requirements were important for integration into the crystal end-cap. The circuit was based on the low-power dual operational amplifier AD8012 [2].

The filter is a combination of an active first order high-pass (HP) filter ( $\tau_d = 26.4$  ns) with a 6 MHz second order Bessel low-pass (LP) in Sallen-Key [49] configuration.

The initial revision of this prototype was sent to Bonn for timing measurements (see Figure 5.7). It featured a signal peaking time of 230 ns [45]. The initial version



Figure 5.7: The Basel Shaper prototype during time resolution tests in Bonn.

was still an inverting type with positive internal feedback. Initially the idea here was to produce negative polarity output pulses that were required by all of our in-stock discriminators. However, due to the fact that in the meantime it was decided to run the preamplifier itself with negative polarity output during the tests this feature was now unwanted (see Section A.1). To still be able to run first time resolution measurements the output was inverted with the help of a LeCroy linear fan-in/fan-out LRS 428F. The effect of this inversion was tested and turned out to be small compared to the overall time resolution of the signal.

#### Shaper revision 4.2

This shaper is the combination of a passive first order Bessel HP and LP with two active amplification stages. It is derived from the second order filter design developed at the KVI [17]. In the case of the original, lead tungstate (PbWO) is used as a scintillator and different timing constants are required for the CsI(Tl) crystals. Following the Basel prototype, the KVI circuit was modified, such that it was possible to operate it at  $f_t = 6$  MHz. A single printed circuit board supports two timing filter channels (see Figure 5.8). The component placement for the rev. 4.2 is outlined in Appendix C, Figures C.1 and C.2.

For comparison measurements with higher energy resolutions further models of this shaper have been manufactured with lower transmission frequencies  $f_t$ . The first such model was indexed as revision 4.2e. Further alterations were labelled successively 4.2f and g. A detailed discussion of the motivation and outcome of this measurement will be given in Section 5.6.

The underlying filter and amplifier stages are outlined in Figure 5.9. Amplification was achieved by two negative feedback AD8099 operational amplifiers ( $X1$  and  $X2$ ) operated at a closed loop gain of  $G = 9$ . The input was realized as an CR high-pass filter formed by  $C_1$  and  $R_1$ . At this point the signal is amplified the first time and then passes the integrator stage ( $R_2$  and  $C_2$ ). It is then amplified again before reaching the output.

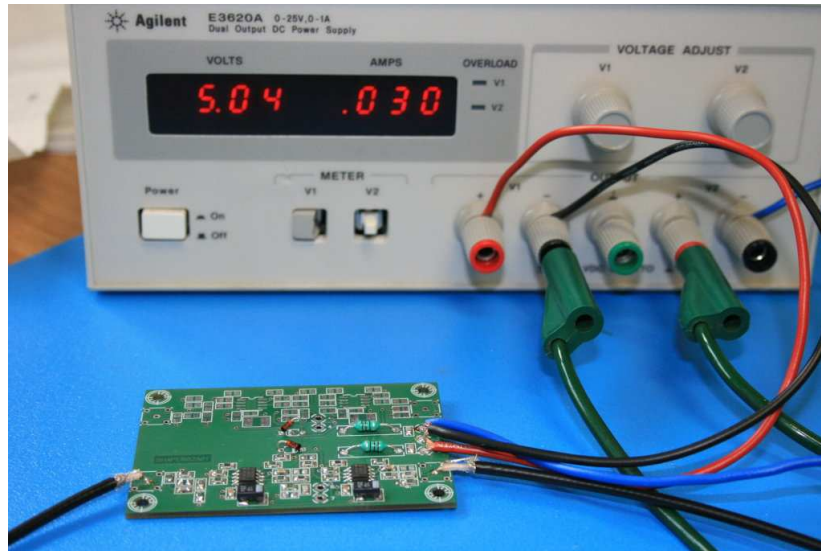


Figure 5.8: The modified KVI shaper. Although the PCB supports two channels, only one is implemented on the picture. Being not optimized for power consumption, the circuit uses 30 mA on the +5 V side of the power supply in contrast to the 4 mA of the Basel Shaper [45].

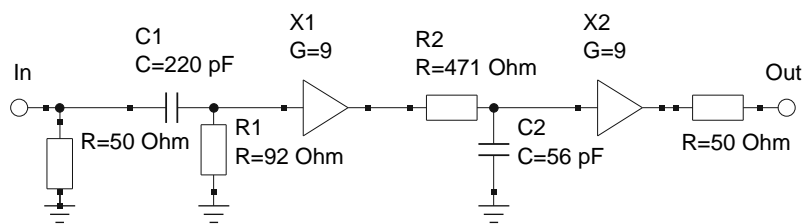


Figure 5.9: Overview of the main components of Shaper rev. 4.2.

## 5 The trigger branch

Due to a calculation error, the timing filter was accidentally equipped with a differential time constant  $\tau_d = C_1 R_1 \approx 20$  ns and a RC-integrator time constant  $\tau_i = R_2 C_1 \approx 26$  ns. The original intention was to satisfy  $\tau_d = \tau_i \approx 26$  ns. Choosing  $\tau_d$  smaller results in a higher cutoff frequency for the input high pass, which again prevents the signal from being overly attenuated, because it widens the spectral transmission band of the whole filter. It turned out this is an advantage at low particle energies, because less spectral power is removed from the signal. This point will be discussed in more detail in the following sections.

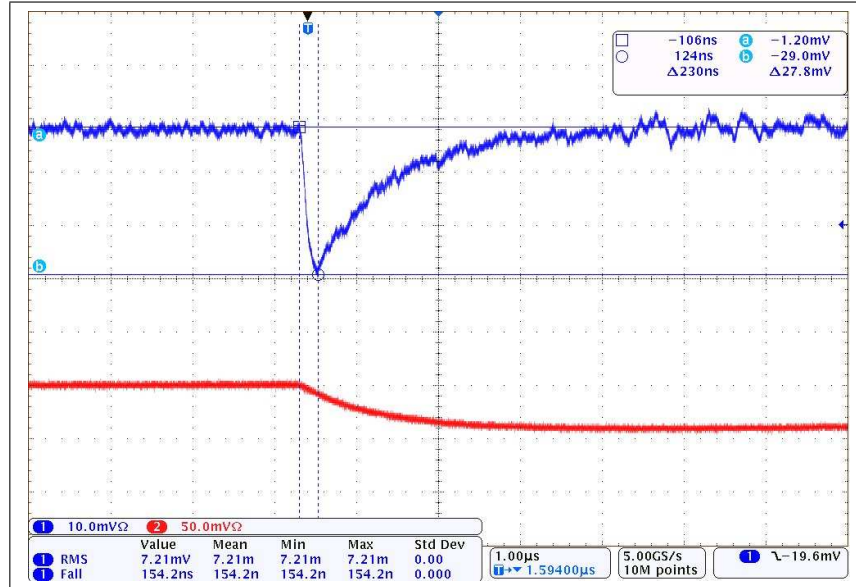


Figure 5.10: Signal response of Shaper revision 4.2 (top) seen with its input from the preamplifier (bottom). The cursors mark the  $\Delta t$  of 230 ns. The peaking time of the signal response is in good agreement with the response of the Basel Shaper.

## 5.5 Timing filter tests with cosmic muons

Having discovered that a custom designed timing filter could in principle supply a signal that meets the design goals and furthermore made small enough to fit into the end-cap of the crystal, a set of tests was devised to probe its time resolution. A first step was to justify the use of the Shaper rev. 4.2 instead of the Basel version. This was important to estimate the significance of the results that were to be obtained. The consequence was a comparative study of the two integrated versions that were introduced in the last section.

The comparison was done with cosmic muons. Measurements of the three prototypes that existed at this point in time were carried out in parallel. As this was the only difference from the method used in Section 5.4.1, a repetition of the

## 5.6 Timing filter tests with the tagged photon beam

experimental method is omitted at this point.

The APD bias voltages for a gain of  $G = 50$  were only known approximately. Therefore the voltages were chosen such that the crystals would respond to cosmic muons on average with the same gain. To check if that procedure of gain-matching would introduce systematic errors into the measurement, all measurements were repeated with swapped configurations of crystal and shapers. From that cross-check it was learned that indeed the results of the different timing filters could be compared in this context. All the results were consistent and the time resolution can, within the statistical uncertainties, solely be attributed to the different timing filters. After such preliminary crosschecks, the setup was left running for a week and a total of 11 k coincident events was recorded.

The time distributions that were recorded are plotted in Figure 5.11. Each histogram was fitted with a Gaussian shape. The width ( $\sigma$ ) of each distribution was extracted. It was observed that Shaper revision 4.2 performs slightly better in terms of time resolution than the Basel model. Whereas revision 4.2e equipped with the longer shaping time constant exhibits the same time resolution as the Basel model.

To make sure that the additional inversion process of the Basel Shaper signal did not have a strong effect on the time resolution, it was checked whether or not inverting the signal three times instead of just once did degrade the time resolution. No noticeable difference was found within the uncertainty limits.

The better performance of the Bonn model can most likely be attributed to the fact that the Basel model is a low power version. Using such components to satisfy power constraints generally has a tradeoff. In this case it is very likely that the low power operational amplifier tends to add distortion, that leads to a worse time resolution.

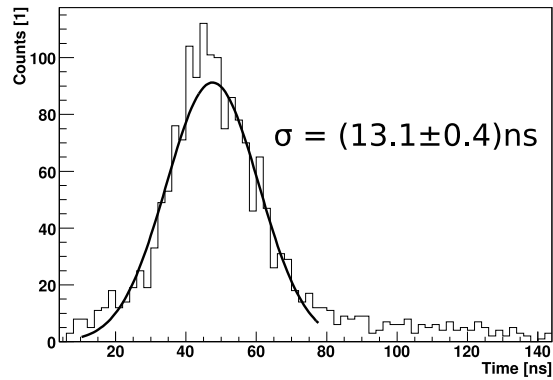
Ultimately these preliminary tests showed that it was possible to produce results with the modified KVI shaper that were similar to what was measured with the Basel prototype. Although rev. 4.2e represented a timing filter with very similar time resolution, it does not comply with the 200 ns latency constraint. With this information at hand all further studies were conducted using the revision 4.2 shaper unless stated otherwise. The results then also have predictive power for the final version of the Basel Shaper.

## 5.6 Timing filter tests with the tagged photon beam

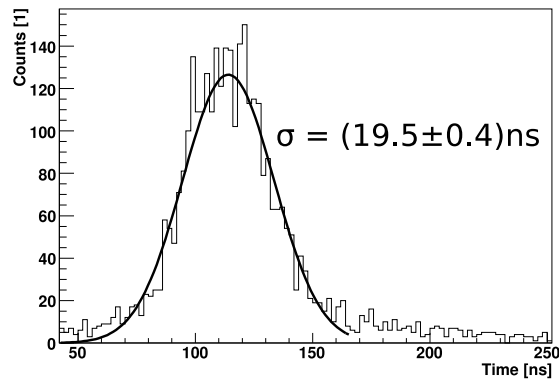
As a next step of the analysis it was particularly important to determine whether or not it was possible to generate a coincident trigger signal from the Crystal Barrel crystals with the prototype APD readout and such a timing filter. For this study 18 rev. 4.2 shapers were built to support two  $3 \times 3$  CsI(Tl) arrays with APD readout. The tests were performed as part of the Studentenexperiment (see Section 2.5).

In this section the trigger of the experiment is described and its performance is

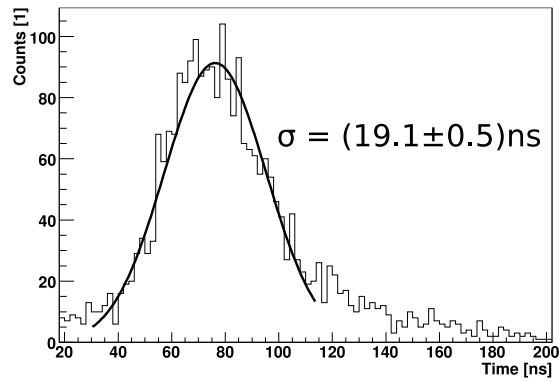
5 The trigger branch



(a) Revision 4.2,  $\tau_d = 20 \text{ ns}$ ,  $\tau_i = 26 \text{ ns}$



(b) Revision 4.2e,  $\tau_d = \tau_i = 100 \text{ ns}$



(c) The Basel Shaper

Figure 5.11: Time resolution measurement with cosmic muons for three different timing filters. No time-walk correction was applied.

discussed briefly. Second a summary of the additional time and energy resolution-tests with different shapers is given. The latter is important with regards to the possibility of a combined energy and time readout with a single shaper.

### 5.6.1 Experimental method

The hardware tests that were performed in the context of the Studentenexperiment exploited several features of the tagged photon beam which is also used for the Crystal Barrel experiment (see Section 2.1). Comparing these tests with cosmic muon measurements, the main differences are the higher energies, the higher rates and most importantly the tagged photons. The latter means that photons arriving at the experiment, generally have a known time of arrival and a well defined energy (see Section 2.1.3 for details). This feature allows time and energy resolution measurements to be conducted at the same time.

The setup was positioned on the beam line, between the MiniTAPS detector and the gamma intensity monitor. The MiniTAPS was moved towards the setup of the Studentenexperiment thus providing a good shielding for electromagnetic background (see Section 2.3.5).

The Studentenexperiment used very similar readout electronics to the Crystal Barrel experiment. Equipped with its own Sync-Client<sup>3</sup> it was possible to transparently integrate the experiment into the Crystal Barrel data acquisition system (DAQ). This was done to take advantage of the full readout of the tagging system.

The trigger signal of the Studentenexperiment entered the main DAQ system as the *Innenself* trigger signal<sup>4</sup>. Therefore only one connection had to be exchanged, while the the main experiment was left almost completely unaffected. To ensure that timing would always be governed by the tagging system with its intrinsically high time resolution, 50 ns of delay cable had to be removed from the tagger trigger signal. Doing so assured that the signals stayed inside the valid time range of the TDC and possible gate of the ADCs.

The primary electron energy of ELSA was tuned to 1.2 GeV for this experiment. The corresponding  $E_\gamma$  covered by the tagging hodoscope was ranging from 200 MeV to 1.2 GeV. Each photon that could trigger the readout had a defined energy known to a precision of at least  $\Delta E_\gamma \leq 25$  MeV.

There were two days of beamtime available for the experiment. Their use can be divided into two main parts. First of all the  $3 \times 3$  crystal arrays were calibrated by putting them directly into the primary photon beam. In this calibration process each crystal was once aligned, such that the photon beam would hit it centrally (compare Figure 5.12). This was done to check for linearity and to estimate the gain coefficients of the APDs. During this time different shapers were tested for a single crystal. The main aim of this measurement was the in-beam calibration,

---

<sup>3</sup>The Crystal Barrel experiment uses a gated mode data acquisition system, where the event synchronization is guaranteed by specially designed VME modules called Sync Clients.

<sup>4</sup>*Innenself* is the name of the self-trigger condition of the inner detector.

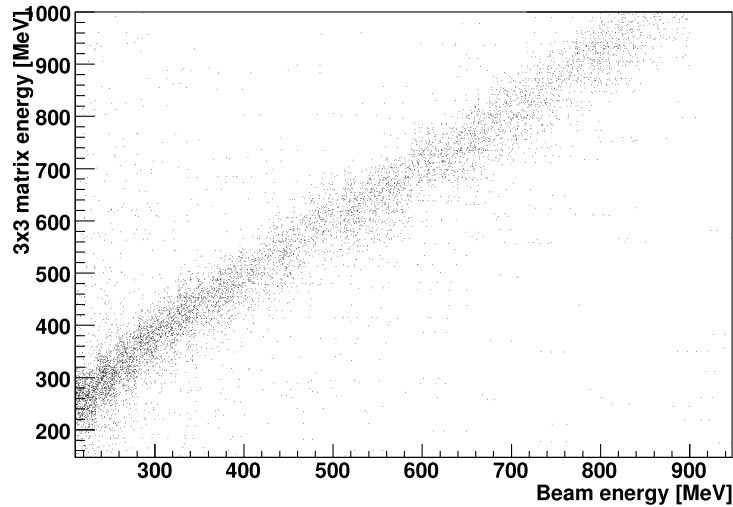


Figure 5.12: Accumulated energy detected by a  $3 \times 3$  matrix for photon hits in the central crystal versus the beam photon energy. The assumption of an underlying linear dependence to first order seems justified. The line exhibits a substantial width. It reflects the limited energy resolution of the timing optimized readout.

the test of rate stability and to show the feasibility of a low latency first level trigger.

The second part was the actual measurement. For that purpose the two blocks were moved in measurement position and the trigger was generated by coincidence to detect the symmetric  $\pi^0$  decay. Most of the two days of beam time was spent on data taking in that mode. This was to accumulate enough data to yield sufficient statistical significance in the analysis. In this thesis only the outcome concerning the performance of the readout will be discussed rather than the reconstruction and analysis of the full experiment. The most important results for this thesis work were obtained during the calibration period at the very beginning of the beam time.

## 5.6.2 Results and discussion

### Trigger performance

As was already outlined in Section 2.5, the Studentenexperiment aims at measuring the symmetric decay of the  $\pi^0$  from the decay of the  $\Delta(1232)$ . With the two  $3 \times 3$  detector arrays at hand the trigger condition of choice was straight forward. A coincidence of the two blocks was the only requirement. The trigger scheme that was used is outlined in Figure 5.13.

The decision whether one block had fired or not was derived from an analog or

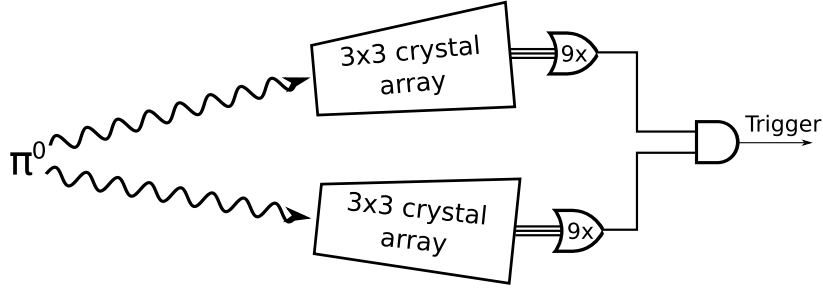


Figure 5.13: Schematic of the trigger condition as it was implemented for the Studentenexperiment. The only condition is that the two photons from the symmetric decay of the pions are detected at the same time.

for the nine crystals of each block. Here the requirement was, that at least one crystal per block was above threshold. The single crystal thresholds were kept at a point close to the minimum allowed by the discriminator (LeCroy LRS4413), resulting in reasonable cosmic muon rates in the order of 10 to 20 Hz in each array. For the direct in-beam measurement it was only possible to position one block in the photon beam at a time. In that case the coincidence was simply changed to a logic or thus avoiding complicated and long lasting rearrangements of the setup during the calibration.

The setup was equipped with leading edge discriminators. Therefore a time resolution in the order of  $\sigma = 20$  ns had to be expected, which corresponds to the results for the uncorrected time resolution from Section 5.5. The discriminators had an output pulse width of 100 ns each corresponding to a 50 ns coincidence gate ( $2.5\sigma$ ). No time-walk correction was used on trigger level in this experiment.

The trigger described here turned out to be very selective for the reaction of interest. During the measurement rates of  $\sim 20$  and  $\sim 60$  Hz (the latter was measured for the  $3 \times 3$  matrix positioned closest to the beam line) were observed. However, the coincidence rate was very stable at approximately 0.5 Hz. This number was also expected as a rough first estimate [41]. Although the readout electronics used during the experiment were optimized for timing, in this experiment also the energy readout was conducted via this readout branch for simplicity reasons. A preliminary calibration from the in-beam measurement that was conducted during the beam time led to the spectrum shown in Figure 5.14. The  $\pi^0$  peak is clearly visible over a background that can best be described with an  $1/E$  dependence. This is a clear indicator that the trigger based on the coincidence of the two  $3 \times 3$  matrices works.

In the context of the Studentenexperiment it was possible to show two things. First of all to derive a valid trigger signal was proven possible to the new APD readout of the CsI(Tl) crystals. The time resolution turned out to be sufficient, to efficiently suppress background while at the same time allow for temporal

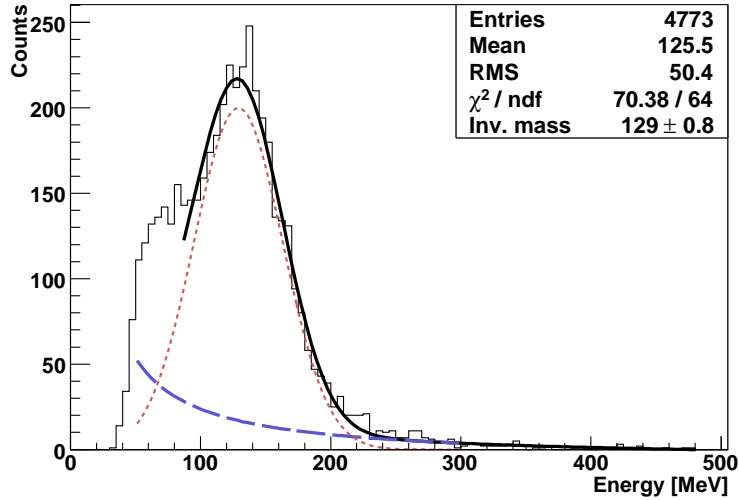


Figure 5.14: Raw count rate data without cuts recorded during the first day of the Studentenexperiment. Here a preliminary energy calibration was used [20]. The  $\pi^0$  peak is clearly visible over the background. The fit consists of a Gaussian (dotted) superimposed with an  $1/E$  background contribution (dashed).

matching of correlated events during the experiment. Second the energy readout turned out to yield sufficient resolution to clearly resolve the  $\gamma\gamma$ -invariant mass of the  $\pi^0$ .

The energy information allows application of time-walk correction techniques. This was already discussed in Section 5.4.1 and will allow the application of much smaller coincidence gates in combination with risetime compensating discriminators. This idea is currently explored in a Diploma thesis [24].

### Time- and energy resolution

As already mentioned in Section 5.4.4 different models of the Shaper revision 4.2 that featured different timing constants were built. The initial idea for this approach was to test whether or not it would be possible to have a single signal path for a combined time and energy signal. During the calibration period at the beginning some of the beam time was also spent on testing the time and energy resolution of those different shaper models. The advantage of using a tagged photon beam for this measurement is that time and energy resolution could be measured for all possible energies in parallel (Figure 5.15). For one crystal/shaper combination only about 5 min of beamtime were needed.

Plots like the one in Figure 5.15 have been recorded for all 18 crystals that were used. The width of the curve in  $y$ -direction reflects the time resolution at a desig-

## 5.6 Timing filter tests with the tagged photon beam

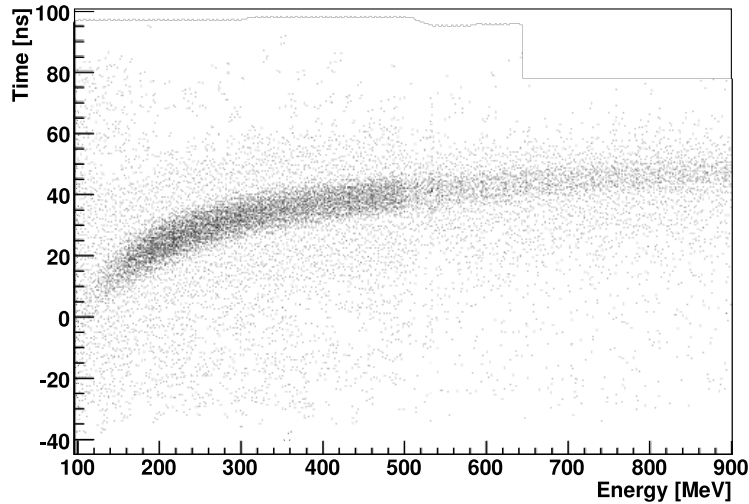


Figure 5.15: Typical time spectrum (shaper rev. 4.2) seen from a single crystal equipped with a Shaper rev. 4.2 readout for all tagged photon energies. The energy is determined by the tagging system. Time in this plot is defined as  $t_{\text{tagger}} - t_{\text{crystal}}$ .

nated energy. By slicing up the scatterplot into different energy bins and fitting a Gaussian to the  $y$  projections the energy dependent time resolution was obtained. The results for three different shaper models are displayed in Figure 5.16.

It is obvious that the shaper specifically designed for trigger timing, namely Shaper rev. 4.2, has the best time resolution ( $\sigma < 3.5$  ns) in the examined energy range. The other two revisions featuring longer shaping time constants, for better energy resolution, have worse timing properties. The  $\sigma_t$  which is plotted here represents the time resolution for close to monoenergetic photons (folded with the resolution of the tagging system). It furthermore constitutes a boundary on what is achievable with time-walk correction.

Although all sorts of photons are produced in the bremsstrahlung process the tagging system makes it possible to sort them according to their energy. That is exactly what has been done here. This simple comparative study already shows that the longer shaping time constants  $\tau$  generally lead to the expected degradation of the time resolution. On the other hand, when looking at the energy side an increase in the resolution is to be expected. This is precisely what is observed. The results are shown in Figure 5.17. To obtain this plot again all measured events were binned according to the tagger energy information. Then the measured distribution of the energy  $E$  was fitted with a Gaussian and  $\sigma E$  was extracted. The relative energy resolution  $\sigma E/E$  can then be plotted versus the incident photon energy as this was done in Figure 5.17.

On the one hand this plot confirms the implicit assumption made in Section 5.3.

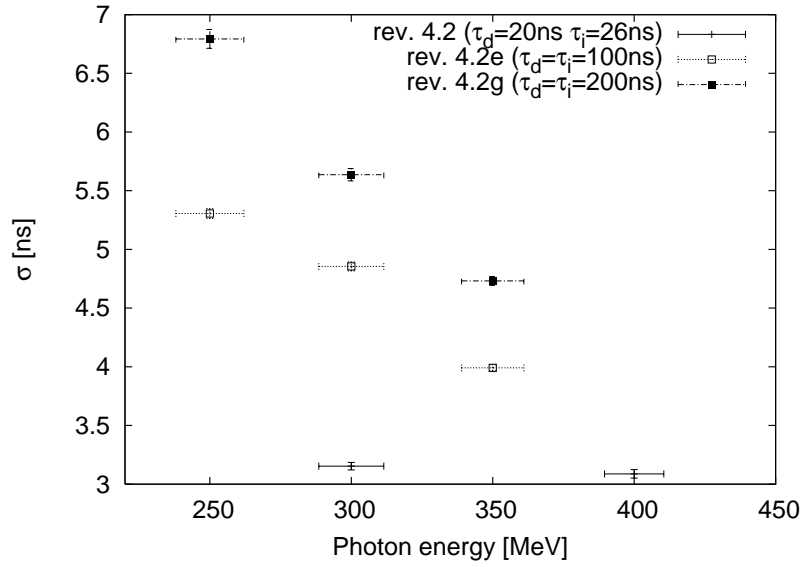


Figure 5.16: Time resolution measurement for different shaper models for central crystal during the in-beam measurement. Due to the gain mismatch of the different shaper models the overlap in possible energies was small. Only a limited number of data points could be extracted.

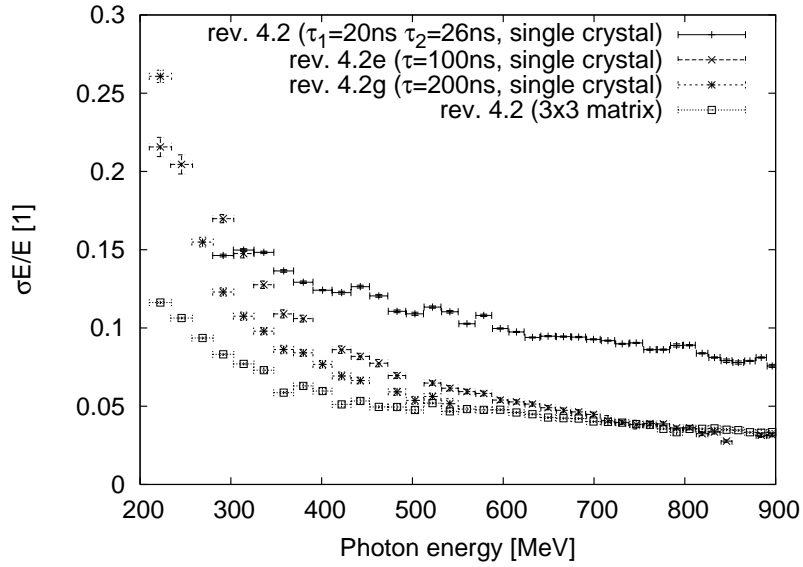


Figure 5.17: Energy resolution measurement for different shaper models in combination with a single crystal and for the full  $3 \times 3$  array respectively (only rev. 4.2). The errorbars on the  $x$  axis correspond to the width of the tagger bars.

A longer shaping time constant  $\tau$  leads to a better energy resolution. On the other hand it also exhibits some more effects that are expected from calorimeters. First of all the relative resolution increases for higher energies. This is mainly an effect of better photon statistics. Second it shows an increase in statistics by summing over several crystals increases the relative resolution by accounting for shower leakage. Third it shows the special behavior of the curve belonging to Shaper rev. 4.2. It looks more flat when compared to the curves belonging to rev. 4.2e and rev. 4.2g. This can most likely be directly correlated with the fact that rev. 4.2 was build with asymmetric shaping time constants  $\tau_d$  and  $\tau_i$ . As for the Studentenexperiment mainly energies below 300 MeV were relevant, this property turned out to be an advantage for the energy resolution in this range of energies.

The comparison of a single crystal rev. 4.2 and a whole  $3 \times 3$  matrix with the same timing filter shows that the gain in resolution is approximately a factor of two.

## 5.7 Timing filter tests with an LED pulser

This section will briefly describe how the Shaper rev. 4.2 was tested with the help of an LED pulser. By injecting light into the crystal, a real event is mimicked. The advantage of that method is that the light output of an LED is perfectly reproducible. Thus a monoenergetic energy source is simulated. However, the resolution is not affected by effects that originate from the scintillation process of the crystal itself. Furthermore the light propagation process within the crystal is different than in the case where the light is produced homogeneously by the crystal itself. Nevertheless this method represents a clean and quick cross-check for the results obtained from cosmic-ray measurements at the laboratory and in-beam measurements at ELSA. The method is furthermore suitable to study the magnitude of time-walk effects at low energy deposits.

### 5.7.1 Experimental method

The LED pulser was initially designed and build as an efficient test of the energy resolution of the setup. It is therefore described in detail in Section 6.1.2 in the next chapter. Nonetheless it was also used for this validation measurement of the time resolution of the Shaper rev. 4.2 in combination with a leading edge discriminator.

For that purpose the LED pulser was tuned to several different light intensities all in the range of 20 MeV to 220 MeV equivalents. Then a TDC spectrum was recorded with a LeCroy 2229 time to digital converter. The Sync output of the arbitrary function generator was used as start signal for the TDC. The obtained spectra were fitted with a Gaussian distribution from which mean and width ( $\sigma$ ) were extracted.

### 5.7.2 Results and discussion

The mean of the stop peak in dependence of the equivalent energy is plotted in Figure 5.18. This measurement shows over what range time-walk effects the time measurement if it is not corrected for.

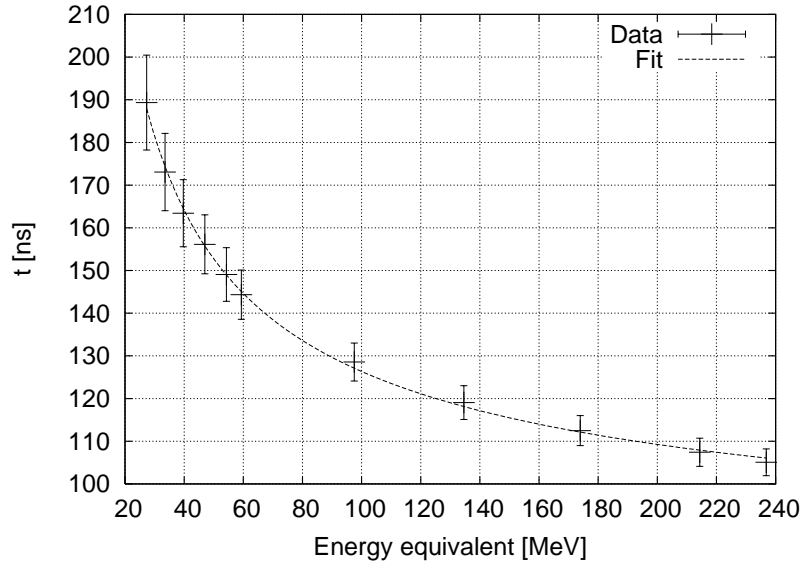


Figure 5.18: Absolute time measurement with the LED pulser for different equivalent energy deposits. The plot shows the true latency of the signal and illustrates the effect of time-walk over the energy range. The  $y$ -error bars reflect the width ( $\sigma$ ) of the stop peak.

Given that information, on-line time-walk correction on discriminator level seems indispensable to gain time resolutions of  $\sigma < 10$  ns over a wide energy range. If time walk correction is applied, the systematic dependence between mean-time  $t$  and energy is removed. The uncertainty of the time correction function then becomes the limiting factor for the resolution. Due to its purely stochastic nature it cannot be corrected and inherently limits the possible time resolution. This is illustrated in Figure 5.19, where  $\sigma$  is plotted with its statistical error from the fit.

Due to the limited precision of the energy calibration with cosmic muons, a systematic error of 10% was assumed on the equivalent energy. Please see Section 6.1.2 for a thorough discussion.

The datapoints in Figure 5.19 have been fitted with the empiric function

$$f(x) = \alpha + \frac{\beta}{x} + \frac{\gamma}{\sqrt{x}}$$

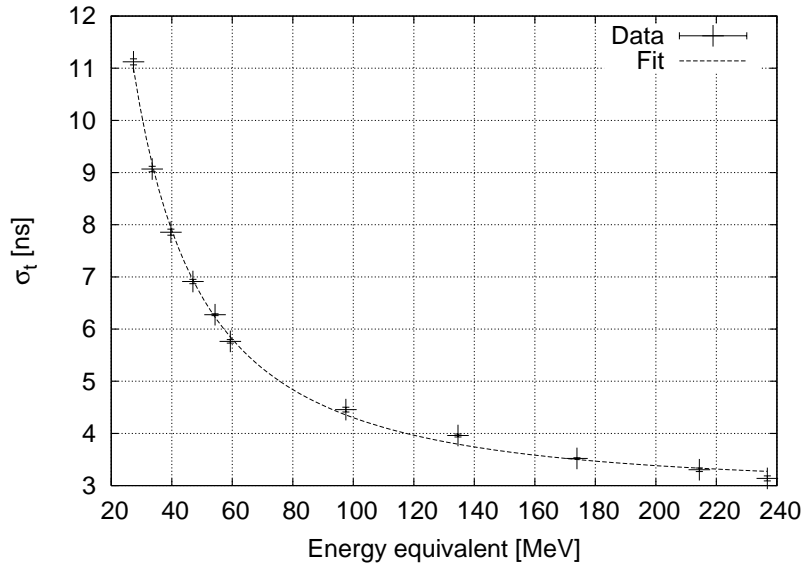


Figure 5.19: Time resolution measurement with the LED pulser for different equivalent energy deposits. The resolutions shown have to be understood as time-walk corrected. Concerning the  $x$ -axis a systematic uncertainty of 10% on the calibration was assumed.

where  $x$  is the energy in MeV. The parameters of the fit  $\alpha, \beta, \gamma$  were found as

$$\begin{aligned}\alpha &= (3.6 \pm 0.4) \text{ ns} \\ \beta &= (350 \pm 24) \text{ ns MeV} \\ \gamma &= (-28 \pm 6) \text{ ns } \sqrt{\text{MeV}}\end{aligned}$$

As expected the measured time resolution agrees very well with the results from Section 5.6. This gives credibility to the values in the range of  $20 \text{ MeV} < E < 100 \text{ MeV}$ , which shows that time resolution decreases rapidly for energies smaller than 50 MeV. It also reflects the fact, that if lower trigger thresholds are needed, a different (longer) shaping time constant will have to be considered. This would ultimately affect the latency of the trigger and eventually violate the initial 200 ns latency requirement.

## 5.8 Summary and conclusion

Starting with an initial latency constraint and a few basic time resolution- and rate requirements for the trigger signal it was shown that the bare preamplifier signal has to be shaped with the help of a timing filter.

Different timing filters were tested. Ultimately a possible solution for a trigger was found in a CR-RC-filter amplifier with time constant  $\tau$  in the order of 26 ns.

## 5 The trigger branch

One prototype was developed in Basel and the Shaper rev. 4.2 was built in Bonn. It was shown that they have comparable properties and that both are capable of fulfilling the latency requirement for a first level trigger signal.

The development of the Basel model focuses on low power consumption, while the Shaper rev. 4.2 is used as a placeholder until a final low power, fully integrated prototype is manufactured in Basel.

As a core parameter of the readout the time resolution was measured by different experiments. First experiments with cosmic muons were conducted to prove the comparability of the two timing filters. Second time and energy resolution measurements were performed at the tagged photon beam at ELSA. Third a LED pulser was used to confirm and crosscheck the results.

It was shown that it is possible to retrieve a signal with a fast risetime (peaking time  $\approx 230$  ns) from the preamplifier signal. It was observed that time resolutions in the order of 10 ns can only be achieved over a large energy range if time-walk correction is applied. The development of risetime compensating discriminator has been underway during the writing of this thesis [24]. For the energy range of  $E_\gamma > 100$  MeV the tests showed that by applying time walk correction, time resolutions  $\sigma(E_\gamma) < 5$  ns are realistic.

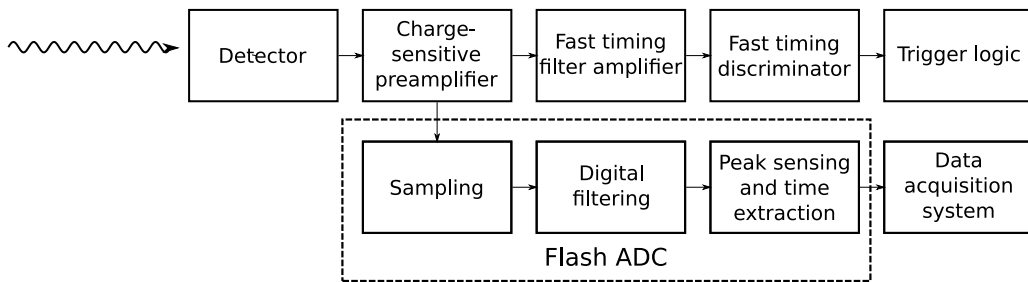


Figure 5.20: Dual readout scheme for time and energy readout achieving nanosecond resolutions, while maintaining the highest possible energy resolution. This is what the final readout concept could look like. The lower readout branch will be covered in Chapter 6.

One of the most important findings of the tests described in this chapter were that a single signal path will obviously not yield optimal time and energy resolution at the same time. Both aims are contradictory in the first place and will always lead to a compromise. Figure 5.20 illustrates how a signal path that avoids this problem could look like. The signal is split at the preamplifier. The two following branches are optimized for time and energy resolution respectively. Based on this knowledge Chapter 6 will now investigate the possibilities and options for the energy readout with FADCs.

## 6 The energy branch

This chapter focuses on how to realize the energy readout with the proposed signal path for the APD setup (compare Section 5.8). Unlike in the case of the trigger branch the latency of the readout is not crucial any more. The information from this branch is only read out when a trigger condition is raised, hence the 200 ns latency constraint can safely be abolished for this task. The primary aim for the energy readout is an optimal energy resolution. A secondary and somewhat controversial aim is the extraction of time information from the signal. Although the trigger branch would be well suited for time readout no TDCs are provided for the readout. To still gain time information from the main calorimeter, the time has to be extracted from the energy optimized signal.

While the trigger branch utilizes the output signal of a timing filter to provide a pulse form that meets the basic requirements for a trigger decision (namely low latency and high time resolution), the energy branch uses the unprocessed output of the charge sensitive preamplifier directly. This has two peculiar advantages. First by not adding active components such as operational amplifiers, inevitable additional noise contributions are avoided. The preamplifier output itself on the other hand is the most general signal that can be obtained from the APD at this point. Any further component downstream alters the shape of the pulse in one way or the other. Most of these alterations have an unidirectional component, which means that information is lost. This is an unwanted effect that has to be avoided.

One possible solution is to digitize the whole signal at a very early stage. In that case the signal is sampled time discretely. All filtering and further signal processing is done digitally thereafter. This idea completely avoids the negative effects of thermal noise or other noise contributions from additional analog circuitry. At the same time it anticipates the necessary step of doing an analog digital conversion at some point. However, this approach raises another issue. Although a variety of problems arising from analog signal processing can be avoided, new problems arise from the digital representation. According to the Sampling Theorem [44] a continuous bandwidth limited signal of bandwidth  $W$  can adequately be reconstructed given it was sampled with a frequency  $f_s$  that satisfies the condition  $f_s > f_N = 2W$ . While this is a mathematically exact statement it is not a priori known that this condition is satisfied by the preamplifier signal. However one can safely assume in the present scenario that this condition can be almost satisfied. For sampling frequencies  $f_s$  that are sufficiently high and signal (and noise) contributions of frequencies higher than the Nyquist frequency  $f_N$  that are at least close enough to zero, the reconstruction will not be affected severely.

## 6.1 The energy readout

As the output of the preamplifier is already proportional to the integrated photon flux, no further integration is needed. Consequently the point of interest of the preamplifier output is the maximum of the pulse. The only information that needs to be read out for the energy extraction is the baseline and the peak of preamplifier signal. Although the baseline should be a constant it might follow a longterm drift behavior. Extracting the baseline also provides an easy and efficient way to detect and correct for pile-up situations. As a consequence the task of the energy readout is very simple. The quantity which is expected to be linear in the deposited energy is given by the maximum subtracted by the current baseline. The baseline and the maximum have to be recorded for every event.

### 6.1.1 Introduction and background theory

There are two key components of the energy resolution measurement. First of all one needs an energy deposit in the crystal of known amount. The knowledge of that quantity should be better than the resolution of the setup. Otherwise the resolution will be dominated by the resolution of the deposit rather than the setup itself. Secondly one would like to have this deposition scalable over a wide range and preferably starting at very low energies to investigate the relative energy resolution in dependence of total energy deposited.

From direct experience with measurements described in Chapter 5 it was obvious that the tagged photon beam did not satisfy these requirements. First of all the exact amount of energy was only known with limited resolution due to the finite width of the tagger bars. Secondly the tagger window for  $E_0 = 1.2 \text{ GeV}$  covers a range of approximately 200 to 1200 MeV, thus leaving out the lower energies which are of particular interest for the performance measurement. Although this measurement is of course one of the most realistic tests it was decided to measure the energy resolution of the electronics itself in the lab. This was done to see whether or not a limiting effect could be found in comparison with the current photodiode readout of the Crystal Barrel.

### 6.1.2 Experimental method

#### The LED test pulser

The simplest way to test the whole electronics chain is to use a light source that emits a specific amount of light directly into the crystal. This light source should be tuneable and reproduce the pulse shape of the CsI(Tl) crystal's scintillation light. For that purpose a simple test setup utilizing an LED in combination with the Agilent 33120A 15 MHz function- and arbitrary waveform generator was devised [25].

The LED is wired to a simple circuit as shown in Figure 6.1. The circuit has a terminated input and R2 is chosen such that the LED's internal resistance

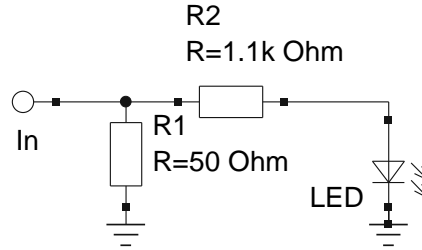


Figure 6.1: Schematic of the circuit used for the LED pulser.  $R1$  establishes an almost  $50\ \Omega$  termination for coaxial input.  $R2$  dominates the total resistance in the case that the diode is kept at threshold and assures that the current through the LED follows the signal from the function generator which is modulated on the offset voltage in a linear fashion.

becomes negligible. Therefore the current through the LED if kept at threshold voltage is proportional to the AC components of the input signal. Assuming that the LED's light output is proportional to the LED current to first order, this setup allows the generation of light pulses of arbitrary shape.

The function generator was programmed with a pulse shape simulating the CsI(Tl) light output. Here a linear rise of 90 ns and an exponential decay with decay constant  $\tau = 1.1\ \mu\text{s}$  was chosen. The constant offset of the function generator to the output was tuned such that the light output followed the programmed pulse shape linearly. The correct operation of the setup was verified by shining the LED's light into a crystal equipped with a photomultiplier tube. Input and output were compared with each other and were in very good agreement (compare Fig. 6.2).

### SADC firmware modifications

In this experiment a modified firmware of the SADC (see Section 4.6) was used. The firmware is capable of extracting information from events with more than 1k samples without leading to congestion in the pipeline of the USB readout. The firmware has the ability to do peak sensing on the input signal by itself. Furthermore the first samples of the rise were stored during the measurement to be analyzed in the context of time extraction (see Section 6.2 for more information).

Although the Zero Chip firmware (described earlier in Section 4.6.1) was readily available, some particular problems in combination with the very long output pulses of the preamplifier were experienced. First the maximum value of the `event size` parameter was limited to 128 samples. In combination with an 80 MHz sampling frequency that resulted in a maximum time of  $128 \times 2.5\ \text{ns} = 1.6\ \mu\text{s}$ . As will be discussed in Section 5.2 the preamplifier signal of the APD readout in combination with CsI(Tl) crystals rises over more than  $5\ \mu\text{s}$ . Therefore this maximum `event size` had to be extended as a first step. Additionally the time extraction

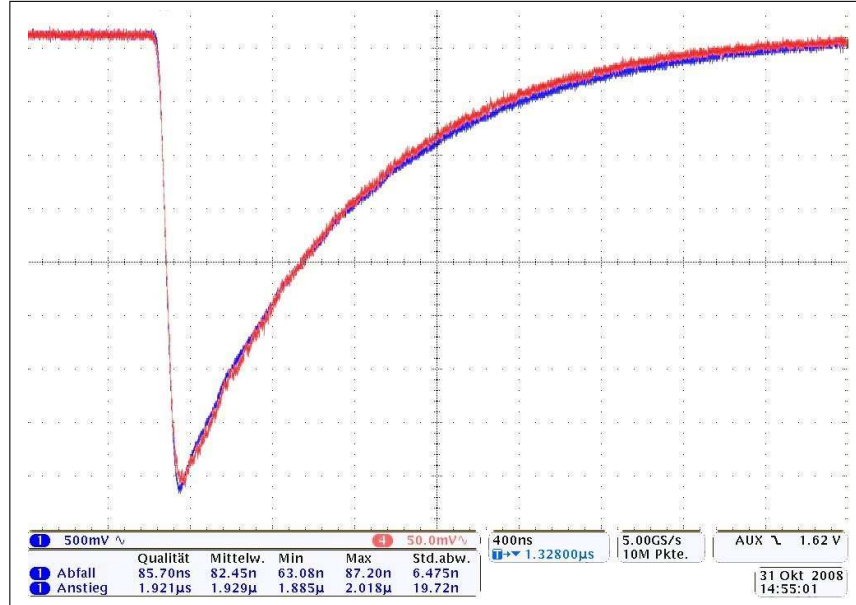


Figure 6.2: Comparison of the signal fed to the LED (in blue) versus the output of the PMT (purple). Apart from the scales the signals are nearly identical and can be conciliated almost to congruence.

that will extensively be discussed in Section 6.2 needed additional digital filtering. The constant fraction discriminator, as it was presently implemented in the Window Trigger firmware v3.00, does not produce sensible results for very long pulses. Therefore it could not be used for the present requirements. This fact can easily be understood. A very long rise sampled with 10 bit resolution will either yield consecutive samples  $p$  that satisfy  $p_{n+1} - p_n = 1$  or  $p_{n+1} - p_n = 0$  respectively. Therefore using only two samples for the constant fraction approach will always result in one of two possible outcomes. It is obvious that such a correction does not add a lot of precision to the final result. In consequence more samples have to be taken into account for a  $t_0$  extraction. The procedure for how this is solved will be described in Section 6.2.

Since the sources of the firmware were made available by Igor Konorov, it was possible to modify the firmware to the present needs. For this purpose the software products Xilinx Foundation and Synplify Pro were purchased. Both are compiler and mapping tools needed to transform the VHDL<sup>1</sup> code into a file that is loadable to the Zero Chip FPGA. To avoid overmapping<sup>2</sup> upon the extension of the SADC firmware the number of active channels had to be reduced. This

<sup>1</sup>VHDL stands for *VHSIC hardware description language*, where VHSIC again stands for Very-High-Speed Integrated Circuits. It is one of the industrial standard hardware description languages used in chip design applications.

<sup>2</sup>Overmapping in that context means that the FPGA is too small for the logic it is supposed to contain.

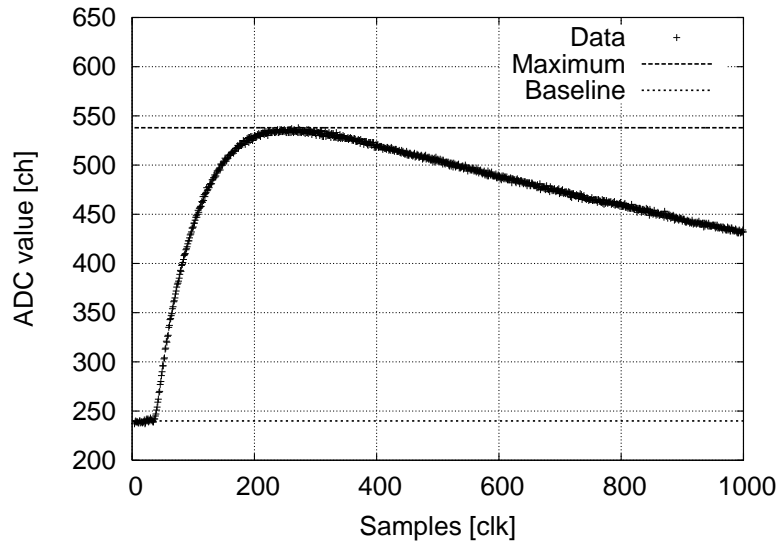


Figure 6.3: Typical pulse as it is analyzed in the Zero Chip FPGA. The event was generated using the the LED pulser and extracted from the SADC using its verbose mode. In normal operation the sampling information is suppressed from the output. As noted in Section 5.2 the tail of the event is cut off as it contains no valuable information.

created free slices<sup>3</sup> on the FPGA for other logic parts. Unfortunately there was no other way to succeed in modifying the firmware. All firmware versions that were derived from the Window Trigger v3.00 were therefore comprising dead channels. It was clear from a start that a way around this had to be found either by using a different FADC or a different firmware in the final revision of the readout. This task is left for the future. However, the limited amount of channels did not impose limitations for the tests. Only a maximum of four channels was needed at a time.

Consequently the Window Trigger firmware was modified to utilize only four active channels for the tests that are presented in this chapter. That approach left enough free logic slices to put further additional features on the FPGA. First of all the FIFO buffers were extended in size to account for the larger `event size`. This firmware ultimately allowed a maximum configurable event size of 1024 samples per event. That allowed following of the preamplifier signal for  $12.8\ \mu\text{s}$  if needed. The rise of the preamplifier signal contains the interesting information, therefore the exponential tail can be ignored (see Figure 6.3 and Section 5.2 for details). As the increased event size lead to congestion at the interfaces somewhere between Zero Chip and USB readout, a further feature was implemented that would allow to only send a certain number of samples to the Secondary Chip, while at the same time including all samples for the maximum detection. This was done by integrating a digital counter that would cut off the data stream in the packet

<sup>3</sup>A *slice* is the smallest usable logic block on an FPGA.

## 6 The energy branch

generator upon reaching a preset limit. This approach allowed the extraction of some 50 samples to be used for the  $t_0$  extraction algorithm. For the present tests this algorithm was run offline. However, the algorithm is designed to reliably run on the FPGA itself (see Section 6.2.3).

### The test setup

For the actual measurement the LED was built into the end-cap of a type-12 crystal with APD readout. A piece of paper was inserted as a diffuse attenuator to prevent that too much light could enter the crystal and oversaturate the readout. The crystal was equipped with the APD readout. The APD was operated at a bias voltage  $U_{\text{bias}}$  of 377.00 V. For the particular APD in use the voltage was corresponding to a gain of 50 (for 25°C) [36]. In a preliminary measurement the linearity of the ADC's peak sensing feature was confirmed by measuring the signal amplitude at the preamplifier's output via oscilloscope and in parallel with the SADC for various different signal amplitudes. No deviation from a linear behavior was seen in this measurement (see Figure 6.4(a)).

In order to investigate the dependence of the preamplifier's output from the peak-to-peak voltage  $V_{\text{pp}}$  applied to the LED's circuit a similar plot was recorded. It is shown in Figure 6.4(b) and exhibits a small contribution from a nonlinear component. The shape was described by a 3<sup>rd</sup> order polynomial which was used for all further analysis to correct the effect.

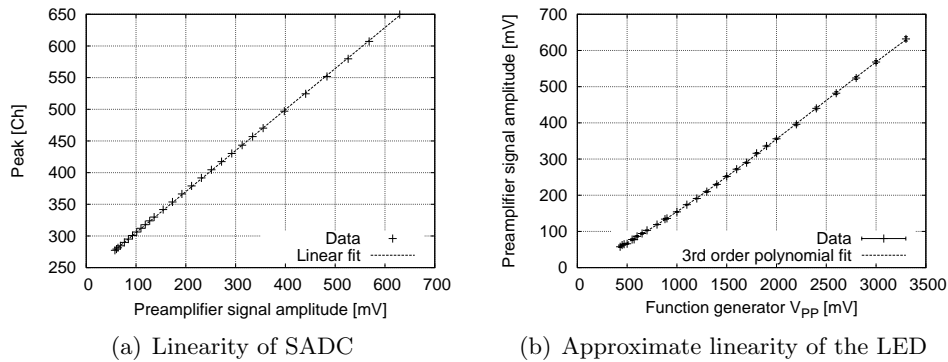


Figure 6.4: The linearity of the different components of the test setup was checked. Where perfect linearity was not achieved, this it was corrected for.

To measure the energy resolution the SADC was used to record a few thousand events of one particular fixed pulse amplitude. It was triggered by the Sync output of the Agilent Arbitrary Function Generator. The ADC spectrum was plotted and the width of the peak was determined from a Gaussian fit (see Figure 6.5). To see the results from this measurement in the context of an actual energy deposition a coarse calibration of the crystal was performed with cosmic muons. The procedure will be explained in more detail in the next section.

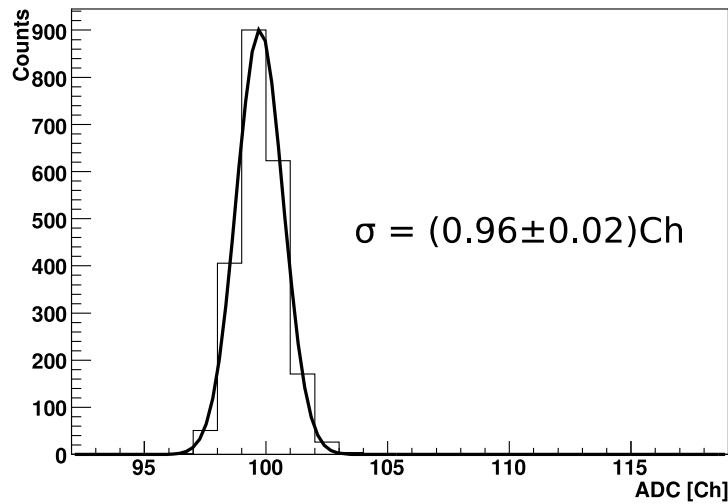


Figure 6.5: Raw energy spectrum recorded with the maximum extraction of the SADC. The coarse binning is given by the finite resolution of the ADC itself.

### Calibration with cosmic muons

To put all the LED measurements in a comparable framework of an energy equivalent, the setup was calibrated with cosmic muons. For this step the LED was turned off and the trigger signal was created with the help of a  $2 \times 2$  cm organic scintillator (trigger scintillator). It was read out by a photomultiplier tube connected to a leading edge discriminator. The discriminator on its part provided the external trigger signal that was fed into the SADC.

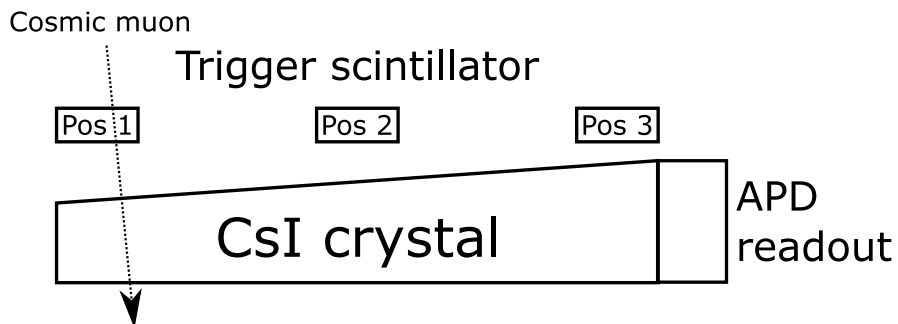


Figure 6.6: Schematic overview of the setup for the energy calibration with minimally ionizing cosmic muons. By varying the position of the trigger scintillator the average length of passage through the inorganic scintillator was altered.

## 6 The energy branch

A simple Geant 4 simulation was used to predict the outcome of the setup. The result is shown in Figure 6.7(a). By finding the most probable value (MPV) of the Landau distribution as a reference, the SADC channel numbers could readily be matched to their energy deposits (see Fig. 6.7(b)).

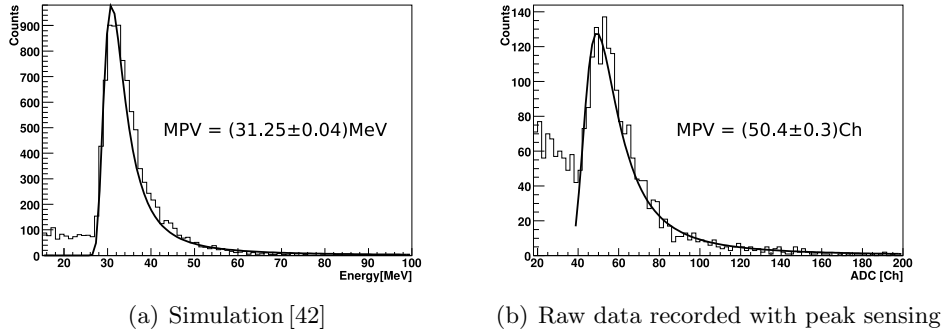


Figure 6.7: Simulated and raw SADC spectrum for Position 1 as shown in Figure 6.6 with a Landau shape fitted to each plot.

As the energy deposition of minimally ionizing particles scales linearly with the thickness of the material they pass through, the calibration curve has to yield a straight line. This was also found to be the case, as is shown in the “Upright profile” measurement in Figure 6.8.

Interestingly the offset of the line fit did not resemble the pedestal, which was found to be at 242 ch during this measurement. Therefore in order to verify the result, a second measurement was performed the next day. During that measurement the crystal was placed on its side (Lying profile) thus giving shorter distances of passage for the mostly vertically incidental muons. The overall energy deposition therefore has to be lower. Instead of finding all points lying on the same line as expected, a second linear dependence was found. This dependence happens to have a slightly different slope parameter ( $\approx 20\%$  difference) and as is obvious from Figure 6.8 also has a different offset. However in this measurement the offset parameter from the fit nicely reproduced the pedestal at 242 ch.

Now there are two likely explanations for this. The only control parameter that was changed between the measurements was the position of the crystal itself. Furthermore the attenuation of the scintillation light during its travel through the crystal was not included in the measurements. It is most likely that this attenuation can best be described by an exponential shape.

All attempts to align both sets of datapoints on a single line by this approach failed. This might also be brought forward by the fact that there were relatively little datapoints with quite large error bars. However, it also suggests that it cannot be the only reason for the mismatch.

One other parameter that was not controlled was the temperature. As was explained earlier in Section 3.2, the gain of an APD is very sensitive to temperature

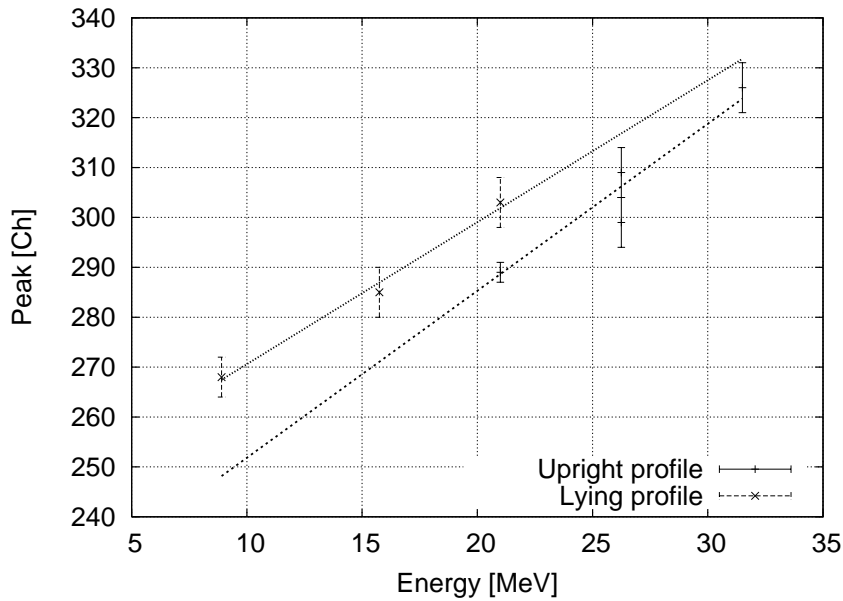


Figure 6.8: Calibration curves for two distinct calibration measurements. The crystal was either lying on its side (lying profile) or in perpendicular position (upright profile).

differences. As the temperature was not a stable parameter during the measurements it is most likely that the distribution of the data points is mainly due to this fact. Further control measurements that followed, where the only parameter that was the temperature, confirmed this assumption.

Changing the temperature of the setup was achieved by using the air conditioner's maximum and minimum settings in the room where the setup was located. The results strongly supported the explanation that the mismatch of the calibration lines is temperature dependent.

As a direct consequence it was found that it is not possible to do a high precision calibration of the current setup. For the final analysis all datapoints from all measurements were taken into account. To accommodate for the limited precision of the calibration a systematic uncertainty of 10 % (66% confidence level) was estimated.

### 6.1.3 Results and discussion

Despite the problems of obtaining a precise absolute calibration it was possible to retrieve meaningful results for the energy readout branch. Most importantly the energy resolution for the readout electronics was measured for different energy equivalents and the result is shown in Figure 6.9.

## 6 The energy branch

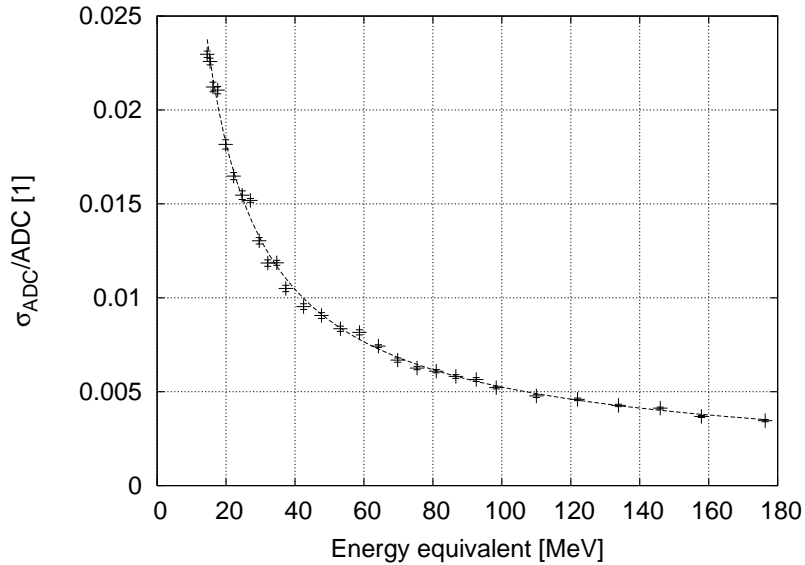


Figure 6.9: Energy resolution for the electronics of the energy readout branch measured with the LED pulser test setup. Errorbars in  $x$ -direction have been omitted for clarity. However the  $x$ -axis has to be interpreted with a 10% relative uncertainty from the calibration.

A function that describes the data points very well was found to be

$$\frac{\sigma_{\text{ADC}}}{\text{ADC}} = \frac{\alpha}{E} + \frac{\beta}{\sqrt{E}} \quad (6.1)$$

where  $E$  has to be understood in units of MeV. The parameters  $\alpha$  and  $\beta$  were obtained from the least squares fit and were determined as

$$\begin{aligned} \alpha &= (0.234 \pm 0.007) \text{ MeV} \\ \beta &= (0.029 \pm 0.001) \sqrt{\text{MeV}} \end{aligned}$$

Although the calibration has a large uncertainty it is safe to say that the energy resolution for energies beyond 100 MeV is well below the 1% level. Furthermore when trusting the fit of Equation 6.1 there are strong indications that the resolution of the setup still stays below the 5% marker for energies  $E$  in the range  $10 \text{ MeV} < E < 100 \text{ MeV}$ .

One cannot neglect the fact that these results have been obtained by using a LED pulser rather than real photons of known energies impinging one of the CsI(Tl) crystals. Further measurements will have to be conducted to study the limiting effects of the scintillating crystal itself and the shower leakage. Nevertheless the measurements give valuable information about the APD readout.

To evaluate these results with the present readout, they have to be compared with a measurement from the time when the Crystal Barrel detector was still

operated at LEAR. The energy resolution was measured with the help of the reaction  $p\bar{p} \rightarrow \pi^0\gamma$  where the monoenergetic  $\gamma$  with energy  $E_\gamma = 933.4 \text{ MeV}$  was used to find the relative energy resolution  $\frac{\sigma E}{E}(933.4 \text{ MeV}) = 2.5\%$ . The second measurement was conducted via the reaction  $p\bar{p} \rightarrow \pi^0\eta$ . An energy resolution of  $\frac{\sigma E}{E}(95 \text{ MeV}) = 5\%$  was extracted [1].

One can finally conclude that the APD in combination with the tested readout electronics seems to yield energy resolutions, which exceed the resolution of current energy readout by a factor of 2 to 5. Consequently it makes sense to assume that the APD readout could improve the resolution of the energy readout, if the limiting factor so far was given by the photodiode readout itself. However, if the resolution limits of the current readout are mainly imposed by the scintillation process, shower losses or other unknown sources of uncertainty, the current resolution will at least not deteriorate upon the change to an APD based readout.

### 6.1.4 Future improvements

Using the standard maximum extraction feature of the Window Trigger firmware (see Section 4.6.1), no filtering is applied to the input signal. Therefore the maximum value extracted is distorted by input noise contribution. It is very likely that a simple averaging algorithm will further improve the performance of the energy readout significantly.

A fixed summation over a certain number of samples and the extraction of that value could help in increasing the resolution and the dynamic range of the ADC. Extracting the maximum from a summation window spanning four 10 bit values would already yield 12 bit of information thus increasing the resolution of the device. At the same time it would act as a low pass filter thus discarding high frequency noise components. It is possible to gain further improvement of the energy resolution by extracting the slope parameter of the rise of the signal. This problem has already been solved algorithmically for the purpose of the  $t_0$  extraction (see Section 6.2.4). The solution for this could further be exploited towards a better energy resolution. The slope parameter should be linearly correlated with the energy deposition to first order. Since the slope parameter only relies on the fact that the first 50 samples are within the dynamic range of the ADC, this approach would also offer the possibility to artificially increase the dynamic range of a FADC beyond the intrinsic ADC resolution.

## 6.2 The time readout

One of the aims of the new readout is to gain time information from the main calorimeter. It seems controversial to extract time information from the energy branch instead of the trigger signal. Yet the method allows to gain time information without using additional TDCs in the trigger branch.

For the extraction of the time information from the preamplifier signal, the same sampling information is used as for the energy extraction. While the energy

readout relies on extracting the baseline and the maximum of the preamplifier signal (see Section 6.1) it can be easily understood that the main time information is encoded in the turning-point and the leading edge of the signal (compare Figure 5.1).

### 6.2.1 Introduction and background theory

In a classical setup without FADC, dedicated components would be required to do time measurements. Firstly a discriminator would be used to generate a digital pulse from the analog input and secondly a time to digital converter (TDC) would measure the time difference between that digital pulse and a dedicated time reference. In general the time reference is a signal which is derived from the trigger signal.

When extracting time with a FADC these two steps are essentially the same. The only difference is that the process is happening on digital data. Just like in the classical analog the discrimination process can be done in different ways. A discriminator can compensate for rise time effects or it can simply be a comparator with an adjustable threshold. Either option ultimately effects the outcome of the measurement. The TDC equivalent in the FADC is implemented by counting its internal clock cycles. In the experiment the clock of the FADC is synchronized with the DAQ system and can be correlated to the trigger time. In the present case where only one SADC module was used, only the freely running internal clock was available.

Every result will usually be expressed in terms of its clock cycles  $clk$  unless stated otherwise. The clock frequency used for the tests was 80 MHz, and therefore  $clk \equiv 12.5$  ns.

One way to approach time extraction is to implement a simple threshold detection and use the current clock cycle as time reference for the occurrence. Classically that would come closest to a leading edge discriminator. This can easily be done with the SADC and the feature is implemented in the standard firmware. The tradeoff of this method despite its simplicity is that the resolution is now limited by the clock speed of the ADC. As the input signals are generally not synchronized with the clock of the SADC a jitter of  $\pm 1/2$  clock cycle is to be expected.

### 6.2.2 Simulations

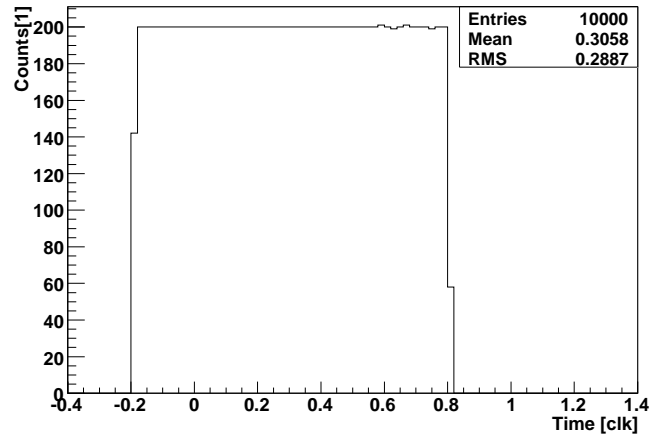
To illustrate the idea of clock jitter, a simple simulation of the situation was implemented using the C++ programming language. With regard to the actual shape of the signal, two simple requirements were imposed onto the analytic function used in the calculation. Namely the function should rise linearly at close to  $t_0 = 0$  and ultimately slowly approach its maximum in an almost flat plateau as these are the key features of the preamplifier output (compare Fig. 5.1). One function which certainly fulfills these two simple requirements is a sine function. Conse-

quently the half period of a sine function was used for the simulation. In the code the sine was sampled at  $N$  discrete points  $x_n = B \sin(\pi n/N + \delta t) + \Delta$  within the first half period, where  $B$  is the dynamic range and if desired a portion of Gaussian noise can enter the simulation via  $\Delta$ . The offset  $\delta t$  was chosen from the interval  $-N/2 < \delta t < N/2$ . For a given threshold  $a$  one can now assign  $t_{le}$  with the value of smallest  $n$  that satisfies  $x_n > a$ . This idea follows the basic working principle of the leading edge discriminator. If one now defines  $t = t_{le} - \delta t$  a plot like the one shown in Figure 6.10(a) will result. The square plateau that can be seen reflects exactly the fact that the pulse jitters within one clock cycle. The root mean square (RMS) was found to be 0.29 clk. Figure 6.10(b) shows the effect of a very small amplitude of additive noise ( $\sigma = 1$  ch). In that case the RMS value was found to be 0.50 clk. This illustrates that not only is the algorithm limited by the clock frequency, but it is also very susceptible to noise.

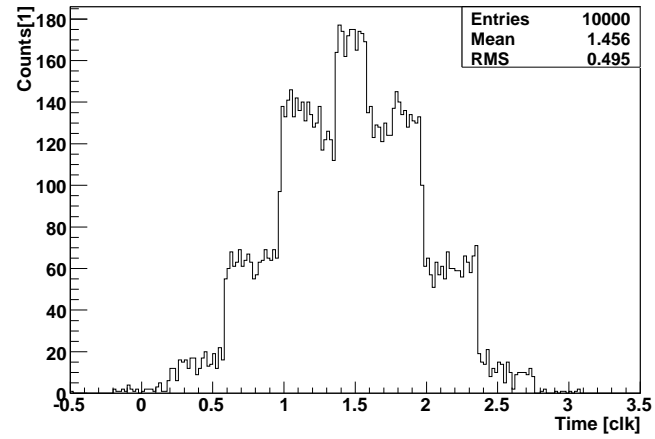
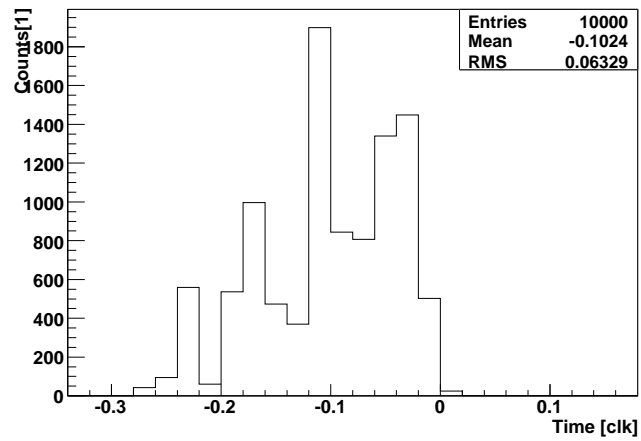
The naive solution to a better time resolution would be to increase the sampling frequency  $f_s$  to the desired time resolution. This possibility is not feasible for several reasons. First of all the signals are not noise free (see Figure 6.10(b)). Secondly the sampling frequency and also the resulting higher data-rate have both technical limits and their cost. If time resolutions below the internal clock frequency are required, some sort of clock interpolation has to be performed. This is usually done by making an assumption about the shape of the signal. Depending on the assumptions the true starting point of the signal  $t_0$  can then be reconstructed with differing precision.

The rise of the preamplifier signal lies in the order of some  $5 \mu s$ . With a sampling frequency  $f_s$  of 80 MHz that corresponds to approximately 400 samples. The question is whether it is possible to properly extract  $t_0$  when only analyzing the first samples of each event. Such a scenario is shown in Figure 6.11 for three cosmic muon events of different energy deposition. All recorded samples are plotted consecutively as they appear in the datastream. They were not causally linked to each other. The flat areas between the rising parts are events where an external trigger fired, but no muon was seen in the crystal. These events would normally contribute to the pedestal. Judging from the rise itself, the general behavior seems to be dominated by a strong linear component.

Starting from these considerations a simple linear regression was implemented in the simulation software and applied to the artificially generated samples. A fixed number of 20 samples from the rising edge were used for the calculation. From the linear function that was obtained by the fit,  $t_0$  was determined as the line's intercept with the baseline. Two typical results are shown in Figures 6.10(c) and 6.10(d) where again  $t = t_0 - \delta t$  is shown. A RMS value of 0.06 clk was extracted from Figure 6.10(c), which shows that the fit technique gives better results than the threshold approach. In case of a noisy signal the resolution of the technique suffers but performs still better than the threshold algorithm (see Figure 6.10(d)). Finally the results from the simulations suggest that this simple assumption obviously leads to an improved time resolution which exceeds the resolution possibilities of the leading edge approach.



(a) Threshold approach, without noise.

(b) Threshold approach, with Gaussian noise ( $\sigma = 1$  ch).

(c) Linear fit, without noise.

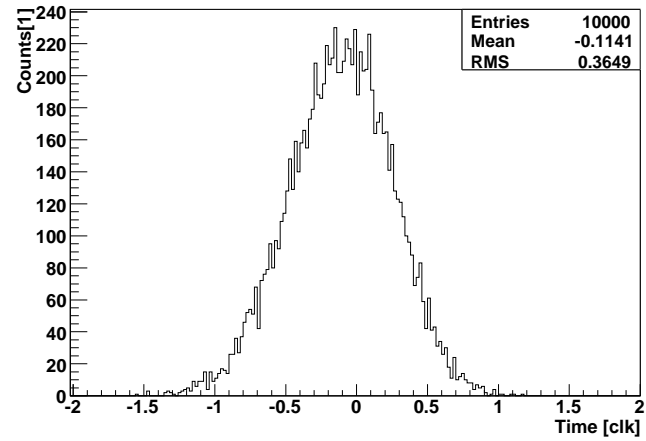
(d) Linear fit, with Gaussian noise ( $\sigma = 1$  ch).

Figure 6.10: Results from time resolution simulations.

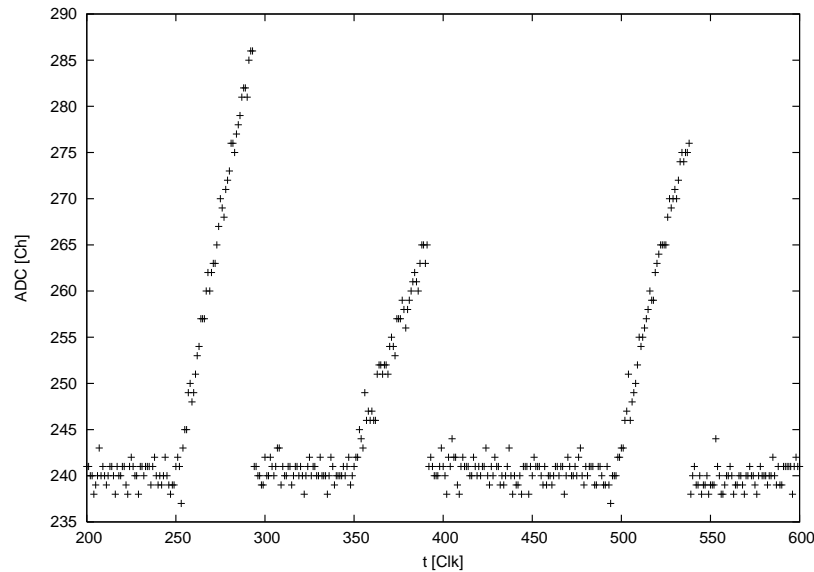


Figure 6.11: Three cosmic muon events as recorded by the SADC. The firmware suppresses all sampling data beyond the first 50 samples. The flat areas between the rises are events contributing to the pedestal.

### 6.2.3 Linear fit time extraction

It turns out that the linear fitting technique has further advantages over other approaches. One advantage of this technique is that it automatically corrects for pulse height and therefore also for timewalk effects, similar to the way a constant fraction discriminator does. Suppose you start with a given set of samples  $p_1 = \{x_n\}$ . As the timing constants of the signal are fixed by the crystal itself a second pulse  $p_2$  with a different size could be given by  $p_2 = \chi \{x_n\}$  where  $\chi$  is a real parameter. Thus the signal is scaled in the  $y$ -dimension. Consequently the linear fits of form  $f(t) = A + Bt$  will accommodate for that fact by satisfying  $f_2(t) = \chi f_1(t)$ . As  $t_0$  computes as  $t_0 = -A/B$  and from  $f_2(t) = \chi f_1(t)$  follows that  $A_2 = \chi A_1$  and  $B_2 = \chi B_1$  respectively, it is easy to see that  $\chi$  cancels in the fraction  $A/B$  and therefore  $t_0$  is left unaffected.

Another advantage of linear fitting technique is that all relevant parameters can easily be calculated on the fly. That means that only little memory is needed. This fact becomes important when the algorithm is to be implemented on an FPGA. It turns out that it is sufficient to calculate two sums while sampling the signal. The extraction of the two numbers is fully sufficient to calculate the linear fit offline and represents a substantial datarate reduction (see Appendix B for details).

Although the method has certain advantages, due to quantization errors the achievable resolution is limited by the choice of the dynamic range  $E_{\max}$  and the number of bits that are available to the ADC. If the uncertainty of the baseline

## 6 The energy branch

extraction is omitted, the limit of the possible resolution is given by

$$\sigma_{t_0}(E) = \frac{1}{\sqrt{12}} \frac{N \Lambda_N E_{\max}}{\alpha 2^r E} \Delta t \quad (6.2)$$

for a number of significant samples  $N \geq 20$ .  $\alpha$  is a constant which is dependent on the pulse shape,  $r$  is the number of bits used by the ADC and  $\Delta t$  is the sampling interval. Finally  $\Lambda_N$  is a constant which is only dependent on  $N$ . The full derivation of Equation 6.2 is given in Appendix B. Figure 6.12 illustrates this dependence for typical parameters as they are used during the tests ( $E_{\max} = 300$  MeV) and as they would become important in the case of the Crystal Barrel experiment ( $E_{\max} = 2$  GeV).

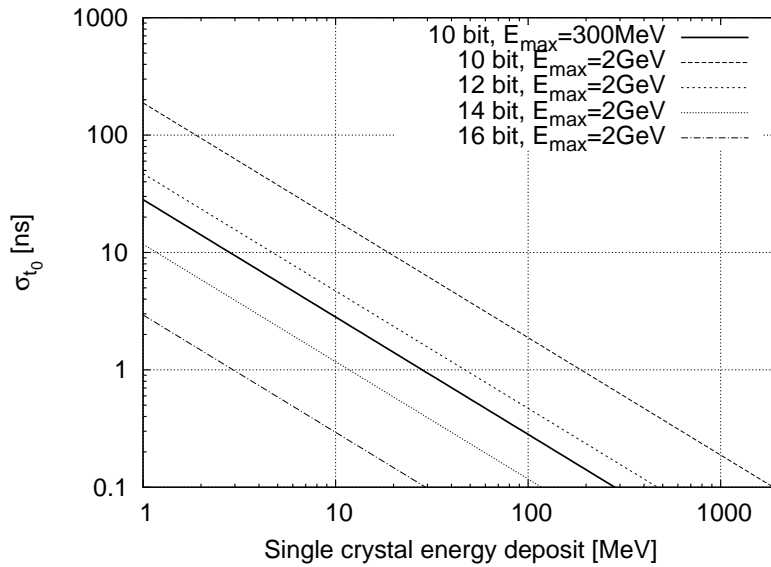


Figure 6.12: Estimated time resolution achievable for different ADCs and dynamic ranges. The parameters were chosen as  $N = 40$ ,  $\alpha = 0.48$ ,  $\Lambda_N = 2.04$  and  $\Delta t = 12.5$  ns. The underlying relation is given as Equation 6.2.

Based on this preliminary work, an experiment was devised to test the  $t_0$  extraction with the help of a linear fit to a small number of consecutive samples of the rising edge of the signal. The aim of the experiment was to measure the time resolution that could be achieved with the given crystal, the present APD, the LNP preamplifier and the SADC. A detailed description of this work is given in the following section.

### 6.2.4 Experimental method

To measure the time resolution of the energy readout branch the setup shown in Figure 6.13 was used. The whole measurement was performed using cosmic

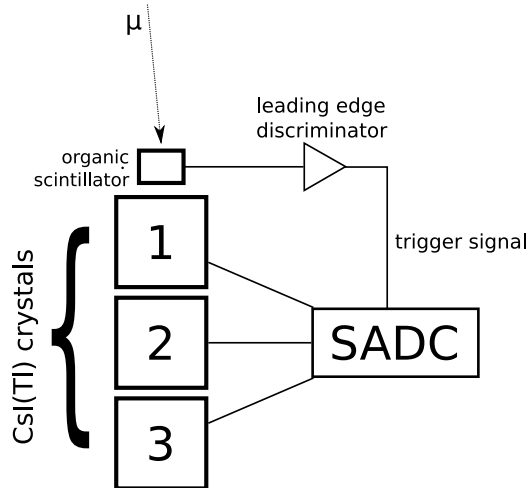


Figure 6.13: Schematic of the setup used for the time resolution measurement with cosmic muons. It was geometrically assured that the incidental muons would pass through all three crystals.

muons. A  $2 \times 2 \text{ cm}^2$  organic scintillator in combination with a leading edge discriminator was used to generate the trigger signal. Three type 12 CsI(Tl) crystals arranged on top of each other were read out simultaneously in order to be able to ensure that the incident muon was passing the setup close to vertically. The bias voltage of the APDs was adjusted to match the gains of the three APDs. The SADC was run in its 80 MHz mode. The firmware was a modified version very similar to the firmware used in the energy resolution measurement (see Section 6.1.2). The SADC was configured in a way to extract the pulse maximum within the first 1 k samples after receiving the trigger signal. This is the familiar peak sensing feature as it has been introduced in Section 6.1 for the energy readout. This information was recorded for cross-checking. The external trigger signal was fed into channel one. The SADC was operated with 4 channels that were read out in latch-all mode (i.e. all channels are read out without zero suppression). Each event was comprising the internal clock value, the baseline and the first 50 samples of each channel. All further feature extraction and cuts on the coincidence on all three crystals was done in software.

As an input channel is used for triggering it is obvious that also the trigger time  $t_{\text{trig}}$  of the SADC jitters within the clock cycle as illustrated in Figure 6.10(a). As the trigger signal is a standard NIM pulse with a risetime much shorter than the sampling frequency, it is not possible to get a better resolution with the help of enhanced fitting techniques. Therefore the resolution is limited by the clock frequency of the SADC.

To still be able to measure the precise time resolution  $\sigma(t_x)$  of each crystal without being limited by the clock resolution, it is important to readout the three coincident crystals. This approach allows the measurement of three different

## 6 The energy branch

time differences  $t_{1,2,3}^d$  and the corresponding resolution. The single crystal time resolution can then be extracted.

Suppose that energy was deposited in all three crystals. The zero crossing of the linear fits will yield the three times  $t'_x = t_x + \Delta t_{\text{trig}}$  where  $x = 1, 2, 3$  corresponding to each crystal. It is obvious that all times  $t'_x$  will be shifted by the jitter of the trigger  $\Delta t_{\text{trig}}$ . Nevertheless, the time differences  $t_1^d = t_1 - t_2$ ,  $t_2^d = t_1 - t_3$  and  $t_3^d = t_2 - t_3$  will be free of the influence of the trigger time. As all time differences should be constant, the finite resolution  $\sigma(t_x^d)$  can be measured directly from the data. Deriving the true time resolution  $\sigma(t_x)$  of a single crystal from the time difference resolution  $\sigma(t_x^d)$  is a simple matter of solving a set of linear equations. Given that the condition  $\sigma(t_1^d) \approx \sigma(t_2^d) \approx \sigma(t_3^d)$  holds, the time resolution of a single crystal can be further simplified. It is then given by the following expression

$$\sigma(t) = \sigma(t_x) \approx \frac{\sigma(t_x^d)}{\sqrt{2}} \quad (6.3)$$

To measure the time differences  $t_{1,2,3}^d$ , the raw data stream from the USB read-out was decoded with the tool `streamusb` and then further processed by `awk` scripts that also performed the linear fitting and  $t_0$  extraction (see Figure 6.14). The trigger delay timings of the SADC were chosen such that the first samples recorded belonged to the baseline. A total of 50 valid samples was extracted for each event, to make it possible for the analysis to observe how the fit performs with different numbers of data points. To avoid confusion among the three crystals the time  $t_0$  is indexed 1, 2, 3 for the three different crystals, while the zero is left out.

Over the course of one weekend the setup recorded approximately 8 k coincident events which were used in the analysis. The expected Landau distribution was found for each of the three energy spectra. This was done to confirm that no spurious coincidental data, like noise-bursts, was recorded. Figure 6.15 shows the spectra for the three possible time differences between the three crystals.

### 6.2.5 Results and discussion

A Gaussian has been fitted to each to extract the time resolutions from the time difference spectra  $\sigma(t_x^d)$  in Figure 6.15. As expected the extracted values are similar and for the further calculus the approximation from Equation 6.3 will be used. Taking the worst time difference resolution (Fig. 6.15(c)) as a starting point  $\sigma(t_3^d) = (0.766 \pm 0.008)$  clk and noting that  $1 \text{ clk} \equiv 12.5 \text{ ns}$ , the time resolution of the single crystal is found to be

$$\sigma(t) = \frac{\sigma(t_3^d)}{\sqrt{2}} \approx (6.77 \pm 0.07) \text{ ns} \quad (6.4)$$

It can be argued that including too many samples into the linear fit might degrade the quality of the fit. The more samples are taken into account, the more

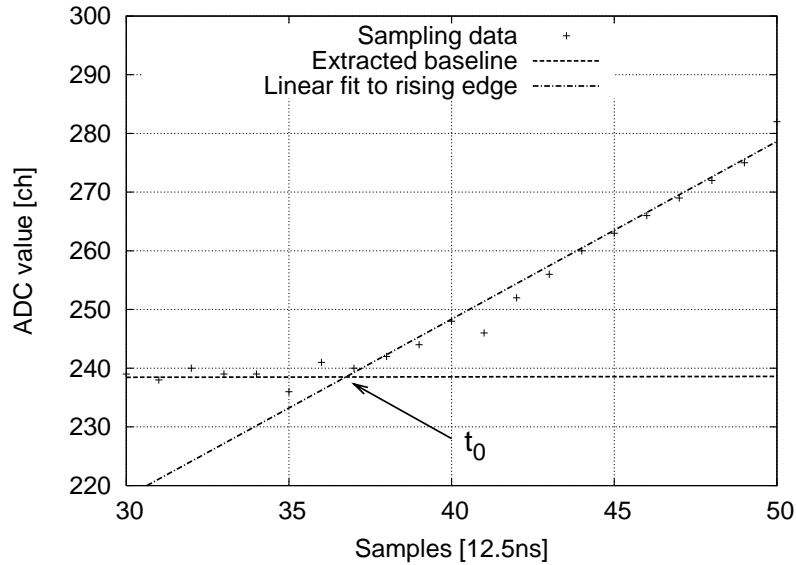


Figure 6.14: The intersect of the averaged baseline and the linear component of the slope is used for  $t_0$  extraction from the datastream.

the nonlinear components of the rising edge of the pulse start to contribute. In other words the pulse shape starts to curve down. On the other hand including too few samples will result in too little statistics for the method to work.

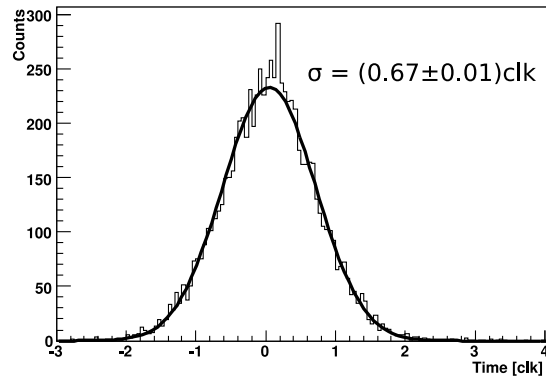
To study this phenomenon the whole analysis was repeated for a different number of samples in the linear fit. The results of this analysis are shown in Figure 6.16. The plot illustrates two key features. Firstly it shows that if there are only 15 samples or less included in the fit the resolution  $\sigma_t$  gets worse. Secondly for linear fits including 20 samples or more the resolution seems to converge suggesting that the resolution seems to be limited by more than simply the number of samples in the linear fit. Furthermore one can note that when only looking at the first 40 samples a negative effect of nonlinear components cannot be seen.

### 6.3 Summary and conclusion

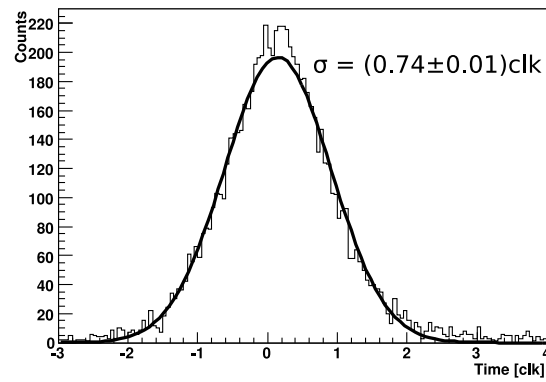
Summarizing the results of this section it can be said that the preamplifier signal is well suited for an energy readout. Using the preamplifier signal directly avoids the introduction of additional noise from further electronic components along the signal path. The slow rise and decay are easily sampled at a sufficiently high rate with standard technology.

Several test experiments using an LED pulser and cosmic muons have been performed to show the energy resolution and the quality of a  $t_0$  time extraction based on a linear fit. The energy resolution of the electronics was found to be better than 1% for energies higher than 100 MeV and therefore substantially better

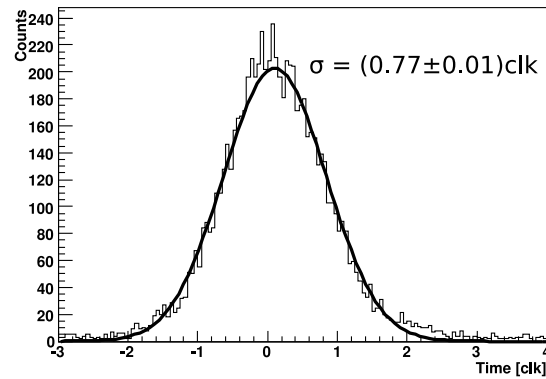
6 The energy branch



(a)  $t_1^d$



(b)  $t_2^d$



(c)  $t_3^d$

Figure 6.15: All possible combinations of time differences. The time extraction was performed with the linear fitting technique. 6 samples were used for baseline extraction and 40 samples for the linear fit.

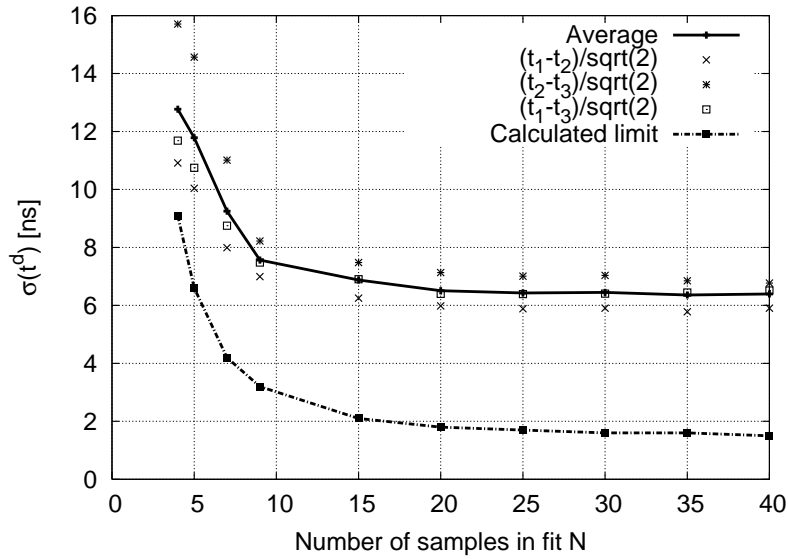


Figure 6.16: Resolution of time difference  $\sigma(t^d)$  versus the number of samples included in the linear fit  $N$ . The data have been divided by  $\sqrt{2}$  to allow comparison with single crystal resolutions. The calculation was performed for a dynamic range of  $E_{\max} = 300$  MeV, an average energy of  $E = 30$  MeV and a value of  $n = 6$  (see Appendix B).

than needed to reproduce or possibly even outperform the energy resolution of the current Crystal Barrel readout.

Finally the approach of extracting time information from the pulse shape with the help of a FADC was proven to work. The simple assumption that the initial rise of the preamplifier signal comes close to a straight line led to the development of a linear fit method that uses little memory and can easily be implemented in VHDL to run on a FPGA. The method was tested and benchmarked in offline tests. For cosmic muon events with a most probable energy deposition of 30 MeV the time resolution with this method was found to be  $(6.77 \pm 0.07)$  ns. For  $n = 6$  and  $N = 40$  the calculation of the quantization error results in  $\sigma_{t_0}^{\text{calc}} = 1.5$  ns. This means that the fitting technique is still dominated by noise on the signal. However, this measurement was done for a reduced dynamic range of approximately 300 MeV. To cover a range of 2 GeV the quantization error for the same FADC is estimated to rise to 6.5 ns. It is then in the same order of magnitude as the measured resolution. Therefore a FADC with at least 12 bit resolution or better (see Figure 6.12) would be needed.

Finally it can be concluded that the presented method is a promising way of extracting energy and time information from an integrated preamplifier signal of a CsI(Tl) crystal. However, ADC resolution and noise impose strict limits to the achievable resolution.

## 6.4 Outlook

Although the results are very promising, there are several possible starting points for future improvements of both the method and the equipment. Due to the lack of a monoenergetic photon source of sufficiently high energy (10-30 MeV) all energy resolution measurements have been done using the LED pulser. To be really sure the readout will have to be tested with real particles. There are two viable approaches to this test. First an in-beam measurement at a tagged photon beam could yield valuable information on the energy resolution. Second a full experiment, similar to the Studentenexperiment in combination with the reconstruction of the  $\pi^0$  and its associated width, would give the ultimate benchmark. The latter idea is already being considered for the 2009 Studentenexperiment. One very important future task is also to optimize the homogeneity and intensity of the light collection. Different approaches are outlined in [24]. Finally further methods of digital filtering could possibly improve the energy and time resolution.

## 7 Summary and conclusion

The aim of this work was to study a possible avalanche photodiode readout for CsI(Tl) crystals as they are used in the Crystal Barrel calorimeter. The focus of this study lay on the development of first level trigger ability for such scintillating crystals, with definite timing constraints. Secondary aim was to develop and evaluate possible readout mechanisms to achieve energy resolutions that resemble the resolution of the current readout of the Crystal Barrel detector. Finally it was a central question if this readout could in addition also provide time information from a slowly rising signal.

This work was based on three initial building blocks. First there was the LNP preamplifier for the APD readout designed by M. Steinacher at the University of Basel [40]. Second a  $3 \times 3$  CsI crystal matrix was already converted to APD readout using such LNP preamplifiers at the University of Giessen. Third a FADC designed at the TU Munich was available including the VHDL sources for the firmware.

During the first part of this work it was understood that the preamplifier alone was not capable of providing a trigger signal that meets the required latency constraint. Therefore a solution based on a fast timing filter amplifier was devised in collaboration with the University of Basel. To build a contemporary test with such a timing filter, contact with the group of Prof. Löhner at the KVI, Groningen was established. One of their filter designs was adopted and modified in Bonn to work with the LNP preamplifier and the present CsI crystals. It was possible to show that this so called Shaper rev. 4.2 was capable of producing a valid trigger signal. With the obtained signal it was possible to meet the initial 200 ns latency constraint. A total of more than twenty boards of this circuit were manufactured during this thesis.

Several tests revealed that the time resolution provided, was high enough for triggering, thus satisfying the main goal for the transition to a new APD readout. To test the new trigger and time readout a second  $3 \times 3$  matrix was built and equipped with the LNP preamplifier and the Shaper rev. 4.2. The two blocks were used as detectors in coincidence (100 ns coincidence gate) during the Studentenexperiment. In this context it was proven that the CsI crystals in combination with the APD readout and a fast timing filter can be used for a low latency low-noise trigger.

It was possible to show that the crystal readout did not saturate at rates up to 6 kHz. For the given shaper monoenergetic time resolution was shown to be better than 3.5 ns ( $\sigma$ ) for photon energies higher than 200 MeV. Strong evidence in LED pulser tests was found that the monoenergetic time resolution is better

## 7 Summary and conclusion

than 15 ns for energies down to 25 MeV. However, the measurement of the energy resolution showed that this fast rising signal was not capable of providing the required energy resolution. Consequently a new readout solution was devised, in which energy and trigger signals are treated in two differently optimized signal paths (see Figure 7.1).

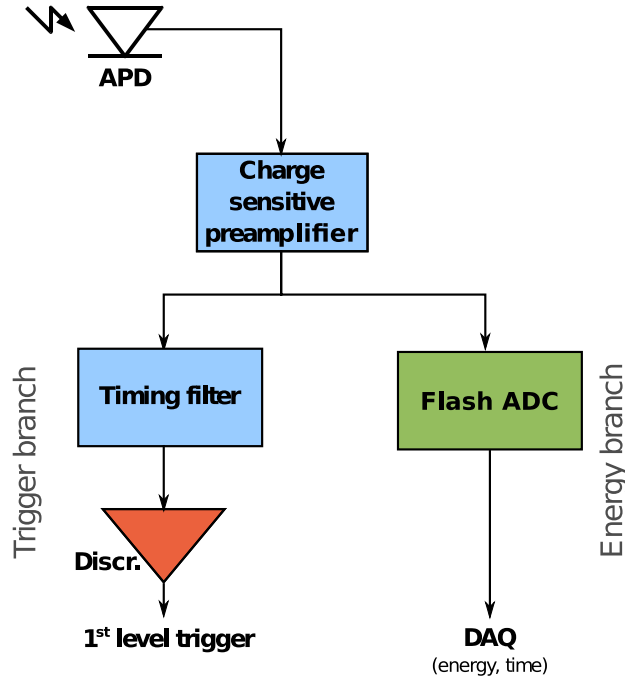


Figure 7.1: Dual signal path for triggering and high resolution energy readout as proposed in this work.

The option to use the preamplifier signal as an energy optimized signal directly was tested in this work. For this readout strategy, the preamplifier signal was directly read by a FADC. A method was devised that yields a high energy resolution and at the same time makes time extraction possible. It was shown that such a readout is possible by doing peak-sensing on the preamplifier signal. With LED pulser tests the energy resolution of the electronics (comprising APD) was measured and was proven to be better than 0.5% for energies higher than 120 MeV and better than 3% for energies higher than 20 MeV respectively. Although not directly comparable, both values are superior to the current benchmark values of the complete Crystal Barrel readout. That leads to the conclusion that the resolution will either stay the same or improve upon the upgrade to an APD based readout.

Time extraction was realized digitally via a linear regression to the leading edge of the preamplifier signal. The straightforward algorithm can be run on an FPGA with very sparse memory requirements. A measurement with cosmic muons depositing a mean energy of  $\approx 30$  MeV showed that the time resolution of

the algorithm is better than 7 ns ( $\sigma$ ).

Although there are still some open questions concerning the precise solution, mainly of technical nature, the APD readout seems to be a realistic approach to put the Crystal Barrel main calorimeter in the first level trigger. With the proposed readout scheme, it is possible to gain a sufficiently fast trigger signal from the CsI crystals without degrading the energy resolution.

One of the next steps is to build and test a fully integrated version of the LNP preamplifier with an on-board timing filter. This integrated version is currently under development at the University of Basel. The next test experiments will focus on measuring the energy resolution with real photons or electrons instead of using an LED pulser. Such measurements will yield more realistic values on the possible energy resolution of the new APD readout. The tests will furthermore focus on the homogeneity of the light collection in the end-cap [24].

Finally I conclude that the proposed APD readout is a very promising solution for both the first level trigger of the main calorimeter and also the combined energy and time readout. If the proposed readout can finally be proven trustworthy during the remaining energy resolution tests, no further obstacles have to be overcome. The APD readout then represents a solid readout option for the main calorimeter.

## *7 Summary and conclusion*

# A Operation preliminaries for the LNP preamplifier

The following steps describe how to assure proper operation of the LNP preamplifier with existing readout electronics.

## A.1 Reversing the polarity of the output

Although the LNP preamplifier is designed for positive signal output it is possible to operate it with negative polarity. This can be useful to do tests with existing discriminators that require negative input polarity.

The output of the LNP preamplifier can simply be reversed by swapping the anode and cathode wires to the APD, whilst at the same time changing the polarity of the HV from positive to negative. For that reason negative high voltage (HV) modules are used (see Section 4.5) instead of positive HV as originally suggested [36]. By doing this the dynamic range of the LNP preamplifier, which asymmetrically favors positive signals, is effectively reduced by a factor of 3 to 4. To slightly compensate for this effect it is possible to change the low voltage (LV) supply from the asymmetric  $+8\text{ V} / -2\text{ V}$  to  $+5\text{ V} / -5\text{ V}$  [45]. However, this alteration to low voltage still results in a reduced dynamic range by a factor of approximately 2. It furthermore makes the whole circuit more susceptible to oscillations. Although the overall performance of the LNP preamplifier is reduced by the alterations, operation is still possible and linearity is preserved.

## A.2 Modifications towards noise reduction

To reduce noise and avoid the injection of unwanted signals the following guidelines were followed [45, 50]. Upon enforcement of those guidelines SNR systematically improved by more than one order of magnitude during the test experiments.

Although the LNP preamplifier was initially housed in a aluminum case attached to the end-cap, the shielding was not connected to ground. This configuration resulted in two separated Faraday cages. One consisting of the cable shielding and one housed the preamplifier. This configuration allowed electromagnetic signals to leak into the case of the preamplifier. Where shielding of the cable entered the preamplifier housing, it acted as an antenna that couples the outside field into the box. As a consequence the whole circuit started to act as a very sensitive amplifier for environmental noise.

## A Operation preliminaries for the LNP preamplifier

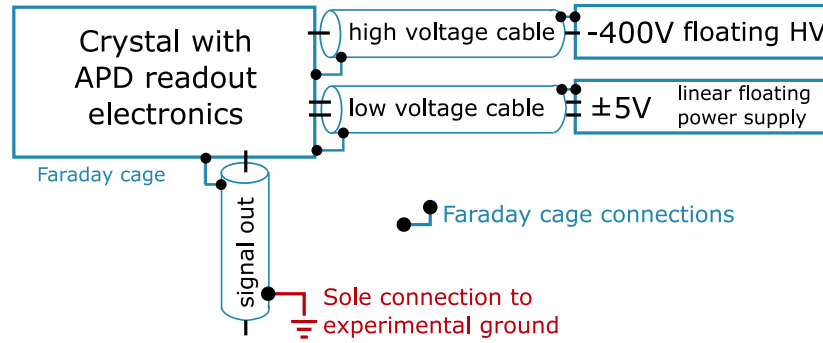


Figure A.1: The whole crystal, including the APD readout is enclosed in a Faraday cage. All cables running in or out the end-cap are also shielded, thus being a part of this cage. The enclosure ensures the minimization of noise pick-up from environment.

To solve that problem a single silver wire is used to connect the ground plane of the preamplifier circuit board with the aluminum housing of each end-cap. It is important that this ground is kept floating and the connection is only made in a single point to avoid ground loops.

The shield of the high voltage cable is soldered to the experimental ground of the preamplifier board while the other end is left floating. This avoids ground loops. Following the same idea the low voltage cables were shielded and the shield is connected to the preamplifier ground plane. Again the other side is kept floating. In this configuration both low voltage and high voltage supply have to be floating. As a high voltage supply a EDS F 025n104-K is used. Details on that module are given in Section 4.5.

Low voltage is provided by a linear laboratory power supply. It is distributed on a printed circuit board, that is encased in a metal box for shielding. The case is connected to the ground plane of the power distributor in a single spot.

So far all equipment allows operation with a floating ground. Depending on the type of measurement this ground should be fixed to a designated potential with a single connection. In cases when the outer circumstances require surveillance measurements with an oscilloscope while there already is a non-avoidable ground connection at a different point, the ground contact of the oscilloscope power cable should be disconnected to avoid the effects of the associated ground loop.

Figure A.1 illustrates how one single ground connection is spread throughout the experiment without creating loops. At the same time it provides a fully closed Faraday cage to hinder environmental noise to get to the very sensitive input of the LNP preamplifier.

## B Quantization errors in $t_0$ extraction

The  $t_0$  time extraction is achieved with a linear fit  $y(t)$  to the leading edge of the preamplifier signal.  $t_0$  is extracted by finding the intercept of the baseline  $\beta$  with the linear function  $y(t)$ , which is defined as  $y(x) = at + b$ . The input signal is sampled in time discrete intervals  $\Delta t$ . The values are labelled  $y_i = y(i\Delta t + t_0)$ . The baseline  $\beta$  is extracted as the arithmetic mean of  $n$  samples prior to the fit. The calculation of the actual fit is based on the following sums

$$\begin{aligned}\chi &= \sum_i^N t_i \\ s_y &= \sum_i^N y_i \\ \xi &= \sum_i^N t_i^2 \\ s_{ty} &= \sum_i^N t_i y_i\end{aligned}$$

where  $N$  is the number of samples included in the fit. For all applications it is possible to start counting the clock cycles with  $t_1 = 1$ . In direct consequence the two sums  $\chi$  and  $\xi$  are only depending on  $N$ . In that case only  $s_y$  and  $s_{ty}$  need to be calculated. By further defining

$$d = N\xi - \chi^2 \tag{B.1}$$

the parameters  $a$  and  $b$  are simply given as

$$\begin{aligned}a &= \frac{Ns_{ty} - \chi s_y}{d} \\ b &= \frac{\xi s_y - \chi s_{ty}}{d}\end{aligned}$$

Finally the  $t_0$  time is given by

$$t_0 = \frac{\beta - b}{a}$$

To derive the time resolution  $\sigma_{t_0}$ , it is convenient to set  $t_0 = 0$  and  $\beta = 0$ . For this derivation only the uncertainty  $\sigma_{y_i}$  will be taken into account. Furthermore

## B Quantization errors in $t_0$ extraction

$\Delta t = 1$  is assumed during the derivation. Therefore  $\sigma_{t_0}$  is fully determined by  $\sigma_a$ ,  $\sigma_b$  and  $\sigma_\beta$  as

$$\sigma_{t_0} = \sqrt{\left(\frac{b}{a^2}\sigma_a\right)^2 + \left(\frac{1}{a}\sigma_b\right)^2 + \left(\frac{1}{a}\sigma_\beta\right)^2} \quad (\text{B.2})$$

It is important to note that the uncertainty in  $y$  direction is constant  $\sigma_{y_i} = \sigma_y = p/\sqrt{12}$  which is a direct consequence of the equidistant channel pitch  $p$  of the ADC. The uncertainties of  $a$  and  $b$  given by Gaussian propagation of error are

$$\sigma_a = \frac{1}{a} \sqrt{N^2\xi - N\chi^2} \sigma_y = \sqrt{\frac{N}{a}} \sigma_y \equiv K_N \sigma_y \quad (\text{B.3})$$

$$\sigma_b = \frac{1}{a} \sqrt{N\xi^2 - \xi\chi^2} \sigma_y = \sqrt{\frac{\xi}{a}} \sigma_y \equiv \Lambda_N \sigma_y \quad (\text{B.4})$$

Since the baseline  $\beta$  is calculated as the arithmetic mean of  $n$  samples, its uncertainty is given as

$$\sigma_\beta = \frac{\sigma_y}{\sqrt{n}}$$

$K_N$  and  $\Lambda_N$  are well defined by a given value of  $N$ . Likewise the ratio  $\sigma_a/\sigma_b$  is only dependent on  $N$ . In the case of  $N \geq 20$  it follows that  $\sigma_a \leq 0.1\sigma_b$ . In general the external trigger assures that sampling starts close to the exact starting time of the rising edge of the signal which is equivalent to  $b \leq 1$ . If furthermore  $n \gg 1$  is assured,  $\sigma_\beta$  can be neglected. Therefore Equation B.2 can be approximated with

$$\sigma_{t_0} \approx \frac{\sigma_b}{a} \quad (\text{B.5})$$

where  $\sigma_b$  is fully defined by the number of samples in the fit ( $N$ ) and the effective ADC resolution ( $\sigma_y$ ). However,  $t_0$  has a strong dependence on the slope parameter  $a$  and therefore on the size of the signal.

To take into account the effect of the finite resolution, the dynamic range of the ADC becomes a crucial parameter. Suppose you want to assure that a maximum energy  $E_{\max}$  is still measurable. That means that the maximum channel of the ADC  $y_{\max}$  corresponds to  $E_{\max}$ . However, for the time extraction only the first  $N$  samples are taken into account. Therefore the maximum of the curve is not relevant at all. The active dynamic range available for the linear fit is therefore reduced by the factor  $\alpha$  that is given by

$$\alpha = \frac{y_N}{y_{\max}}$$

The parameter  $\alpha$  depends on  $N$  and has to be determined from the pulse shape (see Figure B.1).

It is now possible to estimate the time resolution of the fitting method for a specific ADC resolution  $r$  ( $[r]=\text{bit}$ ), a given energy range  $E_{\max}$  and a certain sampling interval  $\Delta t$ . The channel pitch  $p$  can now be expressed as  $p = E_{\max}/2^r$ . For a given  $N$  for which a linear fit is well justified, the simple relation  $a = E\alpha/N$  holds. Combining this with Equation B.5 and furthermore taking into account

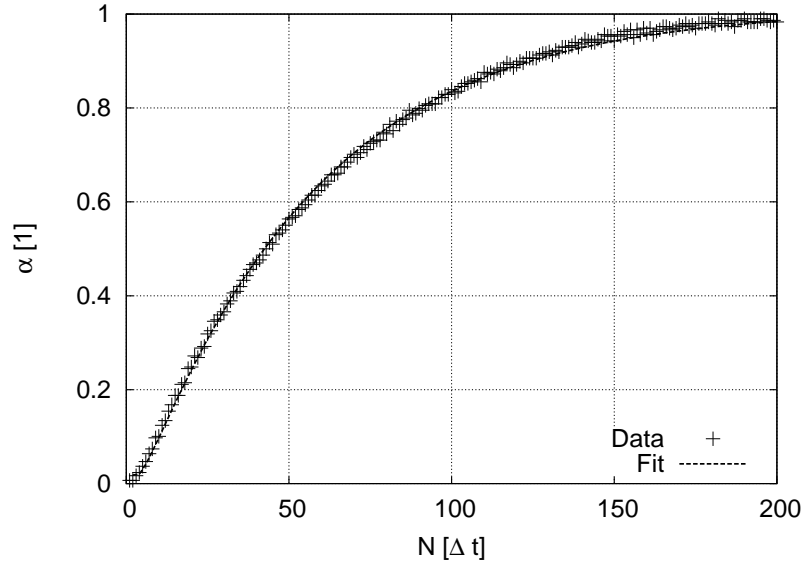


Figure B.1: Characteristic shape of the rising edge of the preamplifier signal in combination with a CsI(Tl) crystal. It is possible to fit the empirical function  $f(x) = 1 - \exp(p_1 x + p_2) + p_3/\sqrt{x}$  to the data. The parameters are given by  $p_1 = -0.01843$ ,  $p_2 = 0.146$  and  $p_3 = 0.19$ .

that  $\sigma_b = \Lambda_N \sigma_y \Delta t = \Lambda_N \Delta t \frac{E_{\max}}{2^r} \frac{1}{\sqrt{12}}$  (see Equation B.4), where also  $\Delta t$  was introduced as a free parameter again, one obtains

$$\sigma_{t_0}(E) = \frac{1}{\sqrt{12}} \frac{N \Lambda_N}{\alpha 2^r} \frac{E_{\max}}{E} \Delta t$$

In scenarios where the quantization error is negligible in comparison to the noise level the above derivation remains valid if  $\sigma_y$  is replaced with the RMS amplitude of the noise. For the precise calculation  $\sigma_y$  should be chosen as the geometric mean of quantization error and RMS noise.

*B Quantization errors in  $t_0$  extraction*

# C Circuit layout diagrams

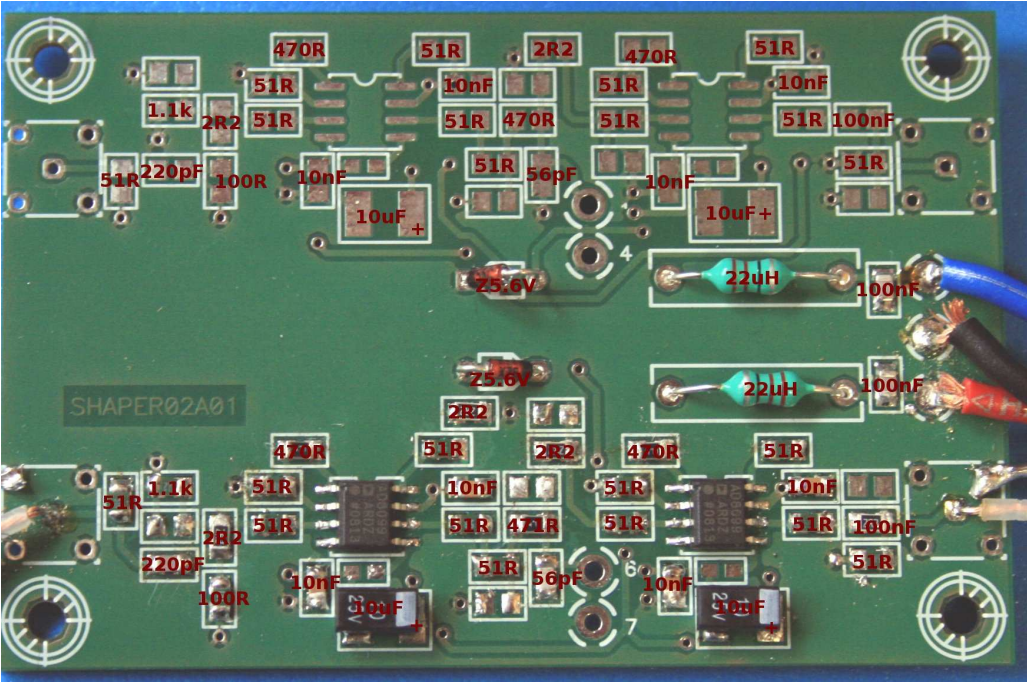


Figure C.1: Overview of PCB component placement for the Shaper rev. 4.2, front. Only the components for one channel have been placed.

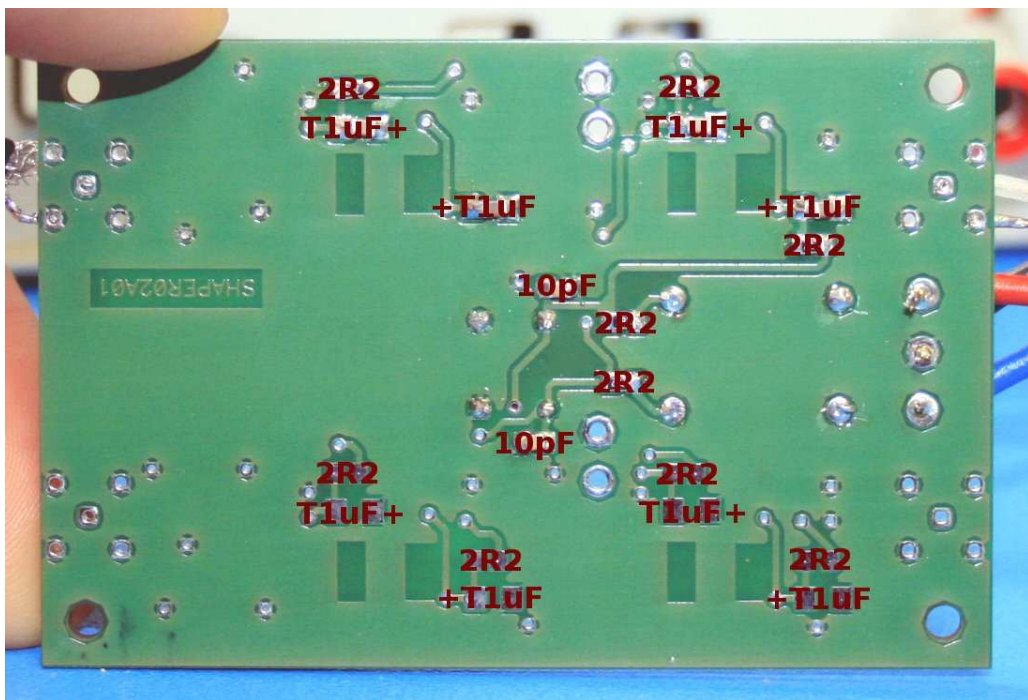


Figure C.2: Overview of PCB component placement for the Shaper rev. 4.2, rear side.



*C Circuit layout diagrams*

# Bibliography

- [1] Aker, E. *et al.*: *The Crystal Barrel spectrometer at LEAR*. Nuclear Instruments and Methods in Physics Research A, 321:69–108, 1992.
- [2] Analog Devices, Inc.: *Dual 350 MHz Low Power Amplifier AD8012*, b ed., 2003.
- [3] Beck, R. Personal communication, Aug. 2008.
- [4] Beck, R. und U. Thoma: *A.1. Spectroscopy of Baryon resonances*. In: *Finanzierungsantrag 01.07.2004 - 30.06.2008*, S. 79–161. Sonderforschungsbereich/Transregio 6034 - Subnuclear Structure of Matter, Elektromagnetische Anregung subnuklearer Systeme, 2004.
- [5] Bethke, S.: *Determination of the QCD coupling  $\alpha_s$* . J. Phys., G26:R27, 2000.
- [6] Blucher, E. *et al.*: *Tests of cesium iodide crystals for an electromagnetic calorimeter*. Nuclear Instruments and Methods in Physics Research A, 249:201–227, 1986.
- [7] Bradtke, C., H. Dutz, H. Peschel, *et al.*: *A new frozen-spin target for  $4\pi$  particle detection*. Nuclear Instruments and Methods in Physics Research A, 436:430–442, 1999.
- [8] Chiang, W.T. and F. Tabakin: *Completeness rules for spin observables in pseudoscalar meson photoproduction*. Phys. Rev. C, 55(4):2054–2066, Apr 1997.
- [9] Dielmann, J.: *Entwicklung, Aufbau und Test eines Detektors zur Bestimmung des Photonenflusses an der Bonner Photonenmarkierungsanlage*. Diploma thesis, Rheinische Friedrich-Wilhelms-Universität Bonn, 2008.
- [10] Eberhardt, M. *et al.*: *The 50 keV Source of Polarized Electrons at ELSA: Past and Future*. AIP Conf. Proc., 915:1031–1036, 2007.
- [11] Elsner, D. *et al.*: *Linearly polarised photon beams at ELSA and measurement of the beam asymmetry in  $\pi^0$ -photoproduction off the proton*. EPJA, 39(3):373–381, Mar. 2009.
- [12] Flemming, H.: *Entwurf und Aufbau eines Zellularlogik-Triggers für das Crystal-Barrel-Experiment an der Elektronenbeschleunigeranlage ELSA*. Dissertation, Ruhr-Universität Bochum, 2001.

## Bibliography

- [13] Funke, C. Personal communication, 2008.
- [14] Funke, C.: *Analyse der Triggerfähigkeiten zur Selektion hadronischer Ereignisse und Entwicklung eines Hochgeschwindigkeits-Triggers für den Vorwärtskonus des Crystal-Barrel-Detektors*. Dissertation, Rheinische Friedrich-Wilhelms-Universität Bonn, 2008.
- [15] Gottschall, M.: *Verbesserung der Triggereigenschaften des Crystal-Barrel-Detektors an ELSA mit einer Silizium-Photomultiplier-Auslese der Kristalle*. Diploma thesis, Rheinische Friedrich-Wilhelms-Universität Bonn, 2007.
- [16] Gruener, M.: *Modifikation und Test des Innendetektors für das Crystal Barrel Experiment*. Diploma thesis, Rheinische Friedrich-Wilhelms-Universität Bonn, 2006.
- [17] Guliyev, E. and H. Löhner: *Apd time resolution with sampling ADC*. In *Annual Report*. KVI, 2007.
- [18] Hamamatsu Photonics K.K. Solid State Division: *Si APD S8664 series*.
- [19] Hamamatsu Photonics K.K. Solid State Division: *Characteristics and use of Si APD (Avalanche Photodiode)*, May 2004.
- [20] Hartmann, J. Personal communication, 2008.
- [21] Hartmann, J.: *Zeitkalibrierung und Photonenflussbestimmung für das Crystal-Barrel Experiment an ELSA*. Diploma thesis, Rheinische Friedrich-Wilhelms-Universität Bonn, 2009.
- [22] Hillert, W.: *Erzeugung eines Nutzstrahls spinpolarisierter Elektronen an der Beschleunigeranlage ELSA*. Postdoctoral lecture qualification thesis, Rheinische Friedrich-Wilhelms-Universität Bonn, 2000.
- [23] Hillert, W.: *The Bonn Electron Stretcher Accelerator ELSA: Past and future*. *European Physical Journal A*, 28:139–148, 2006.
- [24] Honisch, C.: *First level trigger for the Crystal Barrel experiment*. Diploma thesis, Rheinische Friedrich-Wilhelms-Universität Bonn. in preparation.
- [25] Honisch, C. Personal communication, Oct 2008.
- [26] Iseg Spezialelektronik GmbH: *16-channel High Voltage Power Supply EDS F 025n 104-K*, May 2008. <http://www.ortec-online.com/pdf/amptut.pdf>.
- [27] Kaiser, D.: *Aufbau und Test des Gas-Cerenkov-Detektors für den Crystal-Barrel-Aufbau an ELSA*. Diploma thesis, Rheinische Friedrich-Wilhelms-Universität Bonn, 2007.
- [28] Kammer, S.: *Strahlpolarimetrie am CBELSA/TAPS Experiment*. Dissertation, Rheinische Friedrich-Wilhelms-Universität Bonn. in preparation.

- [29] Leo, W.: *Techniques for Nuclear and Particle Physics Experiments: A How-to approach*. Springer-Verlag, New York, Berlin, Heidelberg, 1994.
- [30] Lichtenberg, D.B., W. Namgung, E. Predazzi, and J.G. Wills: *Baryon masses in a relativistic quark-diquark model*. Phys. Rev. Lett., 48(24):1653–1656, Jun 1982.
- [31] Löring, U., B. Metsch, and H. Petry: *The light-baryon spectrum in a relativistic quark model with instanton-induced quark forces*. EPJA, 10(4):395–446, June 2001, ISSN 1434-6001 (PRINT) 1434-601X (ONLINE).
- [32] Makonyi, K.: *Setup of the MINITAPS Detector for the CBELSA/TAPS Experiment*. PhD thesis, Justus-Liebig-University of Gießen. in preparation.
- [33] McGehee, W.R.: *The Gamma Intensity Monitor at CBELSA/TAPS*. B.s. thesis, Massachusetts Institute of Technology, 2008.
- [34] Mesytec GmbH & Co. KG: *MSCF-16 - 16 fold Spectroscopy Amplifier with CFDs and Multiplicity Trigger*, Apr. 2008.
- [35] Novotny, R.: *The BaF<sub>2</sub> photon spectrometer TAPS*. IEEE Trans. Nucl. Sci., NS-38:379–385, 1991.
- [36] Novotny, R. Personal communication, 2008.
- [37] Novotny, R. *et al.*: *Performance of PWO-II Prototype Arrays for the EMC of PANDA*. IEEE Trans. Nucl. Sci., 55(3):1295–1298, June 2008.
- [38] Olsen, H. and L. Maximon: *Photon and Electron Polarization in High-Energy Bremsstrahlung and Pair Production with Screening*. Phys. Rev., 114(3):887–904, May 1959.
- [39] Ortec: *Introduction to ORTEC Amplifiers*, Aug. 2007. <http://www.ortec-online.com/pdf/amptut.pdf>.
- [40] PANDA Collaboration: *Technical Design Report for PANDA Electromagnetic Calorimeter (EMC)*. arXiv.org, 0810.1216v1, 2008.
- [41] Schmieden, H. Personal communication, 2008.
- [42] Schmitz, R. Personal communication, Nov 2008.
- [43] Schumann, S.: *Test der Sampling-ADCs für den Crystal Ball-Detektor*. Diploma thesis, Johannes Gutenberg-Universität Mainz, Sept 2004.
- [44] Shannon, C.: *Communication in the presence of noise*. Proceedings of the IEEE, 86(2):447 – 457, Feb 1998.
- [45] Steinacher, M. Personal communication, 2008.

## Bibliography

- [46] Suft, G. *et al.*: *A scintillating fibre detector for the Crystal Barrel experiment at ELSA*. Nuclear Instruments and Methods in Physics Research Section A, 531:416–424, 2005.
- [47] Thiel, A. Personal communication, Mar. 2009.
- [48] Thoma, U. Personal communication, Sept. 2008.
- [49] Tietze, U. and C. Schenk: *Halbleiter-Schaltungstechnik*. Springer-Verlag, 10th ed., 1993.
- [50] Walther, D. Personal communication, 2008.
- [51] Wehrfritz, M.: *Entwicklung und Test eines Silizium-Photomultiplier-Triggers für das Crystal-Barrel-Kalorimeter*. Diploma thesis, Rheinische Friedrich-Wilhelms-Universität Bonn, 2008.
- [52] Wendel, C.: *Design und Aufbau eines Szintillationsdetektors zur Identifizierung geladener Teilchen im Crystal-Barrel-Vorwärtsdetektor*. Dissertation, Rheinische Friedrich-Wilhelms-Universität Bonn, 2008.
- [53] Winnebeck, A.: *Entwicklung und Implementierung eines universellen, FPGA basierten Triggermoduls für das Crystal-Barrel-Experiment an ELSA*. Diploma thesis, Rheinische Friedrich-Wilhelms-Universität Bonn, 2006.
- [54] Yao, W.M. *et al.*: *The Review of Particle Physics*. Journal of Physics G: Nuclear and Particle Physics, 33, 2006.